

Marcel Pfeifer

# Novel Approaches to Optical Activity Measurements



Cuvillier Verlag Göttingen  
Internationaler wissenschaftlicher Fachverlag



## Novel Approaches to Optical Activity Measurements





# Novel Approaches to Optical Activity Measurements

Von der Fakultät Chemie der Universität Stuttgart  
zur Erlangung der Würde eines Doktors der  
Naturwissenschaften (Dr. rer. nat.) genehmigte Abhandlung

Vorgelegt von  
Dipl. Phys. Marcel Pfeifer  
aus Sigmaringen

Hauptberichter: Prof. Peer Fischer  
Mitberichter: Prof. Joris van Slageren  
Prüfungsvorsitzende: Prof. Sabine Ludwigs

Tag der mündlichen Prüfung: 04.02.2014

Institut für Physikalische Chemie der Universität Stuttgart  
November 2013

D 93



Bibliografische Information der Deutschen Nationalbibliothek  
Die Deutsche Nationalbibliothek verzeichnet diese Publikation in der  
Deutschen Nationalbibliografie; detaillierte bibliografische Daten  
sind im Internet über <http://dnb.d-nb.de> abrufbar.

1. Aufl. - Göttingen: Cuvillier, 2014

Zugl.: Stuttgart, Univ., Diss., 2013

978-3-95404-671-3

© CUVILLIER VERLAG, Göttingen 2014

Nonnenstieg 8, 37075 Göttingen

Telefon: 0551-54724-0

Telefax: 0551-54724-21

[www.cuvillier.de](http://www.cuvillier.de)

Alle Rechte vorbehalten. Ohne ausdrückliche Genehmigung  
des Verlages ist es nicht gestattet, das Buch oder Teile  
daraus auf fotomechanischem Weg (Fotokopie, Mikrokopie)  
zu vervielfältigen.

1. Auflage, 2014

Gedruckt auf umweltfreundlichem, säurefreiem Papier  
aus nachhaltiger Forstwirtschaft.

978-3-95404-671-3



## Erklärung der Selbstständigkeit

Hiermit versichere ich, dass ich die vorliegende Arbeit selbstständig verfasst und keine anderen als die angegebenen Quellen und Hilfsmittel benutzt habe. Aus fremden Quellen entnommene Passagen sind als solche kenntlich gemacht.

## Declaration of Authorship

I hereby certify that this dissertation is entirely my own work except where otherwise indicated. Passages and ideas from other sources have been clearly indicated.

Freiburg, den 12.11.2013

Marcel Pfeifer





# Contents

	Page
List of symbols and abbreviations	i
Zusammenfassung	iii
Abstract	v
<b>1 Introduction</b>	<b>1</b>
1.1 Life is chiral . . . . .	1
1.2 Probing chirality . . . . .	2
1.3 Motivation and outline . . . . .	4
1.4 Publication of main results . . . . .	5
<b>2 Theory</b>	<b>7</b>
2.1 Definitions of molecular chirality and optical activity . . . . .	7
2.1.1 Definitions and sources for molecular chirality . . . . .	7
2.1.2 Definition of optical activity and symmetry considerations . . . . .	10
2.2 Polarized light as a probe for chirality . . . . .	11
2.2.1 States of polarized light . . . . .	12
2.2.2 Light-matter-interaction . . . . .	17
2.2.3 Observables of optical activity . . . . .	19
<b>3 Chiral Refractometry</b>	<b>29</b>
3.1 Optical activity induced light beam deflection and splitting . . . . .	30
3.1.1 Calculation of light beam splitting . . . . .	30
3.1.2 Magneto optical activity: The Faraday Effect . . . . .	32
3.2 Position method: dual polarization modulation . . . . .	33
3.2.1 Experimental setup . . . . .	33
3.2.2 Model and calculations . . . . .	34
3.2.3 Measurements . . . . .	37
3.3 Intensity method: weak value amplified detection . . . . .	38
3.3.1 Weak value amplified measurement of small beam deflections . . . . .	39
3.3.2 Heterodyne weak value amplified measurements . . . . .	42
3.3.3 Polarization modulated weak value amplified measurements . . . . .	47
3.4 Comparison of methods . . . . .	51



4	MIR Laser-Based Vibrational Optical Activity	55
4.1	Theory	56
4.1.1	Measurement of vibrational circular dichroism, VCD	57
4.1.2	Measurement of vibrational circular birefringence, VCB	58
4.2	Optical setup	59
4.2.1	Quantum cascade laser-based setup for VCD measurements	59
4.2.2	Quantum cascade laser-based setup for VCB measurements	60
4.2.3	Reference spectra and theoretical calculations	61
4.3	QCL based measurements of vibrational optical activity	61
4.3.1	Noise and stability	62
4.3.2	VOA measurements I: Ni-sparteine complex	62
4.3.3	VOA measurements II: Limonene	63
4.3.4	VOA measurements III: Proline	65
4.3.5	Modified optical setup	67
4.3.6	VOA measurements IV: Test of the modified setup	69
5	Mid-Infrared Refractometry	73
5.1	Experimental setup	74
5.2	Theoretical model	75
5.3	Measurements	78
6	Chiral Scattering and Colloidal Molecules	83
6.1	Synthesis of chiral colloids	84
6.2	Optical characterization	85
6.2.1	Calculation of circular differential scattering (CDSI)	85
6.2.2	Experimental setup	95
6.2.3	Measurements	96
6.3	The propeller-effect and chiral separation	101
7	Conclusion	103
7.1	Chiral refractometry	103
7.2	MIR laser-based vibrational optical activity	104
7.3	Mid-infrared refractometry	106
7.4	Chiral scattering and colloidal molecules	106
	References	109
	Own Publications	119
	Danksagung	121



# List of symbols and abbreviations

## Symbols

$\mathbf{E}, \mathbf{B}$	vector of the electric and magnetic field
$I$	intensity of the electromagnetic field
$\nabla$	differential operator Nabla
$\mathbf{k}$	wave vector of radiation
$\epsilon_0, \mu_0$	vacuum permittivity, vacuum permeability
$\epsilon$	dielectric permittivity
$\tilde{n} = n + i\kappa$	complex refractive index
$n$	refractive index (real part of $\tilde{n}$ )
$\kappa$	absorption index (imaginary part of $\tilde{n}$ )
$c_0, c$	speed of light in vacuum and medium with refractive index $n$
$\lambda_0, \lambda$	wavelength of radiation in vacuum and medium with refractive index $n$
$\omega$	angular frequency
$\hbar$	reduced Planck constant
$\hat{H}$	Hamilton operator
$\hat{\mu}$	electric dipole operator
$\hat{m}$	magnetic dipole operator
$\hat{\Theta}$	electric quadrupole operator
$\underline{\alpha}$	electric dipole polarizability tensor
$\underline{G}'$	mixed electric-magnetic dipole polarizability tensor (optical activity tensor)
$\underline{A}$	mixed electric dipole-electric quadrupole polarizability tensor
$D_{jn}$	dipole strength of transition $ \mathbf{n}\rangle \leftrightarrow  \mathbf{j}\rangle$
$R_{jn}$	rotational strength of transition $ \mathbf{n}\rangle \leftrightarrow  \mathbf{j}\rangle$
$\alpha, [\alpha]$	optical rotation angle and specific rotation
$\psi, [\psi]$	ellipticity and specific ellipticity
$J_0, J_1, J_2$	Bessel functions of zeroth, first and second order
$j_1, j_2$	spherical Bessel functions of first and second order



---

$\operatorname{erf}(x)$	error function
$A'', \epsilon''$	absorbance and molecular absorptivity
$\hat{\mathbf{e}}_x, \hat{\mathbf{e}}_y, \hat{\mathbf{e}}_z$	unit vectors along the x,y,z-axes
$\delta_{\alpha\beta}$	Kronecker delta
$\epsilon_{\alpha\beta\gamma}$	Levi-Civita symbol

## Abbreviations

CD, CB	Circular Dichroism, Circular Birefringence
VCD, VCB	Vibrational CD, Vibrational CB
VOA	Vibrational Optical Activity
ORD	Optical Rotatory Dispersion
CDSI	Circular Differential Scattering Intensity
MIR	Middle Infrared
QCL	Quantum Cascade Laser
MCT	Mercury Cadmium Telluride
FTIR	Fourier transform infrared (spectroscopy)
FT-VCD	Fourier transform vibrational circular dichroism (spectroscopy)
PEM	Photoelastic Modulator
LIA	Lock-in Amplifier
PMT	Photomultiplier Tube
QWP	Quarter-wave Plate
TIR	Total Internal Reflection
DFT	Density Functional Theory
RMS	Root Mean Square
M	Molar, i.e. a concentration of 1 mol/l
$\mu\text{l}$	microlitre
rad	radian
$\mu\text{m}$ , mm, cm	micrometer, millimeter, centimeter



# Zusammenfassung

Diese Arbeit widmet sich der Entwicklung und Untersuchung neuer optischer Messverfahren zur Analyse chiraler Substanzen. Das Wort *Chiralität* bedeutet wörtlich übersetzt *Händigkeit*, d.h. ein Objekt wird als chiral bezeichnet, wenn es nicht mit seinem Spiegelbild zur Deckung gebracht werden kann, wie zum Beispiel unsere Hände. Ebenso existieren chirale Moleküle in zwei zueinander spiegelbildlichen Konfigurationen ihrer Atome, welche als *Enantiomere* bezeichnet werden. Viele organische, in der Natur vorkommende Moleküle sind chiral, wie z.B. Peptide, Enzyme, viele Aminosäuren oder Proteine. Trotz ähnlicher physikalisch-chemischer Eigenschaften können Enantiomere über sehr unterschiedliche biochemische und physiologische Wirkungen verfügen. Dieser Unterschied ist bei der Entwicklung von neuen pharmazeutischen Wirkstoffen von großer Bedeutung. Während ein Enantiomer die gewünschte Wirkung zeigt, kann das andere nur eingeschränkt wirksam sein oder sogar zu ungewollten Nebeneffekten führen. Ein bekanntes Beispiel ist der Wirkstoff Thalidomid. Er wurde unter dem Namen Contergan in den späten 1950ern als Beruhigungsmittel verkauft, führte jedoch zu schweren Missbildungen von Neugeborenen. Der Contergan-Skandal hat daher gezeigt, dass zur Vermeidung von ungewollten Nebeneffekten zwischen den Enantiomeren pharmazeutischer Wirkstoffe unterschieden werden muss.

Aufgrund der unterschiedlichen Wechselwirkung chiraler Moleküle mit links und rechts zirkular polarisiertem Licht bieten optische Methoden eine direkte Möglichkeit zur Differenzierung der Enantiomere. Makroskopisch führt dieser Unterschied zu einem ungleichen komplexen Brechungsindex  $\tilde{n} = n + i\kappa$  für die beiden Zirkularpolarisationen. Der Unterschied im Realteil des Brechungsindex  $\delta n = n_l - n_r$  ist als *Zirkulare Doppelbrechung (CB)* bekannt, und ist in Brechung, Beugung und Streuung messbar. Der Unterschied im Imaginärteil  $\delta\kappa = \kappa_l - \kappa_r$  hingegen ist gleichbedeutend mit einer differentiellen Absorption und wird *Zirkulardichroismus (CD)* genannt. Die für gewöhnlich kleinen Unterschiede  $\delta n$  und  $\delta\kappa$  ( $\leq 10^{-4}$ ) resultieren in winzigen Effekten, deren Nachweis wiederum experimentell anspruchsvoll ist. Daher werden hier alternative Detektionsmethoden untersucht basierend auf der differentiellen Brechung, Streuung und Absorption zirkular-polarisierten Lichts. Die Arbeit ist hierbei zum Teil motiviert, optische Aktivität in kleinen Probenvolumina und schwierigen (stark absorbierenden) Umgebungen detektierbar zu machen.

Durchtritt linear-polarisiertes Licht eine chirale Substanz, so verursacht der Unterschied im Realteil des Brechungsindex  $\delta n$  die Drehung der Polarisationssebene, bekannt als *optische Rotation*. Da der Drehwinkel direkt proportional zur Konzentration und zurückgelegten

Strecke innerhalb der Substanz ist, werden Langwegzellen für die Messung sehr kleiner Werte von  $\delta n$  benötigt. Dies ist jedoch problematisch, wenn nur kleine Mengen verfügbar sind, was bei der Entwicklung neuer Wirkstoffe oft der Fall ist. Daher werden verschiedene Konzepte für ein *Chirales Refraktometer* vorgestellt, welches die Messung von zirkularer Doppelbrechung in Kleinstvolumina erlaubt. Die Refraktometer basieren auf der differentiellen Brechung der zirkular polarisierten Strahlkomponenten an einer Trennfläche zwischen einem chiralen und einem achiralen Medium. Da in der Regel  $\delta n \leq 10^{-6}$  ist, liegen die zu erwartenden Strahlablenkungen im Nanometerbereich. Drei unterschiedliche Verfahren werden präsentiert und getestet, welche Modulationen der Polarisation mit direkten oder interferometrischen Strahlpositionsmessungen vereinen.

*Vibrational Circular Dichroism (VCD)* misst die differentielle Absorption der zirkular Komponenten im Mittelinfrarot (MIR) bezüglich Vibrationszuständen des chiralen Moleküls. Da VCD damit sensitiv gegenüber der räumlichen Anordnung bestimmter funktionaler Gruppen ist, ist es ein wichtiges Werkzeug zur Ermittlung der Absolutkonfiguration chiraler Moleküle. Ein Problem jedoch ist meist die starke Absorption des Lösemittels selbst, was die Untersuchungen auf ausgewählte Substanzen und Spektralbereiche einschränkt. Aus diesem Grund wurde ein Quanten-Kaskaden-Laser (QCL) basiertes VCD-Spektrometer realisiert. QCLs bieten unter anderem eine deutlich höhere Ausgangsleistung im Vergleich zu thermischen Lichtquellen ( $\sim 10^4$ ), was VCD-Messungen in stark absorbierenden Lösungsmitteln wie Wasser ermöglicht. Untersuchungen an Lösungen verschiedener chiraler Substanzen (u.a. Prolin in Wasser) werden gezeigt und sowohl mit quantenchemischen Rechnungen als auch mit Referenzmessungen an einem FT-VCD-Spektrometer verglichen. Ihrem robusten und kompakten Design zum Trotz leiden QCLs oftmals unter Intensitätsschwankungen, welche die erreichbare Sensitivität von Absorptionsmessungen limitiert. Anhand eines indirekten Messverfahrens wird gezeigt, wie Absorptionsspektren ohne direkte Detektion der Intensität bestimmt werden können. Das vorgestellte Verfahren ist eine Art MIR-Refraktometer, welches über die Bestimmung des Totalreflexionswinkels die Messung der Absorption ermöglicht. Hierfür werden Änderungen des Strahlprofils nach der Totalreflexion an einer Grenzfläche zwischen einem ZnSe-Prisma und der untersuchten Flüssigkeit analysiert und sowohl Real- als auch Imaginärteil simultan bestimmt. Ergebnisse für Dichlormethan (DCM) werden präsentiert.

Chirale Kolloide mit einer Größe von wenigen Mikrometern bieten die Möglichkeit, Effekte auf mesoskopischen Längenskalen zu untersuchen, welche auf molekularer Ebene nur schwer nachweisbar sind. Glancing Angle Physical Vapor Deposition (GLAD) wird für Herstellung der Kolloide mit programmierbarer Geometrie, Chiralität und Materialzusammensetzung in großer Stückzahl benutzt. Die differentielle Streuung von zirkular polarisiertem Licht dient dabei der Untersuchung und Charakterisierung der Kolloide in Lösung. Die Messungen werden mit Rechnungen basierend auf einem analytischen Modell verglichen. Es wird gezeigt, dass die differentiellen Streusignale sensitiv gegenüber den chiralen Strukturelementen der Kolloide sind.



# Abstract

This thesis is dedicated to the development and study of new optical measurement techniques for the analysis of chiral substances. The word *chirality*, which has its origin in the Greek, literally means handedness. So an object is called chiral if it can not be superimposed with its mirror image, as for example our left and right hands. Similarly, chiral molecules exist in two geometric configurations of their atoms with mirror-image symmetry. These mirror images are called *enantiomers*. Many natural and organic molecules are chiral, such as peptides, enzymes, many amino acids or proteins. Despite similar physical and chemical properties, enantiomers may have very different biochemical and physiological effects. This difference is of great interest for the development of new pharmaceutically active compounds. While one of the enantiomers posses the desired effect, the other may have limited activity or even cause unwanted side effects. A prominent example is the drug thalidomide, which was sold as a sedative (Contergan) in the late 1950s, but caused severe birth defects. Therefore, the thalidomide case raised awareness for the discrimination of enantiomers of chiral pharmaceuticals to prevent side effects.

Optical methods provide a direct means of distinguishing the enantiomers due to their differential interaction with left and right circularly polarized light. Macroscopically this difference leads to an unequal complex refractive index  $\tilde{n} = n + i\kappa$  for the two circular polarizations, which manifests itself in various ways and is referred to as *Optical Activity*. The difference in the real part of the refractive index,  $\delta n = n_l - n_r$ , is known as *Circular Birefringence (CB)*, and is detectable in refraction, diffraction or scattering. The difference in the imaginary part  $\delta\kappa = \kappa_l - \kappa_r$ , called *Circular Dichroism (CD)*, is equivalent to a differential absorption of left- and right-circularly polarized light. The usually small differences  $\delta n$  and  $\delta\kappa$  ( $\leq 10^4$ ) result in tiny effects, which in turn are experimentally demanding to detect. Therefore, in the presented work alternative detection methods for both  $\delta n$  and  $\delta\kappa$  are developed and examined. They are based on the differential refraction, scattering and absorption of circularly polarized light. Thereby the work is in part motivated by the challenge of detecting optical activity in small sample volumes or in difficult (strong absorbing) environments.

When traversing a chiral liquid the difference in the real part of the refractive index  $\delta n$  causes the rotation of the plane of polarization for linear-polarized light, known as *Optical Rotation*. Since the rotation angle is directly proportional to the concentration and the distance the light traveled within the substance, longer pathlength cells are needed if small

values of  $\delta n$  are to be detected. This is difficult if only small sample volumes are available, which is often the case in the synthesis of new compounds. Therefore, different concepts for a *Chiral Refractometer* are presented, which allow the measurement of circular birefringence in microfluidic volumes. The refractometers are based on the differential refraction of circularly polarized beam components at a surface between a chiral and achiral medium. Since  $\delta n$  is usually  $\leq 10^{-6}$ , the expected lateral separations between the beam components are in the nanometer range. Three different detection schemes are presented and tested, all combining appropriate polarization modulation techniques with direct or interferometric beam position measurements.

Vibrational Circular Dichroism (VCD) in the middle infrared (MIR) probes the differential absorbance between circular polarization states observed across the absorption bands of molecular vibrational modes. Since VCD is sensitive to the mutual orientation of distinct functional groups, it provides structural information and has become an important tool for the determination of the absolute configuration of chiral molecules. One problem, however, is the strong absorption of many solvents, which usually limits the studies to selected solvents and spectral regions. Consequently, a quantum cascade laser (QCL) based VCD spectrometer was realized. QCLs provide a higher output power compared to thermal light sources ( $\sim 10^4$ ), which allows VCD studies in strongly absorbing solvents like water. Solutions of different chiral compounds are examined and compared with FT-VCD reference measurements, as well as theoretical calculations. These include an aqueous solution of the amino acid proline with an optical density of up to 3.5.

Despite their compact and rugged design QCLs are often plagued by intensity fluctuations, which limits the achievable sensitivity in absorption measurements. An indirect method is shown, how vibrational spectra can be determined without the need for direct intensity measurements. The presented setup is a type of mid-infrared refractometer, which allows the measurement of the absorption through the determination of the angle of total internal reflection. Here changes in the beam profile are analyzed after the total internal reflection at a boundary between a ZnSe-Prism and the sample. Both the real and imaginary parts ( $n$  and  $\kappa$ ) are simultaneously revealed. Measurement results of Dichloromethane (DCM) are presented, which exhibits a single absorption band in the examined spectral range.

Chiral colloids with a size of a few micrometers provide the possibility to examine effects on a mesoscopic length scale which are difficult to prove at the molecular level. Glancing Angle Physical Vapor Deposition (GLAD) is used for the parallel grows of such colloids with programmable shape, chirality and material composition in large quantities. The differential scattering of circularly polarized light is used for the characterization of these colloids in solution. The measurements are compared with calculations based on an analytical model. It is shown that the differential scattering signal is sensitive to the chiral structural features of the colloids.



# 1

## Introduction

### 1.1 Life is chiral

The term chirality has its origin in the Greek word *kheir*, which means hand. It was brought into general use by Lord Kelvin, who stated in 1894 [1]:

*“I call any geometrical figure, or any group of points, chiral, and say that it has chirality, if its image in a plane mirror, ideally realized, cannot be brought to coincide with itself.”*

Perhaps the most prominent chiral objects are our left and right hands. A molecule is called chiral when it possesses handedness, i.e. it can be found in two geometrical configurations of its atoms with mirror-image symmetry. These mirror images are called enantiomers when referring to molecules, while the word enantiomorphs is usually still reserved for larger objects like crystals. Many organic and natural molecules are chiral, especially those affecting our daily life like peptides, enzymes, amino acids (except glycine) or proteins. But the reason why these molecules exist primarily just in one configuration is still unclear.

The two enantiomers of a chiral molecule possess similar physical and chemical properties in a non-chiral environment but will act differently in the interaction with other chiral objects. This may lead to very different biochemical and physiological effects. Referring to pharmaceutical active compounds this difference is of great interest. While one of the configurations possesses the desired properties the other one may have limited activity or unwanted side effects. A prominent example is the molecule thalidomide (Fig. 1.1), which was sold as a sedative drug (Contergan) in the late 1950s. It was prescribed to treat morning sickness, but caused severe birth defects in the newborn babies. Studies soon indicated that the (*S*)-(-)-enantiomer could be responsible for the fetal damage due to the interaction with the embryo's prenatal DNA [2]. Since both thalidomide enantiomers racemize quickly

in the human body it is not sufficient to take just the (*R*)-conformer. Although the complete picture turned out to be not that simple, the thalidomide case raised awareness for the discrimination of enantiomers of chiral pharmaceuticals to prevent side effects, and the determination of the enantiomeric excess (or purity) is now a requirement demanded by the FDA (U.S. Food and Drug Administration).

## 1.2 Probing chirality

Optical methods provide a direct means of distinguishing the enantiomers of chiral molecules. Most of these methods are based on the differential interaction of the molecules with circularly polarized light, which is also chiral. It is macroscopically described by a difference in the complex refractive index  $\delta\tilde{n} = \delta n + i \delta\kappa$  to left- and right- circularly polarized light, which is referred to as *Optical Activity*. It was first discovered by Jean-Baptiste Biot, Augustin Fresnel, and Aimé Cotton in the early 19th century [3,4]. The usually small differences ( $< 10^{-6}$ ) result in tiny effects, which in turn are experimentally demanding to observe. Nevertheless, a number of optical methods have been developed.

The difference in the real part of the index, called *Circular Birefringence (CB)*, is detectable in refraction, diffraction or scattering. If linearly polarized light traverses an optically active medium, the Circular Birefringence will cause the rotation of the plane of polarization, known as *optical rotation*. In the polarimetry the rotation is detected for the determination of the handedness and/or the concentration of optically active solutions [3]. The variation in the rotation angle as a function of the wavelength is known as *Optical Rotary Dispersion (ORD)*. Since the rotation angle is also proportional to the pathlength

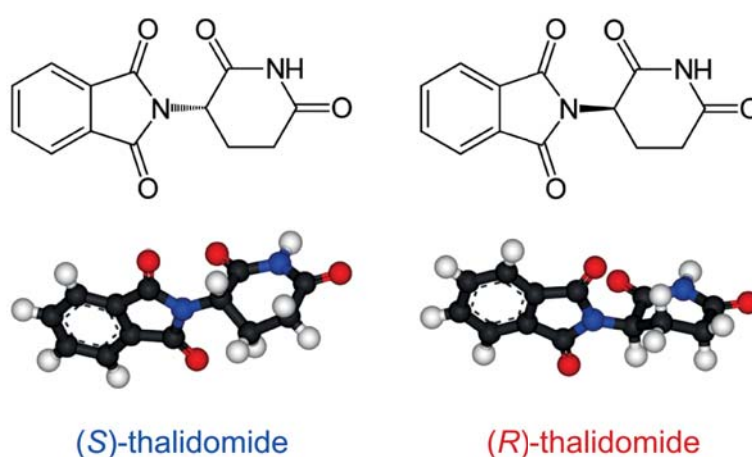


**Figure 1.1:** Both enantiomers of thalidomide, the chiral molecule that caused the Contergan scandal in the late 1950s. Where the (*R*)-enantiomer seems to act as a sedative the other enantiomer turned out to cause dramatic birth defects. (adapted from Wikimedia Commons)

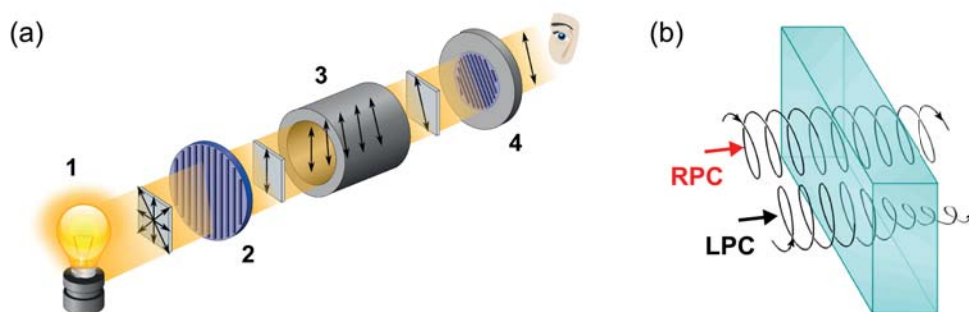


**Figure 1.2:** (a) Schematic of a polarimeter for the detection of optical rotation. Unpolarized light (1) is linearly polarized (2) before passing the optical active sample (3). The rotation is detected with a second rotatable polarizer (4). (b) Circular dichroism (CD) manifests itself in the differential absorption between left- and right-circularly polarized light. (adapted from Wikimedia Commons)

the light travels inside the sample, longer pathlength cells are needed if small differences  $\delta n$  are to be detected. But this is difficult if only small volumes are available, as is often the case in high-throughput screenings or if new compounds are synthesized. Polarimetry in microfluidic volumes is therefore generally not possible. In this thesis a scheme to measure optical activity in sub-micro liter volumes is presented.

*Circular Dichroism (CD)* refers to the difference to left- and right-circularly polarized light,  $\delta\kappa$ , in the imaginary part of the complex refractive index. It is equivalent to a differential absorption of the two circular polarization states, which is measured with a CD spectrometer. Nowadays CD spectroscopy has a wide range of applications depending on the spectral region of interest. UV CD, for example, is used to examine the secondary structure of proteins or charge-transfer processes in chiral metallic complexes [5]. Vibrational Circular Dichroism (VCD) observed across the absorption bands of vibrational molecular transitions extends the CD studies to the middle infrared (MIR) region. Being sensitive to the mutual orientation of distinct functional groups, VCD provides structural information about chiral molecules. Together with *ab initio* calculations VCD has become a powerful tool for the determination of the absolute conformation of small molecules. It is also used for structural studies of small organic molecules, or proteins and DNA [5]. One difficulty, however, is often the strong absorption of the solvent itself, especially in aqueous (polar) solvents. This often restricts traditional VCD instrumentation to selected spectral regions and special solvents. In this thesis it is shown how the use of MIR lasers permit VCD studies in aqueous solutions.

*Raman-Optical-Activity (ROA)* is an alternate form of Vibrational Optical Activity (VOA), measuring the differential Raman scattering intensities of the circular polarizations. It is a complementary technique to VCD spectroscopy. Because ROA spectroscopy uses laser in the transparent (visible) spectral region of the solution, ROA does not suffer from solvent

absorption. It can be observed in a number of forms defined by the polarization of the incident and scattered light [3, 6]. In scattered circular polarization (SCP) experiments, for example, is the incident light linearly polarized and differences in circular polarization components of the scattered light are measured. In dual circular polarization (DCP) ROA the incident as well as the scattered light are circularly polarized. Nevertheless, ROA instrumentations are experimentally and technically more demanding compared to VCD instrumentation and due to the weakness of the observed ROA signals.

In the field of nonlinear optics there are also forms of optical activity [7, 8], and observables exist at different orders of nonlinearity. The intensity of the generated light field in second-order nonlinear processes like sum-frequency (SFG) or second harmonic generation (SHG), for instance, can be used as a measure for the chirality of the sample. Beside these second order process additional optical activity observables are predicted to exist in higher-order processes like the (quartic) nonlinear Raman spectroscopy (BioCARS) with similar properties.

Beside the described methods there are also non-optical indirect tools for chiral structural analysis like nuclear magnetic resonance (NMR) spectroscopy or X-ray diffraction. Because both enantiomers show identical chemical shifts and spin-spin coupling constants, conventional NMR spectroscopy is unable to distinguish between them. This requires the use of chiral reagents typically leading to the formation of diastereomers showing different NMR signals. Ideas for a direct discrimination in chiral NMR have been published [9] as well as the use of achiral reagents [10]. The inelastic or resonant scattering of X-rays by optically active compounds in the solid state is still one of the key methods for the determination of absolute configuration. It has been first proposed and realized by Bijvoet in 1951 [11]. Since elastic X-ray scattering measures the interatomic distances which do not differ for a pair of enantiomers, the absolute configuration can not be determined. Using X-rays with a wavelength near the absorption of just one type of atoms the two crystallized enantiomers can be distinguished. This is due to the additional phase-lag of the radiation resonantly scattered at these atoms. This in turn leads to different scattering patterns for the crystal and its mirror image. Nevertheless, crystallization of optically active compounds with high purity and regularity is not always easy to accomplish, and the evaluation of scattering patterns of complex compounds gets difficult.

Despite the wide diversity of techniques detecting optical activity, this work is in part motivated by the challenge of detecting optical activity in small sample volumes or in difficult (strong absorbing) environments.

### 1.3 Motivation and outline

This work presents and investigates new optical methods for the analysis of chiral media based on different optical activity effects in refraction, absorption and scattering. It is

motivated by the following questions: How can optical activity (OA) be detected in small sample volumes as for example is the case in microfluidics? Can OA be analyzed using VCD in (aqueous) solutions despite the strong solvent absorption? Is there a possibility to observe OA in scattering and are the colloidal analogues chiral molecules?

The first method introduces a *chiral refractometer*. Here the refractive index difference  $\delta n$  (CB) is detected in refraction. At an interface between a chiral and an achiral medium both circular polarization components will refract with slightly different angles of refraction. Light which is initially collinear splits into two polarization components propagating in slightly different directions. This splitting is in the order of nanorad ( $10^{-9}$  rad) for millimolar (mM) solutions. Since the effect happens at the interface the method requires potentially much smaller fluid volumes ( $\sim 1 \mu\text{l}$ ) than usual transmission based experiments (polarimetry). The sensitivity of the measurement scheme now depends on how small a beam displacement or separation can be detected. Therefore different beam position detection schemes are tested and compared with each other.

The second method which has been developed is a VCD spectrometer using quantum cascade lasers (QCL). These middle infrared (MIR) lasers provide orders of magnitude more optical power compared to thermal light sources. This allows optical activity measurements in strongly absorbing solutions. Results for different solutions recorded with the QCL-spectrometer are presented. These include the VCD spectra of aqueous solutions of the amino acid proline with an optical density of up to 3.5 in the examined spectral region. Despite their higher power levels and compact and rugged design QCLs suffer often from intensity fluctuations. This affects and limits the sensitivity in absorption measurements (for example VCD). Therefore a QCL based MIR refractometer is presented, which allows the detection of vibrational spectra without direct measurement of the QCL's intensity. The real and imaginary part ( $n$  and  $\kappa$ ) of the refractive index are determined in an imaging setup. Changes in the beam profile at a total internal reflection interface are used to deduce simultaneously  $n$  and  $\kappa$  of the analyte.

Finally helical colloidal molecules with programmable shape and chirality are investigated. Glancing angle physical vapor deposition (GLAD) is used for the batch-production of large numbers of colloids. Suspensions are characterized in water by differential scattering of both circular polarization components. Scattering CD data of different chiral colloids (helices) are presented and compared to calculation based on a simple analytical model. It is shown that the differential scattering signals are sensitive to the chiral parameters of the colloidal scatterer.

## 1.4 Publication of main results

The main results of this thesis have been published in four peer-reviewed scientific journals and two conference proceedings, on which the following chapters (3,4,5,6) are based on:

### Chapter 3: Chiral refractometer

- M. PFEIFER AND P. FISCHER, “Weak value amplified optical activity measurements”, *Opt. Express* **19**, pp. 16508 - 16517 (2011) [P1].
- M. PFEIFER, AND P. FISCHER, “Heterodyne ”weak measurements” of nanorad beam deflections”, *SENSOR+TEST Conference proc.* **4.3**, (2011), presented at *OPTO 2011* [P2].

### Chapter 4: QCL based vibrational optical activity

- S.LÜDEKE, M. PFEIFER, AND P. FISCHER, “Quantum cascade laser based circular dichroism”, *J. Am. Chem. Soc.* **133**, pp. 5704 - 5707 (2011) [P3].
- M. PFEIFER, S. LÜDEKE, AND P. FISCHER, “Mid-IR laser-based vibrational optical activity”, *Proceedings of SPIE* **8219**, pp. 821906-1 (2012), presented at *Photonics West 2012* [P4].

### Chapter 5: QCL based middle infrared refractometry

- M. PFEIFER, A. RUF, AND P. FISCHER, “Indirect absorption spectroscopy using quantum cascade lasers: mid-infrared refractometry and photothermal spectroscopy”, *Opt. Express* **21**, pp. 25643 - 25654 (2013) [P5].

### Chapter 6: Chiral scattering and colloidal molecules

- D. SCHAMEL, M. PFEIFER, J. G. GIBBS, B. MIKSCH, A. G. MARK, AND P. FISCHER, “Chiral colloidal molecules and observation of the propeller effect”, *J. Am. Chem. Soc.* **135**, pp. 12353 - 12359 (2013) [P6].



# 2

## Theory

This chapter presents the main theoretical background for the understanding of the thesis. A number of different optical effects are covered in the thesis and so we reserve the specific theoretical aspects for subsequent chapters. A short overview of the concepts of molecular chirality and optical activity are given as well as an introduction to the description of polarized light. A detailed analysis of both can be found in the books of Laurence Nafie [12] or Laurence Barron [3]. Here we will point out the main results.

### 2.1 Definitions of molecular chirality and optical activity

#### 2.1.1 Definitions and sources for molecular chirality

We will now take a closer look at the definition of chirality in the context of molecular geometry and symmetry. As mentioned before, a molecule is called chiral if it cannot be superimposed on its mirror image. This is the simplest definition of molecular chirality. A more rigorous definition can be given using group theory, i.e. the classification of symmetry operations. These include rotations, reflections, and improper rotations. A molecule possesses symmetry if it is unchanged after one of those operations. A molecule is chiral, if it does not contain any improper rotation symmetry elements [3], like a center of inversion, reflection planes or rotation-reflection axis. Therefore chiral objects are not asymmetric, since they can possess symmetry. An example is a left- or right-handed helix, a chiral object which is symmetric with respect to a rotation axis through the mid point of the helix, perpendicular to its long axis ( $C_2$ ). Molecular chirality is a special form of isomerism, which describes compounds with the same molecular formula but distinct structural compositions. There

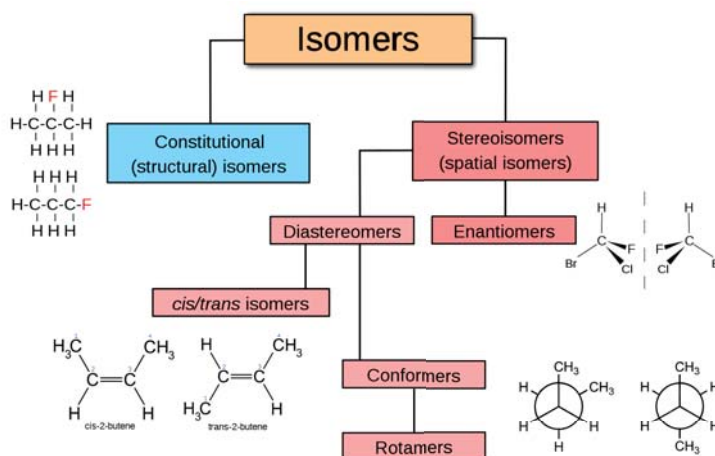


**Figure 2.1:** Overview about the different forms of isomerism. It can be seen, that chirality or enantiomerism is a special form of stereoisomerism (source: Wikimedia Commons)

are many different classes of isomers which can be split into two main forms: structural isomerism and stereoisomerism (spatial isomerism) (Fig. 2.1). Structural or constitutional isomers are compounds where the connections/bonds of atoms and functional groups differ, which is in contrast to stereoisomers. Here the bond structure is the same, but the geometrical orientation of atoms and functional groups in space is different. This class includes the enantiomers of chiral molecules as well as diastereomers. While structural isomers typically have different chemical properties, stereoisomers behave often identically except in their interaction with other stereoisomers, a property already mentioned in chapter 1. Four distinct structural elements can impart chirality in a molecule (Fig. 2.2) [12]:

1. Helix:

It is the simplest embodiment of a chiral structure. Here the molecule possesses a helical shape, where the sense of its chirality is equal to the handedness of the helix and is classified as *P* (plus) for a clockwise and *M* (minus) for a counterclockwise orientation. Examples are the molecule hexahelicene or DNA.

2. Chiral Center:

The chiral center is a central atom bonded to a set of different ligands (atoms or groups of atoms) in a spatial arrangement which is not superposable on its mirror image. In its simplest and most common form a chiral center is an atom with four unequal groups, usually a tetrahedral carbon. But also nitrogen, sulfur or phosphorus can be chiral centers. The chirality of the centers is specified by the letters *R* (rectus) and *S* (sinister) depending on a clockwise or counterclockwise orientation of the ligands with respect to their priority. The priority of the groups is assigned based on their atomic mass following the Cahn-Ingold-Prelog system. In some cases, like

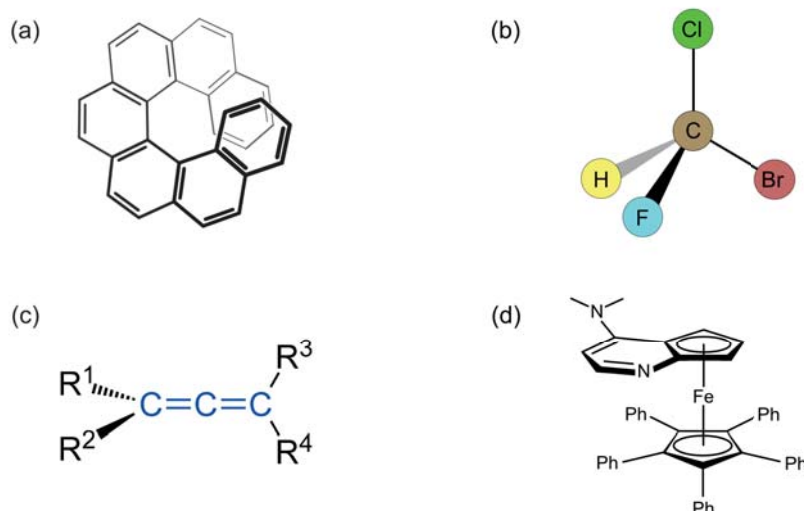


**Figure 2.2:** Schematic illustration of the four structural elements responsible for molecular chirality. These are (a) the helix, (b) the chiral center, (c) the chiral axis, and (d) the chiral plane. See text for details (adapted from Wikimedia Commons).

sugars, amino acids or peptides, a nomenclature with the symbols L and D based on the Fischer projections is used.

### 3. Chiral Axis:

A chiral axis can be thought of as a structure starting from a tetrahedral chiral center where two groups are stretched away from the other two groups. The center now becomes a line of chirality if the two pairs at each end do not lie in the same plane. The four groups no longer need to be different from one another, it is just required that the two groups at each end are not the same. The specification of the axis can follow the *P/M* or *R/S* system based on the relative priority of the groups when looking along the axis, where those nearest to the viewer have a higher priority.

### 4. Chiral Plane:

A chirality plane is the plane of a structural fragment in a chiral molecule that cannot lie in a symmetry plane because of restricted rotation or structural requirements. The enantiomers of such a chiral molecule differ in the spatial arrangement of the remaining atoms of the molecule with respect to the chirality plane. Analogous to the chiral axis the plan is specified by the *P/M* or *R/S* system.

If molecules possess more than one structural chirality element they are termed diastereomers, where each unique combination of the configuration of these elements is a different molecule. Generally each configuration, called diastereomer, has distinct physical and chemical properties. Diastereomers which differ in all of their structural elements are enantiomers of each other and are distinguished only by their mirror symmetry. A racemic

mixture of a chiral substance consist of a equal number of both enantiomers. Any excess of one enantiomer over the other is called the enantiomeric excess  $ee$ , which is defined as the ratio of the absolute difference between the corresponding amounts (moles, concentration, or number of molecules) and their sum:

$$ee = \frac{R - S}{R + S} \times 100 \quad (2.1)$$

Therefore the enantiomeric excess of a racemic mixture is  $ee_{rac} = 0$  whereas for a enantio-pure solution  $ee = \pm 100$ .

### 2.1.2 Definition of optical activity and symmetry considerations

The definition of optical activity involves both, the concepts of molecular chirality and those for circularly polarized radiation. Analogous to enantiomers, left and right circularly polarization states are spatial mirror images if we consider the pattern of their field vectors at any instant in time describing a helix in space. So generally it can be stated, that *natural optical activity* is defined as the differential interaction of a chiral molecule with left- or right-circularly polarized radiation. Electronic optical activity (EOA) and vibrational optical activity (VOA) involve electronic or vibrational transitions, respectively.

The behavior of chiral molecules with respect to spatial and time symmetry operations exhibits information about possible optical activity phenomena and their observables. The parity operator  $\hat{P}$  is the representation of the space inversion symmetry operation, e.g.  $\hat{P}(x, y, z) = (-x, -y, -z)$ . Most physical laws and the corresponding equations representing them are unchanged by  $\hat{P}$ , and the therein described physical processes are said to conserve parity. The time reversal operator  $\hat{T}$  reverses the motion of all particles in the system. Under  $\hat{T}$  the time coordinate  $t$  is replaced by  $-t$  in classical mechanics. In quantum mechanics time reversal is represented by an antiunitary operator  $\hat{T} = \hat{U}\hat{K}$  where  $\hat{U}$  is an unitary operator and  $\hat{K}$  is the operator of complex conjugation [3]. For the case of spinless particles,  $\hat{U}$  is the unit operator so time reversal is accomplished by  $t \rightarrow -t$  and complex conjugation [3, 13]. Otherwise  $\hat{U} = i\sigma_y$ , with  $\sigma_y$  being one of the Pauli spin matrices. If an equation is left unchanged under  $\hat{T}$ , then the system is said to be time reversal invariant or have reversality.

Scalar, vector and tensor physical quantities can be characterized due to their behavior under the operations  $\hat{P}$  and  $\hat{T}$ , i.e. whether they change sign or not, and are correspondingly parity-odd or parity-even, or time-odd or time-even. A vector whose sign changes under  $\hat{P}$  is called a *polar* or *true vector* whereas the sign of a *axial* or *pseudo vector* is unchanged. Examples are the position vector  $\mathbf{r}$  (polar) and the angular momentum vector  $\mathbf{L}$  (axial). Analogue is a *pseudoscalar* a quantity which changes sign with parity operation in contrast to normal scalars. We will see that chiral observables in solutions are pseudoscalars.

The electric field vector  $\mathbf{E}$  and the dipole moment  $\boldsymbol{\mu}$  can also be classified as parity odd, whereas the magnetic field  $\mathbf{B}$  and  $\mathbf{m}$  (dipole moment) are axial vectors [8]. Since the operator  $\hat{T}$  reverses the direction of momenta and spins of charged particles but leaves the charge itself unchanged, it follows that  $\mathbf{E}$  and  $\boldsymbol{\mu}_e$  are time-even and  $\mathbf{B}$  and  $\mathbf{m}$  are time-odd. It now can be verified that the laws of electromagnetism, represented by Maxwell's equations and the Lorentz force equation, conserve parity and reversality [3]. Consequently, any physical process involving just electromagnetism, the interaction of light with a molecule for example, has to do the same.

In an isotropic medium, like an achiral liquid, optical effects cannot depend on the orientation of the sample, since it "looks" the same from all sides. As a consequence all optical observables of this system have to be parity-even scalar quantities, like for example the refractive index. For a chiral object (molecule), however, this symmetry requirement may change. Under parity it is transformed into its mirror image, rendering it parity-odd, since all chirality-specific properties change their sign. Thus this requires scalars and tensors describing the chiral response also to be parity-odd. Furthermore it can be shown, that a true chiral observable, i.e. for natural chirality, has to be symmetric with respect to time reversal [3, 8]. In a chiral solution with  $ee \neq 0$  we therefore expect to find experimental observables that are pseudoscalars.

The weak force, acting on all leptons, is the only fundamental force that does not conserve parity. This leads to a slight difference between the ground state energies of enantiomers on the order of  $\sim 10^{-17}$  of the total energy [12]. This difference disappears, when additionally every particle is replaced by its corresponding anti-particle (charge conjugation operator  $\hat{C}$ ). Thus, an anti-particle mirror image is the true equal-energy enantiomer. This energy difference of the  $\hat{P}\hat{T}$  enantiomers of a molecule induced by the weak force has so far not been observed and is still discussed as one of the possible reasons for the homochirality of most biomolecules.

## 2.2 Polarized light as a probe for chirality

The interaction of polarized light with an optically active medium can act as a test for its chirality. Especially the response to circular polarization states, electromagnetic fields which are chiral by themselves, gives rise to chiroptical effects. This includes effects based on refraction, absorption and scattering, which will be discussed in this thesis. Therefore a convenient formalism describing the polarization states of radiation is needed. In what follows a short summary of two different approaches shall be given. The measurable observables resulting from the interaction of circularly polarized radiation with an optical active medium will subsequently be discussed.

### 2.2.1 States of polarized light

Here the main points of two different matrix based concepts used to describe the polarization of light shall be given. Both are based on the wave nature of light, i.e. the description of electromagnetic radiation as a transverse oscillating wave of electric and magnetic fields obeying Maxwell's equations. While the Jones formalism is based on complex field amplitudes and is therefore able to describe interference effects, the Mueller-Stokes formalism uses the resulting intensities for polarization characterization. With the latter it is also possible to describe partially polarized light in contrast to the Jones formalism. We will restrict our considerations to the case of a plane wave propagating along or under a small angle with respect to an optical axis, i.e. the paraxial case.

#### Jones formalism

Generally, the oscillating electric field of an electromagnetic plane wave at some point  $\mathbf{r} = (x, y, z)^T$  in space and at time  $t$  can be described by:

$$\mathbf{E}(\mathbf{r}, t) = \tilde{\mathbf{A}} \exp \left[ i \left( \tilde{\mathbf{k}} \cdot \mathbf{r} - \omega t \right) \right] \quad (2.2)$$

The complex vector  $\tilde{\mathbf{A}}$  contains the information about the polarization of the wave. The complex wave vector  $\tilde{\mathbf{k}}$  and the angular frequency  $\omega$  are:

$$\tilde{\mathbf{k}} = \frac{2\pi\tilde{n}}{\lambda} \hat{\mathbf{k}} \quad \text{and} \quad \omega = \frac{2\pi c}{\lambda}, \quad (2.3)$$

where  $\lambda$  is the wavelength and  $\tilde{n} = n + i\kappa$  the complex index of refraction. Here  $\hat{\mathbf{k}}$  is a unit vector pointing along the direction of propagation. For a wave traveling along the  $z$ -axis of a Cartesian coordinate system the field vector oscillates in the  $xy$ -plane since the wave is transversal. Any polarization state can now be written as a sum of two orthogonal vectors and Eq. 2.2 simplifies to [12]:

$$\begin{aligned} \mathbf{E}(\mathbf{r}, t) &= (\tilde{A}_x \hat{\mathbf{x}} + \tilde{A}_y \hat{\mathbf{y}}) \exp [i(kz - \omega t)] \\ \text{with } \tilde{A}_{x,y} &= a_{x,y} \exp [i\varphi_{x,y}] \end{aligned} \quad (2.4)$$

The polarization state is fully described by the complex amplitudes  $\tilde{A}_{x,y}$ , therefore it can be characterized by a two-dimensional matrix known as the **Jones vector** [14]:

$$|\mathbf{J}\rangle = \begin{bmatrix} \tilde{A}_x \\ \tilde{A}_y \end{bmatrix} \quad (2.5)$$

polarization	$\varphi_y - \varphi_x$	$a_x, a_y$	Jones vector
linear (LP) in x direction	$n \cdot \pi$	1 , 0	$ \mathbf{H}\rangle = \begin{bmatrix} 1 \\ 0 \end{bmatrix}$
linear (LP) in y direction	$n \cdot \pi$	0 , 1	$ \mathbf{V}\rangle = \begin{bmatrix} 0 \\ 1 \end{bmatrix}$
linear (LP) along angle $\beta$	$n \cdot \pi$	$\cos \beta$ , $\sin \beta$	$ \beta\rangle = \begin{bmatrix} \cos \beta \\ \sin \beta \end{bmatrix}$
left-circular (LCP)	$\frac{\pi}{2}$	1 , 1	$ \mathbf{L}\rangle = \frac{1}{\sqrt{2}} \begin{bmatrix} 1 \\ i \end{bmatrix}$
right-circular (RCP)	$-\frac{\pi}{2}$	1 , 1	$ \mathbf{R}\rangle = \frac{1}{\sqrt{2}} \begin{bmatrix} 1 \\ -i \end{bmatrix}$

**Table 2.1:** Jones vectors for the most common polarization states [14]

The formalism can now be extended to the description of an arbitrarily polarized wave with a spatial profile of the electric field  $\mathcal{E}(x,y)$ , so one can write:

$$\mathbf{E}(\mathbf{r},t) = \mathcal{E}(x,y) \exp[i(kz - \omega t)] |\mathbf{J}\rangle \quad (2.6)$$

This formalism will be used in chapter 3 for the calculation of the intensity profiles in the chiral refractometer measurements using weak value amplification. The resulting polarization state depends on the amplitudes  $a_{x,y}$  and the phases  $\varphi_{x,y}$  of the two polarization vectors. Usually the vector  $|\mathbf{J}\rangle$  is normalized, so  $a_x^2 + a_y^2 = 1$ . The corresponding values for the most common polarization states are shown in Tab. 2.1.

The transmission of a plane wave with arbitrary polarization through an optical system is established through a simple matrix formalism. Each polarization optical element in the system is represented by a  $2 \times 2$  transformation matrix  $\mathbf{T}$ , the so called **Jones matrix**. The Jones vector of the new polarization state follows from matrix multiplication [14]:

$$|\mathbf{J}_2\rangle = \begin{bmatrix} \tilde{A}_{2,x} \\ \tilde{A}_{2,y} \end{bmatrix} = \begin{bmatrix} T_{11} & T_{12} \\ T_{21} & T_{22} \end{bmatrix} \cdot \begin{bmatrix} \tilde{A}_{1,x} \\ \tilde{A}_{1,y} \end{bmatrix} = \mathbf{T} |\mathbf{J}_1\rangle \quad (2.7)$$

For a wave passing  $N$  consecutive optical elements the final polarization state is evaluated through the subsequent multiplication of the corresponding Jones matrices:

$$|\mathbf{J}_2\rangle = \mathbf{T}_N \dots \mathbf{T}_2 \mathbf{T}_1 |\mathbf{J}_1\rangle \quad (2.8)$$

Since the elements of the Jones vectors and matrices depend on the choice of the coordinate system, matrix methods are needed for the transformation between different systems. If  $|\mathbf{J}\rangle$  and  $\mathbf{T}$  are the Jones vector and matrix in the  $xy$ -basis, then the transformation matrix  $\mathbf{R}(\theta)$  can be used to calculate the corresponding quantities  $|\mathbf{J}'\rangle$  and  $\mathbf{T}'$  in the  $x'y'$ -basis rotated by an angle  $\theta$ . The new Jones vector is:

$$|\mathbf{J}'\rangle = \underline{\mathbf{R}}(\theta) |\mathbf{J}\rangle \quad (2.9)$$

Similarly, the Jones Matrices can be transformed [14]:

$$\begin{aligned} \underline{\mathbf{T}}' &= \underline{\mathbf{R}}(\theta) \underline{\mathbf{T}} \underline{\mathbf{R}}(-\theta) \\ \underline{\mathbf{T}} &= \underline{\mathbf{R}}(-\theta) \underline{\mathbf{T}}' \underline{\mathbf{R}}(\theta) \quad \text{with} \quad \underline{\mathbf{R}}(\theta) = \begin{bmatrix} \cos \theta & \sin \theta \\ -\sin \theta & \cos \theta \end{bmatrix} \end{aligned} \quad (2.10)$$

Equation 2.10 may be used to determine the matrix describing a polarizer that has its transmission axis rotated by an angle  $\beta$  with respect to a polarizer that is oriented along the  $x$ -axis. The resulting matrix is found in Tab. 2.2 together with other useful optical elements.

### Müller-Stokes formalism

The polarization state of an electromagnetic wave may also be described by the Müller-Stokes formalism. Here the **Stokes parameters**, a set of four real numbers ( $S_0, S_1, S_2, S_3$ ), fully describe the intensity and the polarization state of the system. Often they are combined into a vector, the **Stokes vector**:

$$\vec{\mathbf{S}} = \begin{bmatrix} S_0 \\ S_1 \\ S_2 \\ S_3 \end{bmatrix} = \begin{bmatrix} I \\ Q \\ U \\ V \end{bmatrix} \quad (2.11)$$

All Stokes parameters refer to radiation intensities instead of complex field vectors as in the Jones formalism and are therefore more directly related to experiments. Moreover, in the Stokes formalism it is possible to represent unpolarized light. The first parameter  $S_0$  represents the total intensity of the light beam, whereas  $S_1, S_2$  and  $S_3$  are the intensity differences between the  $x$ - and  $y$ , the  $45^\circ$ - and  $-45^\circ$ , and the left- and right-circular polarization components, respectively. Using the complex amplitudes  $\tilde{A}_{x,y}$  we can write [12, 14]:

$$\begin{aligned} S_0 &= I_x + I_y = |\tilde{A}_x|^2 + |\tilde{A}_y|^2 = a_x^2 + a_y^2 \\ S_1 &= I_x - I_y = |\tilde{A}_x|^2 - |\tilde{A}_y|^2 = a_x^2 - a_y^2 \\ S_2 &= I_{45^\circ} - I_{-45^\circ} = \tilde{A}_x^* \tilde{A}_y + \tilde{A}_x \tilde{A}_y^* = 2a_x a_y \cos(\varphi_y - \varphi_x) \\ S_3 &= I_R - I_L = i(\tilde{A}_x^* \tilde{A}_y - \tilde{A}_x \tilde{A}_y^*) = 2a_x a_y \sin(\varphi_y - \varphi_x) \end{aligned} \quad (2.12)$$

optical element	Jones matrix
linear polarizer oriented in $x$ direction	$\underline{\mathbf{P}}(0^\circ) = \begin{bmatrix} 1 & 0 \\ 0 & 0 \end{bmatrix}$
linear polarizer oriented under angle $\theta$	$\underline{\mathbf{P}}(\theta) = \underline{\mathbf{R}}(-\theta) \underline{\mathbf{P}}(0^\circ) \underline{\mathbf{R}}(\theta) = \begin{bmatrix} \cos^2 \theta & \sin \theta \cos \theta \\ \sin \theta \cos \theta & \sin^2 \theta \end{bmatrix}$
quarter-wave plate fast axis horizontal	$\underline{\mathbf{Q}}(\pi/2, 0^\circ) = \begin{bmatrix} 1 & 0 \\ 0 & i \end{bmatrix}$
retarder with fast axis vertical	$\underline{\mathbf{Q}}(\pi/2, 90^\circ) = \begin{bmatrix} i & 0 \\ 0 & 1 \end{bmatrix} = \begin{bmatrix} 1 & 0 \\ 0 & -i \end{bmatrix}$
retarder (retardance $\delta$ ) fast axis rotated by $\theta$	$\underline{\mathbf{Q}}(\delta, \theta) = \begin{bmatrix} \cos^2 \theta + e^{i\delta} \sin^2 \theta & (1 - e^{i\delta}) \cos \theta \sin \theta \\ (1 - e^{i\delta}) \cos \theta \sin \theta & e^{i\delta} \cos^2 \theta + \sin^2 \theta \end{bmatrix}$

**Table 2.2:** Jones matrices for often used optical elements [14]

For completely polarized radiation the relation  $S_1^2 + S_2^2 + S_3^2 = S_0^2$  holds so only three of the four components of the Stokes vector are independent. The system is completely defined by these parameters. In the general case also including partial polarization we write:

$$S_1^2 + S_2^2 + S_3^2 \leq S_0^2 \quad (2.13)$$

Similar to the Jones formalism are Stokes vectors transformed when radiation passes an optical element, which is generally represented by a corresponding  $4 \times 4$  matrix, the **Müller matrix**  $[\mathbf{M}]$  [12]:

$$\vec{S}_2 = \begin{bmatrix} S_{2,0} \\ S_{2,1} \\ S_{2,2} \\ S_{2,3} \end{bmatrix} = [\mathbf{M}] \cdot \vec{S}_1 = \begin{bmatrix} M_{00} & M_{01} & M_{02} & M_{03} \\ M_{10} & M_{11} & M_{12} & M_{13} \\ M_{20} & M_{21} & M_{22} & M_{23} \\ M_{30} & M_{31} & M_{32} & M_{33} \end{bmatrix} \begin{bmatrix} S_{1,0} \\ S_{1,1} \\ S_{1,2} \\ S_{1,3} \end{bmatrix} \quad (2.14)$$

For a wave passing the optical element  $M_1, M_2, \dots, M_N$  Eq. 2.7 becomes:

$$\vec{S}_2 = [\mathbf{M}]_N \dots [\mathbf{M}]_2 [\mathbf{M}]_1 \vec{S}_1 \quad (2.15)$$

To calculate the matrix  $[\mathbf{M}(\theta)]$  of a polarization element, which has been rotated by an angle  $\theta$  with respect to the propagation direction, the corresponding  $4 \times 4$  version of the rotation matrix  $\underline{\mathbf{R}}(\theta)$  is used [15]:

**Table 2.3:** Collection of Stokes vectors and Müller matrices. Here *HLP*, *VLP*, *RCP* and *LCP* stand for linearly polarized (H = horizontal, V = vertical), right-circularly polarized and left-circularly polarized, respectively [15].

HLP $\vec{H}$	VLP $\vec{V}$	LP $\pm 45^\circ$ $\vec{D}$	RCP $\vec{R}$	LCP $\vec{L}$	unpol. $\vec{U}$
$\begin{bmatrix} 1 \\ 1 \\ 0 \\ 0 \end{bmatrix}$	$\begin{bmatrix} 1 \\ -1 \\ 0 \\ 0 \end{bmatrix}$	$\begin{bmatrix} 1 \\ 0 \\ \pm 1 \\ 0 \end{bmatrix}$	$\begin{bmatrix} 1 \\ 0 \\ 0 \\ 1 \end{bmatrix}$	$\begin{bmatrix} 1 \\ 0 \\ 0 \\ -1 \end{bmatrix}$	$\begin{bmatrix} 1 \\ 0 \\ 0 \\ 0 \end{bmatrix}$
Linear polarizer, transmission axis					
horizontal vertical		oriented with $\pm 45^\circ$			
$\frac{1}{2} \begin{bmatrix} 1 & \pm 1 & 0 & 0 \\ \pm 1 & 1 & 0 & 0 \\ 0 & 0 & 0 & 0 \\ 0 & 0 & 0 & 0 \end{bmatrix}$		$\frac{1}{2} \begin{bmatrix} 1 & 0 & \pm 1 & 0 \\ 0 & 0 & 0 & 0 \\ \pm 1 & 0 & 1 & 0 \\ 0 & 0 & 0 & 0 \end{bmatrix}$			
Linear polarizer, transmission axis oriented with $\theta$					
$\frac{1}{2} \begin{bmatrix} 1 & \cos 2\theta & \sin 2\theta & 0 \\ \cos 2\theta & \cos^2 2\theta & \cos 2\theta \sin 2\theta & 0 \\ \sin 2\theta & \cos 2\theta \sin 2\theta & \sin^2 2\theta & 0 \\ 0 & 0 & 0 & 0 \end{bmatrix}$					
Retarder, retardance $\delta$ , fast axis					
horizontal vertical		oriented with $\pm 45^\circ$			
$\begin{bmatrix} 1 & 0 & 0 & 0 \\ 0 & 1 & 0 & 0 \\ 0 & 0 & \cos \delta & \pm \sin \delta \\ 0 & 0 & \mp \sin \delta & \cos \delta \end{bmatrix}$		$\begin{bmatrix} 1 & 0 & 0 & 0 \\ 0 & \cos \delta & 0 & -\sin \delta \\ 0 & 0 & 1 & 0 \\ 0 & \sin \delta & 0 & \cos \delta \end{bmatrix}$			
Retarder, retardance $\delta$ , fast axis oriented with $\theta$					
$\begin{bmatrix} 1 & 0 & 0 & 0 \\ 0 & \cos^2 2\theta + \sin^2 2\theta \cos \delta & \sin 4\theta \sin^2 \delta / 2 & -\sin 2\theta \sin \delta \\ 0 & \sin 4\theta \sin^2 \delta / 2 & \sin^2 2\theta + \cos^2 2\theta \cos \delta & \cos 2\theta \sin \delta \\ 0 & \sin 2\theta \sin \delta & -\cos 2\theta \sin \delta & \cos \delta \end{bmatrix}$					

$$\begin{aligned}
 [\mathbf{M}(\theta)] &= [\mathbf{R}(\theta)] [\mathbf{M}] [\mathbf{R}(-\theta)] \\
 \text{with } [\mathbf{R}(\theta)] &= \begin{bmatrix} 1 & 0 & 0 & 0 \\ 0 & \cos 2\theta & -\sin 2\theta & 0 \\ 0 & \sin 2\theta & \cos 2\theta & 0 \\ 0 & 0 & 0 & 1 \end{bmatrix}
 \end{aligned} \tag{2.16}$$

A collection of Stokes vectors and Müller matrices for the most prominent polarization states and optical elements is shown in Tab. 2.3.

### 2.2.2 Light-matter-interaction

Optical properties and phenomena including those of optical activity can be explained on a molecular scale by the following model. A radiation field induces time-varying electric and magnetic multipole moments in a molecule. These molecular moments are themselves radiation sources and the corresponding multipolar interaction Hamiltonian is described by [16, 17]:

$$\hat{\mathbf{H}}_{int} = -\hat{\boldsymbol{\mu}} \cdot \mathbf{E} - \hat{\mathbf{m}} \cdot \mathbf{B} - \hat{\boldsymbol{\Theta}} : (\nabla \cdot \mathbf{E}) \tag{2.17}$$

Here  $\hat{\boldsymbol{\mu}}$ ,  $\hat{\mathbf{m}}$  and  $\hat{\boldsymbol{\Theta}}$  are the electric dipole, the magnetic dipole and the electric quadrupole moment operators. For a collection of  $N$  point charges  $e_i$  at position  $\mathbf{r}_i$  with mass  $m_i$  and momentum  $\mathbf{p}_i$  they are defined as [3, 18]:

$$\begin{aligned}
 \hat{\boldsymbol{\mu}} &= \sum_i e_i \mathbf{r}_i \\
 \hat{\mathbf{m}} &= \sum_i \frac{e_i}{2m_i} (\mathbf{l}_i + g_i \mathbf{s}_i) = \sum_i \frac{e_i}{2m_i} (\mathbf{r}_i \times \mathbf{p}_i + g_i \mathbf{s}_i) \\
 \hat{\boldsymbol{\Theta}} &= \frac{1}{2} \sum_i e_i (3\mathbf{r}_i \mathbf{r}_i - r_i^2 \mathbb{1})
 \end{aligned} \tag{2.18}$$

$\mathbf{l}_i$  and  $\mathbf{s}_i$  are the orbital angular momentum and the spin of the particle, whereas  $g_i$  is the  $g$ -value of the  $i$ th particle. In the definition of the quadrupole moment we also used the symmetric identity matrix  $\mathbb{1} = \sum_{\alpha\beta} \delta_{\alpha\beta}$ .

Quantum mechanical perturbation theory is now used to describe the influence of the incident electromagnetic wave on the molecule. The expectation values of the multipole operators of Eq. 2.18 are calculated to deduce the corresponding induced multipole moments as a function of the applied electric and magnetic field components, and their spatial and temporal derivatives. They are in complex notation given by [3, 18, 19]:

$$\tilde{\boldsymbol{\mu}}_{ind}(t) = \langle \Psi(t) | \hat{\boldsymbol{\mu}} | \Psi(t) \rangle = \tilde{\boldsymbol{\alpha}} \mathbf{E} + \tilde{\mathbf{G}} \mathbf{B} + \frac{1}{3} \tilde{\mathbf{A}} : (\nabla \mathbf{E}) + \dots$$

$$\begin{aligned}
\tilde{\mathbf{m}}_{ind}(t) &= \langle \Psi(t) | \hat{\mathbf{m}} | \Psi(t) \rangle = \tilde{\chi}_m \mathbf{B} + \tilde{\mathbf{G}} \mathbf{E} + \dots \\
\tilde{\mathbf{Q}}_{ind}(t) &= \langle \Psi(t) | \hat{\mathbf{Q}} | \Psi(t) \rangle = \tilde{\mathbf{A}} : \mathbf{E} + \dots
\end{aligned} \tag{2.19}$$

The fields  $\mathbf{E}$  and  $\mathbf{B}$  are taken at the molecular origin and the states  $|\Psi(t)\rangle$  are written in terms of the perturbed eigenstates of the system. The tensor  $\tilde{\alpha}$  is the electric dipole polarizability and  $\tilde{\chi}_m$  the magnetic dipole susceptibility, whereas  $\tilde{\mathbf{G}}$  is the mixed electric-magnetic dipole polarizability or optical activity tensor. The property tensors can be separated into their real and imaginary parts, i.e.  $\tilde{\alpha} = \alpha - i\alpha'$  etc.

Most linear optical phenomena such as refraction, absorption or Rayleigh light scattering are described by  $\alpha$ . The imaginary part  $\alpha'$  is none zero only in time-odd systems as in a magnetic field and it is responsible for the Faraday effect (magneto optical rotation) and magneto circular dichroism (MCD). Optical rotation, circular dichroism and other natural optical activity phenomena such as vibrational circular dichroism (VCD) and Raman optical activity (ROA) are due to the tensors  $\mathbf{G}'$  and  $\mathbf{A}$ . The latter is the electric quadrupole polarizability and contributes only in oriented samples [19]. The remaining tensors  $\mathbf{G}$  and  $\mathbf{A}'$  generate more exotic phenomena such as gyrotropic birefringence and magnetochiral effects when the system is both chiral and under the influence of a magnetic field [3,18]. Here we will restrict the subsequent discussion to the tensors  $\alpha$  and  $\mathbf{G}'$ , as these are relevant for natural optical activity phenomena. Their Cartesian components are given as [3]:

$$\begin{aligned}
\alpha_{\alpha\beta} &= \frac{2}{\hbar} \sum_{j \neq n} \omega_{jn} \text{Re} [\langle n | \hat{\mu}_\alpha | j \rangle \langle j | \hat{\mu}_\beta | n \rangle] (f + ig) \\
G'_{\alpha\beta} &= -\frac{2\omega}{\hbar} \sum_{j \neq n} \text{Im} [\langle n | \hat{\mu}_\alpha | j \rangle \langle j | \hat{m}_\beta | n \rangle] (f + ig)
\end{aligned} \tag{2.20}$$

We have used the Einstein summation convention, i.e. repeated subscripts denote summation. The frequencies  $\omega_{jn} = (E_j - E_n)/\hbar$  are the natural transition frequencies between states  $n$  and  $j$ . We also introduce the dispersion and absorption line-shape functions  $f$  and  $g$ , which are seen in Fig. 2.3 and where  $\Gamma_{jn}$  is the full width at half maximum (FWHM):

$$\begin{aligned}
f(\omega, \omega_{jn}, \Gamma_{jn}) &= \frac{(\omega_{jn} - \omega)}{(\omega_{jn} - \omega)^2 + \Gamma_{jn}^2} \\
g(\omega, \omega_{jn}, \Gamma_{jn}) &= \frac{\Gamma_{jn}}{(\omega_{jn} - \omega)^2 + \Gamma_{jn}^2}
\end{aligned} \tag{2.21}$$

In the next section we define the optical observables for some chiral and achiral phenomena which are discussed in this thesis. The observables are expressed in terms of molecular property tensors.

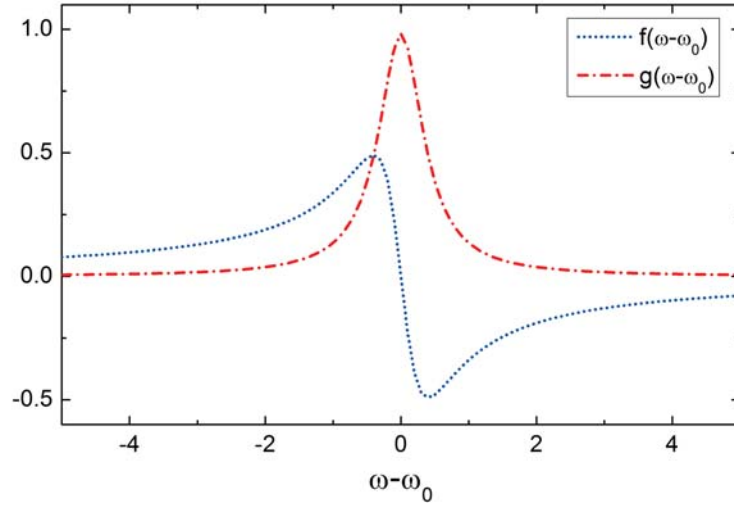


**Figure 2.3:** Dispersion and absorption lineshape functions  $f(\omega)$  and  $g(\omega)$  in the region of a resonance  $\omega_0$  (adapted from [12]).

### 2.2.3 Observables of optical activity

We restrict the discussion to isotropic samples because only liquids have been used in this thesis. In an isotropic medium the corresponding polarizability or susceptibility tensors  $\underline{\chi}$  may be replaced by appropriate scalars. These are obtained from an orientational average denoted by  $\langle \dots \rangle$ . Using the Einstein summation convention this can be expressed for tensors of rank 2 and 3 by [8]:

$$\begin{aligned}\bar{\chi}^{(1)} &= \langle \underline{\chi}^{(1)} \rangle = \frac{1}{3} \chi_{\alpha\beta}^{(1)} \delta_{\alpha\beta} = \frac{1}{3} (\chi_{xx}^{(1)} + \chi_{yy}^{(1)} + \chi_{zz}^{(1)}) \\ \bar{\chi}^{(2)} &= \langle \underline{\chi}^{(2)} \rangle = \frac{1}{6} \chi_{\alpha\beta\gamma}^{(2)} \epsilon_{\alpha\beta\gamma} = \frac{1}{6} (\chi_{xyz}^{(2)} - \chi_{xzy}^{(2)} + \chi_{yxz}^{(2)} - \chi_{yzx}^{(2)} + \chi_{zxy}^{(2)} - \chi_{zyx}^{(2)})\end{aligned}\quad (2.22)$$

For the derivation of the observables we will use the isotropic components of the molecular property tensors  $\underline{\alpha}$  and  $\underline{G}'$ , which are (Eq. 2.20 and 2.22)

$$\begin{aligned}\bar{\alpha} &= \frac{2}{3\hbar} \sum_{j \neq n} \omega_{jn} \operatorname{Re} [\langle n | \hat{\boldsymbol{\mu}} | j \rangle \cdot \langle j | \hat{\boldsymbol{\mu}} | n \rangle] (f + ig) \\ \bar{G}' &= -\frac{2}{3\hbar} \sum_{j \neq n} \omega \operatorname{Im} [\langle n | \hat{\boldsymbol{\mu}} | j \rangle \cdot \langle j | \hat{\boldsymbol{m}} | n \rangle] (f + ig)\end{aligned}\quad (2.23)$$

#### Linear optical activity

In an achiral medium the tensor  $\underline{G}'$  vanishes and the induced dipole moments up to first order in the multipolar expansion are proportional just to the molecular polarizability  $\underline{\alpha}$ .

The ensemble of induced dipoles gives rise to an average macroscopic polarization  $\mathbf{P}$  in the medium, which in linear optics is [7, 8]

$$\mathbf{P} = N \langle \boldsymbol{\mu}_{ind} \rangle = \epsilon_0 \underline{\chi}^{(1)} \mathbf{E} + \dots \quad (2.24)$$

where the angular brackets denote an average over a region containing  $N$  molecules per unit volume. The linear susceptibility  $\underline{\chi}^{(1)} = N \underline{\alpha} / \epsilon_0$  is the macroscopic analogue to the molecular polarizability. In an isotropic medium such as a liquid it is written as:

$$\bar{\chi}^{(1)} = \frac{N}{3\epsilon_0} (\alpha_{xx} + \alpha_{yy} + \alpha_{zz}) = \frac{N}{\epsilon_0} \bar{\alpha} \quad (2.25)$$

The linear refractive index  $\tilde{n}_0$  is defined as a function of the susceptibility and is in the isotropic case also a scalar

$$\tilde{n}_0 = \sqrt{1 + \bar{\chi}^{(1)}} \equiv \sqrt{\epsilon} \quad (2.26)$$

Here we introduced the dielectric permittivity  $\epsilon$ . Using the real and imaginary part for the isotropic components of  $\underline{\alpha}$  (Eqs. 2.23) we can write for the complex refractive index  $\tilde{n}_0(\omega) = n_0(\omega) + i\kappa_0(\omega)$  [12]:

$$\begin{aligned} n_0(\omega) &= 1 + \frac{N}{3\hbar\epsilon_0} \sum_{j \neq n} \text{Re} [\langle n | \hat{\boldsymbol{\mu}} | j \rangle \cdot \langle j | \hat{\boldsymbol{\mu}} | n \rangle] \frac{\omega_{jn}(\omega_{jn} - \omega)}{(\omega_{jn} - \omega)^2 + \Gamma_{jn}^2} \\ &= 1 + \frac{N}{3\hbar\epsilon_0} \sum_{j \neq n} D_{jn} \omega_{jn} f(\omega) \\ \kappa_0(\omega) &= \frac{N}{3\hbar\epsilon_0} \sum_{j \neq n} \text{Re} [\langle n | \hat{\boldsymbol{\mu}} | j \rangle \cdot \langle j | \hat{\boldsymbol{\mu}} | n \rangle] \frac{\omega_{jn} \Gamma_{jn}}{(\omega_{jn} - \omega)^2 + \Gamma_{jn}^2} \\ &= \frac{N}{3\hbar\epsilon_0} \sum_{j \neq n} D_{jn} \omega_{jn} g(\omega) \end{aligned} \quad (2.27)$$

$D_{jn}$  is the dipole strength of the transition  $|n\rangle \leftrightarrow |j\rangle$  and is related to the oscillator strength  $f_{jn}$  by a proportionality constant depending on mass  $m_e$  and charge  $-e$  of the electron [3]:

$$f_{jn} = \frac{2\omega_{jn} m_e}{3\hbar e^2} D_{jn} = \frac{2\omega_{jn} m_e}{3\hbar} \langle n | \mathbf{r} | j \rangle \cdot \langle j | \mathbf{r} | n \rangle \quad (2.28)$$

For a chiral medium it is necessary to go beyond the electric dipole approximation of Eq. 2.24 and to also consider the induced magnetic dipole moment  $\mathbf{m}_{int}$  as well as the electric quadrupole moment  $\boldsymbol{\Theta}_{int}$ . It follows that in Eqs. 2.19 we have to consider the terms due to  $\underline{\mathbf{G}}'$  and for oriented samples also  $\underline{\mathbf{A}}$ . Analog to the macroscopic polarization the macroscopic magnetization and quadrupole density are defined as

$$\mathbf{M} = N \langle \mathbf{m}_{ind} \rangle \quad \text{and} \quad \underline{\mathbf{Q}} = N \langle \boldsymbol{\Theta}_{ind} \rangle \quad (2.29)$$

The contributions from both the magnetization and the quadrupole density are considered by defining an effective polarization [7, 8]

$$\mathbf{P}_{eff} = \mathbf{P} + \frac{i}{\omega} \nabla \times \mathbf{M} - \nabla \cdot \mathbf{Q} \quad (2.30)$$

The electric field  $\mathbf{E}^{r,l}$  of a left- or right-circularly polarized plane wave traveling along the  $z$  direction is:

$$\mathbf{E}^{r,l}(z,t) = E_0 \exp[i(kz - \omega t)] (\hat{\mathbf{x}} \mp i\hat{\mathbf{y}}), \quad (2.31)$$

where the upper sign corresponds to a right-circularly polarized and the lower sign to a left-circularly polarized wave. The following relations can be deduced:

$$\dot{\mathbf{E}}^{r,l} = -i\omega \mathbf{E}^{r,l}, \quad \nabla \times \mathbf{E}^{r,l} = \pm i \frac{\omega}{c} \mathbf{E}^{r,l}, \quad \dot{\mathbf{B}}^{r,l} = \pm \frac{\omega}{c} \mathbf{E}^{r,l}$$

In an isotropic chiral medium the tensors  $\underline{\alpha}$  and  $\underline{G}'$  are replaced by their isotropic components while  $\underline{A}$  vanishes [3]. Substitution of the fields  $\mathbf{E}^{r,l}$  into the equations for the induced multipole moments (Eqs. 2.19) and using the above relations the effective polarization can be calculated to (for nonmagnetic material, i.e.  $\bar{\chi}_m = 0$ ) [7, 8]

$$\mathbf{P}_{eff}^{r,l} = \epsilon_0 \left[ \frac{N}{\epsilon_0} \bar{\alpha} \pm \frac{2Nn_0}{\epsilon_0 c} \bar{G}' \right] \mathbf{E}^{r,l} = \epsilon_0 \bar{\chi}_{eff}^{(1)} \mathbf{E}^{r,l} \quad (2.32)$$

Since Eq. 2.26 also holds in an optically active isotropic medium we obtain the refractive index for left- and right-circularly polarized light

$$\tilde{n}_{r,l} = \sqrt{1 + \bar{\chi}_{eff}^{(1)}} \approx \tilde{n}_0 \pm g_0 \quad \text{with} \quad g_0 = \frac{Nn_0}{\epsilon_0 c} \bar{G}' \quad (2.33)$$

The refractive index difference  $\delta\tilde{n} = \tilde{n}_l - \tilde{n}_r$  between both circular polarizations is therefore proportional to the isotropic components of the optical rotation tensor  $\bar{G}'$ . Similar to the linear refractive index  $\tilde{n}_0$  the real and imaginary part of  $\delta\tilde{n}$  are defined by [12]:

$$\begin{aligned} \delta n(\omega) &= \frac{4\omega}{3\hbar} \frac{Nn_0}{\epsilon_0 c} \sum_{j \neq n} R_{jn} f(\omega) \\ \delta \kappa(\omega) &= \frac{4\omega}{3\hbar} \frac{Nn_0}{\epsilon_0 c} \sum_{j \neq n} R_{jn} g(\omega) \end{aligned} \quad (2.34)$$

$R_{jn}$  is called the rotational strength for the transition  $|n\rangle \leftrightarrow |j\rangle$ :

$$R_{jn} = \text{Im} [\langle n | \boldsymbol{\mu} | j \rangle \cdot \langle j | \mathbf{m} | n \rangle] \quad (2.35)$$

It is seen in Eq. 2.23 that  $\bar{G}'$  is a (parity-odd) pseudoscalar because it can be seen as a product of an electric and a magnetic dipole transition moment. Therefore it fulfills

the requirements we defined for a chiral observable making the difference in the complex refractive index a macroscopic observable for molecular chirality. The different effects and measures resulting from this difference are characterized whether they are based on the real ( $\delta n$ ) or the imaginary part ( $\delta \kappa$ ) of the index.

### Circular Birefringence and Optical Rotation (dispersion)

The difference in the real part of the refractive index for left- and right-circularly polarized light is known as *Circular Birefringence (CB)*. It describes the phase difference between the two circular components. We now consider a plane wave linearly polarized at angle  $\beta$  (with respect to the x-axis) and traveling along  $z$ . Since linearly polarized light can be described as a superposition of left- and right-circular states the field vector can be written using Jones calculus (Eq. 2.6):

$$\mathbf{E}(z = 0, t) = \mathcal{E}_0 e^{-i\omega t} |\beta\rangle = \frac{\mathcal{E}_0}{\sqrt{2}} e^{-i\omega t} [e^{i\beta} |\mathbf{R}\rangle + e^{-i\beta} |\mathbf{L}\rangle] \quad (2.36)$$

After traveling a distance  $z_0$  in the optically active medium the field is therefore described by:

$$\begin{aligned} \mathbf{E}(z_0, t) &= \frac{\mathcal{E}_0}{\sqrt{2}} e^{i(kz_0 - \omega t)} [e^{i(\beta + \alpha)} |\mathbf{R}\rangle + e^{-i(\beta + \alpha)} |\mathbf{L}\rangle] \\ \text{with } \alpha &= \frac{\pi z_0}{\lambda} [n_l - n_r] = \frac{\pi z_0}{\lambda} \delta n \end{aligned} \quad (2.37)$$

This corresponds to a plane wave with its initial polarization rotated by an angle  $\alpha$ , and is called *Optical Rotation* or *Optical Rotatory Dispersion (ORD)* when measured as a function of wavelength. The measurement of  $\alpha$  is mostly used for the characterization of chiral media in their transparent regions. Because  $\delta n$  depends on the concentration  $C$  of the sample, the wavelength  $\lambda$ , and the pathlength  $z_0$ , it is useful to define a specific rotation [12]:

$$[\alpha]_{\lambda}^T = \frac{1}{C z_0} \alpha \quad (2.38)$$

where  $C$  is the concentration in  $\text{g cm}^{-3}$ ,  $z_0$  the pathlength in decimeter (dm) and  $T$  the temperature. The sign of the specific rotation depends on the handedness of the sample and is therefore equal and opposite for a pair of enantiomers.

### Circular Dichroism and absorption

The difference  $\delta \kappa$  in the imaginary part of the refractive index is known as *Circular Dichroism (CD)*. It manifests itself as a differential attenuation for the circular components

and is measured as a difference in absorbance. It can be expressed as a difference in the absorption coefficients for left- and right-circularly polarized light or as an ellipticity of the resulting polarization. Considering a left- or right-circularly polarized plane wave traveling along the  $z$ -axis through an absorbing optically active medium, we can write the intensity after a distance  $z_0$  as

$$I_{r,l}(z_0, \lambda) \propto |\mathbf{E}_{r,l}(z_0, t)|^2 = I_0(\lambda) \exp \left[ -\frac{4\pi z_0}{\lambda} \kappa_{r,l} \right] = I_0(\lambda) 10^{-A_{r,l}(\lambda)} \quad (2.39)$$

This is the Beer-Lambert law where in the last relation we introduced the decadic absorbance  $A(\lambda) = Cz_0\epsilon(\lambda)$ , which is defined by the concentration  $C$ , the molar absorption coefficient  $\epsilon(\lambda)$  and the path length  $z_0$  of the sample. Comparison of the exponents relates the imaginary part of the refractive index  $\kappa$  with the absorbance  $A$  and the molar absorption coefficient  $\epsilon$  [12]:

$$A_{r,l}(\lambda) = \frac{4\pi z_0}{\lambda \ln 10} \kappa_{r,l}(\lambda) \quad \text{and} \quad \epsilon_{r,l}(\lambda) = \frac{4\pi}{\lambda \ln 10 C} \kappa_{r,l}(\lambda) \quad (2.40)$$

Therefore the difference of the absorbance  $\Delta A(\lambda)$  and molar absorptivity  $\Delta\epsilon(\lambda)$  for the two circular polarization states is proportional to  $\delta\kappa(\lambda)$ . This difference results in an intensity difference for both circular polarization components which can be detected in a setup using an appropriate polarization modulation. This will be further explained in chapter 4.

When a linearly polarized light beam travels through the sample its circular components will be attenuated differently (Eq. 2.39) and the polarization state will become elliptical. The ellipticity angle, which is the angle between the major axis of the polarization ellipse and the original polarization direction, is defined as [3, 12]:

$$\psi(\lambda) = \frac{\pi z_0}{\lambda} \delta\kappa = \frac{1}{4} \ln 10 \Delta A(\lambda) = \frac{cz_0}{4} \ln 10 \Delta\epsilon(\lambda) \quad (2.41)$$

Analog to the expression for the specific rotation the density and pathlength dependence is removed by defining a specific ellipticity [12]

$$[\psi(\lambda)]_{\lambda}^T = \frac{1}{C z_0} \psi(\lambda) \quad (2.42)$$

Often the dependence on the wavelength  $\lambda$  is converted to wavenumber frequency given by  $\nu = 1/\lambda$ . Depending on the molecular transitions involved it is customary to distinguish between Electronic Circular Dichroism (ECD) and Vibrational Circular Dichroism (VCD). For measurements of CD spectra one often specifies an anisotropy or  $g_a$  factor for a specific transition to state  $a$  as the dimensionless ratio of the corresponding circular dichroism to its parent absorption. Using Eqs. 2.27 and 2.34 we can write [3, 12]:

$$g_a = \frac{\delta\kappa_a}{\kappa_a} = \frac{4n_0}{c} \frac{R_{an}}{D_{an}} \approx \frac{r}{\lambda} \quad (2.43)$$

The relation is the same for  $\Delta A$  and  $A$ , as well as  $\Delta\epsilon$  and  $\epsilon$ . The ratio  $g_a$  is a measure of the intrinsic chiral strength of the transition and therefore also of the expected signal-to-noise ratio. The factor  $g_a$  scales as the ratio of the spatial extend of the transition,  $r$ , to the wavelength  $\lambda$  of the radiation [12]. Usually  $r$  is approximately  $\sim 1$  nm, so VCD anisotropy ratios are in the range of  $10^{-3}$  to  $10^{-6}$ , whereas those of ECD are between  $10^{-2}$  and  $10^{-4}$ .

### Kramers-Kronig transform of optical activity observables

The molecular property tensors  $\underline{\alpha}$ ,  $\underline{G}'$ , and  $\underline{\Theta}$  when expressed as a sum of dispersive and absorptive parts (Eq. 2.20) belong to a class of functions known as response functions. The real (dispersive) and imaginary (absorptive) parts of such functions are related to each other by a *Kramers-Kronig transform* (KKT) [3, 12]. Because the complex refractive index  $\tilde{n}(\nu)$  and the circular index difference  $\delta\tilde{n}(\nu)$  are both functions of the above property tensors, the Kramers-Kronig transform also applies to optical activity observables. In the case of  $\tilde{n}(\nu)$  the KKT relationship is [12]:

$$\begin{aligned} n(\nu) &= 1 + \frac{2}{\pi} \mathcal{P} \int_0^\infty \frac{x \kappa(x)}{x^2 - \nu^2} dx \\ \kappa(\nu) &= -\frac{2\nu}{\pi} \mathcal{P} \int_0^\infty \frac{n(x) - 1}{x^2 - \nu^2} dx, \end{aligned} \quad (2.44)$$

where  $\mathcal{P}$  denotes the Cauchy principal value of the integral evaluated by a contour integration in the complex plane. Here we use the wavenumber  $\nu$  for the spectral dependence. The equations are the same for any other frequency variable like  $\omega$ . The integration variable  $x$  has the same units as  $\nu$ . Because the index of refraction of the vacuum is taken to be unity an additional term of 1 enters the equation for  $n(\nu)$ .

The relationship can easily be extended to the spectra of circular birefringence (CB)  $\delta n(\nu)$  and circular dichroism (CD)  $\delta\kappa(\nu)$  which are the circular polarization differences of  $n(\nu)$  and  $\kappa(\nu)$  [12]:

$$\begin{aligned} \delta n(\nu) &= \frac{2}{\pi} \mathcal{P} \int_0^\infty \frac{x \delta\kappa(x)}{x^2 - \nu^2} dx \\ \delta\kappa(\nu) &= -\frac{2\nu}{\pi} \mathcal{P} \int_0^\infty \frac{\delta n(x)}{x^2 - \nu^2} dx \end{aligned} \quad (2.45)$$

This Kramers-Kronig transform holds not only for  $\delta n(\nu)$  and  $\delta\kappa(\nu)$ , but also for any pair of equivalent CB and CD observables, such as the optical rotation  $\alpha(\nu)$  and the ellipticity

angle  $\psi(\nu)$  [12]. As can be seen from Eqs. 2.44 and 2.45 knowledge of either the dispersive or absorptive part of a response function over the entire spectrum permits the evaluation of the other part at any specified frequency  $\nu$ . And since

$$\mathcal{P} \int_0^\infty \frac{1}{x^2 - \nu^2} dx = 0,$$

it is obvious that the absorptive part of any response function vanishes if the dispersive part is constant [3]. As we shall see in chapter 5, KKT are especially useful in the IR, as here absorption bands are well separated. Thus the integral can be substituted by an integration over the absorption line.

### Optical activity in scattering

The interaction of light with matter, including optical activity, can be understood as a scattering process on molecular scale as shown in the previous sections. Therefore optical activity is also detectable in scattering experiments such as Rayleigh (elastic) or Raman (inelastic) scattering. Especially the latter has proven its usefulness for the measurement of vibrational optical activity as an alternative to absorbance measurements, i.e. measurement of VCD. Another form of optical activity is found in the Mie-Scattering of chiral colloids and macromolecules. Moreover, all optical activity observables in transmission (CD and CB) can be understood as a result of the interference of the forward scattered waves with the incident primary wave, which is called *refrangent scattering* [3].

The source of the scattered light is considered to be the emitted radiation generated by the oscillating electric and magnetic multipole moments induced in a molecule by the incident light wave (Eq. 2.19). The scattered electric field detected at a distance  $R$  large compared with the wavelength is therefore [3]:

$$\mathbf{E}^s = \frac{\omega^2 \mu_0}{4\pi R} e^{i(kR - \omega t)} \left[ (1 - \hat{\mathbf{k}}\hat{\mathbf{k}}) \cdot \underline{\tilde{\boldsymbol{\mu}}}_{ind} - \frac{1}{c} \hat{\mathbf{k}} \times \underline{\tilde{\boldsymbol{m}}}_{ind} - \frac{i\omega}{3c} (1 - \hat{\mathbf{k}}\hat{\mathbf{k}}) \cdot \hat{\mathbf{k}} : \underline{\tilde{\boldsymbol{\Theta}}}_{ind} \right] \quad (2.46)$$

Here  $\hat{\mathbf{k}}$  is the unit propagation vector in the direction of the detected wave and  $k = 2\pi/\lambda$ . The terms in  $\hat{\mathbf{k}}\hat{\mathbf{k}} \cdot \underline{\tilde{\boldsymbol{\mu}}}$  and  $\hat{\mathbf{k}}\hat{\mathbf{k}} \cdot (\hat{\mathbf{k}} : \underline{\tilde{\boldsymbol{\Theta}}})$  ensure that the wave is transverse. Using Eq. 2.19 the field of the scattered wave can be expressed in terms of the molecular property tensors and the incident plane wave  $\mathbf{E}^0$  [3]:

$$\mathbf{E}^s = \frac{\omega^2 \mu_0}{4\pi R} e^{i(kR - \omega t)} \underline{\mathbf{a}} \mathbf{E}^0 \quad (2.47)$$

The scattering tensor  $\underline{\mathbf{a}}$  for particular incident and scattering propagation vectors ( $\hat{\mathbf{k}}^0$  and  $\hat{\mathbf{k}}$ ) and pure transverse waves is given by:

$$a_{\alpha\beta} = \alpha_{\alpha\beta} - \frac{i}{c} \left( \epsilon_{\gamma\delta\beta} \hat{k}_\delta^0 G'_{\alpha\gamma} - \epsilon_{\gamma\delta\alpha} \hat{k}_\delta G'_{\gamma\beta} \right) - \frac{i\omega}{3c} \left( \hat{k}_\gamma^0 A_{\alpha\gamma\beta} - \hat{k}_\gamma A_{\beta\gamma\alpha} \right) + \dots \quad (2.48)$$

Transmission observables like simple absorption, optical rotation or circular dichroism can be understood as the interference of the forward scattered part of  $\mathbf{E}^s$  (i.e.  $\hat{\mathbf{k}} = \hat{\mathbf{k}}^0$ ) and the incident wave  $\mathbf{E}^0$ . Any intensity or polarization change arising from refringent scattering can be considered if the final field  $\mathbf{E}^f = \mathbf{E}^0 + \mathbf{E}^s$  is used to calculate the four Stokes parameters defined in Eq. 2.12. Detailed calculations of the different transmission observables are given in [3].

Optical activity and polarization effects are also detectable in light scattering processes which do not involve the interference between the unscattered and forward-scattered components. These cover Rayleigh, Mie and Raman scattering in all other directions, and also forward Raman scattering due to the different frequencies of the scattered and unscattered fields. Again a light wave propagating along the  $z$  axis is incident upon a scatterer (molecule) at the origin of the right-handed coordinate system  $x, y, z$ . We consider the wave scattered at an arbitrary angle  $\theta$  in the  $yz$  plane and calculate its polarization and intensity using the Stokes parameters. The scattered wave propagates along the unit vector  $z'$  of second coordinate system  $x', y', z'$ , with [3]:

$$x' = x, \quad y' = y \cos \theta - z \sin \theta, \quad z' = y \sin \theta + z \cos \theta \quad (2.49)$$

These relations are used to calculate the Stokes parameters (Eq. 2.12) of the scattered wave  $\mathbf{E}^s$  in the  $x, y, z$  system [3]:

$$\begin{aligned} S_0^s &= E_x^s E_x^{s*} + E_y^s E_y^{s*} \cos^2 \theta + E_z^s E_z^{s*} \sin^2 \theta - \left( E_y^s E_z^{s*} + E_z^s E_y^{s*} \right) \cos \theta \sin \theta \\ S_1^s &= E_x^s E_x^{s*} - E_y^s E_y^{s*} \cos^2 \theta - E_z^s E_z^{s*} \sin^2 \theta - \left( E_y^s E_z^{s*} + E_z^s E_y^{s*} \right) \cos \theta \sin \theta \\ S_2^s &= - \left( E_x^s E_y^{s*} + E_y^s E_x^{s*} \right) \cos \theta + \left( E_x^s E_z^{s*} + E_z^s E_x^{s*} \right) \sin \theta \\ S_3^s &= -i \left( E_x^s E_y^{s*} - E_y^s E_x^{s*} \right) \cos \theta + i \left( E_x^s E_z^{s*} - E_z^s E_x^{s*} \right) \sin \theta \end{aligned} \quad (2.50)$$

Using Eq. 2.47 for the electric field of the scattered wave  $\mathbf{E}^s$  the Stokes parameters can be expressed in terms of the scattering tensor  $\underline{\mathbf{a}}$  and the Stokes parameters of the incident wave  $\mathbf{E}^0$ , as shown in [3]. Explicit expressions in terms of the dynamic molecular property tensors  $\underline{\boldsymbol{\alpha}}$ ,  $\underline{\mathbf{G}}'$  and  $\underline{\mathbf{A}}$  are found by regarding their contributions to the scattering tensor  $\underline{\mathbf{a}}$  (Eq. 2.48). For isotropic samples like fluids and in the absence of external fields products of tensor components have to be averaged over all orientations of the molecule, analogue to Eq. 2.22 [3].

Scattering of randomly oriented achiral molecules at transparent frequencies is usually dominated by the real dynamic polarizability  $\underline{\alpha}$ . Only components of the tensor product  $\underline{\alpha}\underline{\alpha}^*$  contribute to the Stokes parameters of the scattered wave. In contrast, Rayleigh and Raman scattering from isotropic chiral samples can show additional polarization effects. These are mainly due to the interference between waves generated by  $\underline{\alpha}$  and waves generated by  $\underline{\mathbf{G}}'$  or  $\underline{\mathbf{A}}$ . Therefore components of the tensor products  $\underline{\alpha}\underline{\mathbf{G}}'^*$  and  $\underline{\alpha}\underline{\mathbf{A}}^*$  are added to the scattered Stokes parameters (Eq. 2.50) [3]. Although  $\underline{\mathbf{A}}$  only contributes to optical rotation or circular dichroism in oriented samples, it is also part of scattering optical activity even in isotropic samples, where the corresponding terms are on the same order of magnitude as those from  $\underline{\mathbf{G}}'$ . Terms in  $\underline{\mathbf{G}}'^2$  and  $\underline{\mathbf{A}}^2$  are also found in the Stokes parameters of the scattered field, but they are expected to be about  $10^{-6}$  times the terms in  $\underline{\alpha}^2$  and even  $10^{-3}$  times terms in  $\underline{\alpha}\underline{\mathbf{G}}'^*$  and  $\underline{\alpha}\underline{\mathbf{A}}^*$  [3, 20].

An appropriate observable in scattering optical activity is the difference in intensities scattered at an angle  $\theta$  for both circular polarizations, named *Circular Differential Scattering Intensity (CDSI)*:

$$CDSI(\theta) = \frac{I_r(\theta) - I_l(\theta)}{I_r(\theta) + I_l(\theta)} \propto \frac{S_0^{s,r} - S_0^{s,l}}{S_0^{s,r} + S_0^{s,l}} \quad (2.51)$$

where  $S_0^{s,r}$  and  $S_0^{s,l}$  are the Stokes parameters of the scattered field for right- or left-circularly polarized incident light. For an isotropic chiral sample neat equations for the scattering in (near) forward, backward and  $90^\circ$ -direction can be found in [3, 18, 20]. For  $90^\circ$  scattering we have for example:

$$CDSI(90^\circ) = \frac{2 \left( 13\alpha_{\alpha\beta}G'_{\alpha\beta}^* - \alpha_{\alpha\alpha}G'_{\beta\beta}^* - \frac{1}{3}\omega\alpha_{\alpha\beta}\epsilon_{\alpha\gamma\delta}A_{\gamma\delta\beta}^* \right)}{c \left( 13\alpha_{\lambda\mu}\alpha_{\lambda\mu}^* - \alpha_{\lambda\lambda}\alpha_{\mu\mu}^* \right)} \quad (2.52)$$

CDSI can also be found in the Mie scattering of chiral colloids and macromolecules even if only contributions of  $\underline{\alpha}$  are considered. A macromolecule or colloid is considered as an arbitrary set of polarizability tensors  $\underline{\alpha}_i$ , where each emits a wave according to Eq. 2.46. The total scattered field  $\underline{\mathbf{E}}^s$  is the sum over all fields emitted by the polarizabilities. Using Eq. 2.31 for a left- or right-circularly polarized incident plane wave the scattered intensities  $I_{l,r}$  can be calculated. If considering an isotropic suspension of colloids or macromolecules, the difference and the sum of  $I_r$  and  $I_l$  have to be averaged over all orientations of the scatterer. Further details are given in chapter 6 where this differential scattering is used for the characterization of artificial chiral colloids. In contrast to other chiroptical methods (CD or ORD), CDSI of chiral colloids can give information about structural elements on the order of the wavelength used in the experiment and is not restricted to spectral regions within absorption bands of the scatterers [21].





# 3

## Chiral Refractometry

One hallmark of natural and magnetic optical activity is the difference in the real part of the refractive indices for circularly polarized light (Circular Birefringence), which causes the rotation of the plane of polarization of a linearly polarized light beam traversing an optically active medium (Sec. 2.2.3). The small difference typically found in optically active systems can be detected in transmission (polarimetry) [3]. However, as Fresnel first proposed, it may also be detected in refraction [22]. A linearly polarized light beam incident at an interface between a chiral and an achiral medium will split into its two circular polarization components, as the two components refract with different angles of refraction [22, 23]. Optical activity measurements at interfaces require potentially much smaller fluid volumes than transmission experiments [23–28]. For chemical and pharmaceutical applications it is of interest to measure small optical activities (with correspondingly small refractive index differences) in minute liquid samples.

The sensitivity of the refraction scheme now depends on how small a separation between the left- and right-circular components can be registered on a detector [22, 23, 27]. Various methods have been tested and compared with each other and a distinction is drawn between two different measurement principles to detect the small beam deflections:

- (1) *Position Methods*, and
- (2) *Intensity Methods*

The *Position Methods* include the direct detection of the beam position with a position sensitive detector and appropriate polarization modulation, whereas the *Intensity Methods* make use of interferometric-like intensity measurements to detect the beam deflection (also called *Weak Value Amplification*). The corresponding details are presented in the following sections. Part of this chapter has been published in [P1, P2].

### 3.1 Optical activity induced light beam deflection and splitting

We now consider the following two situations to calculate the angular splitting  $\delta\theta$  of a linearly polarized light beam as a function of the refractive index difference  $\delta n$  between circularly polarized beam components. The light beam is either travelling from the non chiral to the chiral medium (named external refraction, Fig. 3.1a) or vice versa (called internal refraction, Fig. 3.1b). In what follows  $n = (n^+ + n^-)/2$  is the mean refractive index of the chiral liquid and  $n^{+,-}$  the refractive indices for the circular polarizations.

#### 3.1.1 Calculation of light beam splitting

External refraction: achiral to chiral medium

Both circularly polarized beam components must independently obey Snell's Law of refraction. With the difference in the refractive index  $\delta n = n^+ - n^-$  and the angular splitting  $\delta\theta = \theta_+ - \theta_-$  this can be expressed as:

$$n_0 \sin \theta_0 = n^+ \sin \theta_+ = (n + \delta n/2) \sin (\theta + \delta\theta/2) \quad (3.1a)$$

$$n_0 \sin \theta_0 = n^- \sin \theta_- = (n - \delta n/2) \sin (\theta - \delta\theta/2) \quad (3.1b)$$

Here  $n_0$  is the refractive index of the achiral surrounding. This equation system can be solved by subtracting both equations from one another and using fundamental trigonometric relations. Since  $\delta\theta$  is small, the approximations  $\sin \delta\theta/2 \approx \delta\theta/2$  and  $\cos \delta\theta/2 \approx 1$  are true and we obtain the following expression for the angular splitting  $\delta\theta$  [23]:

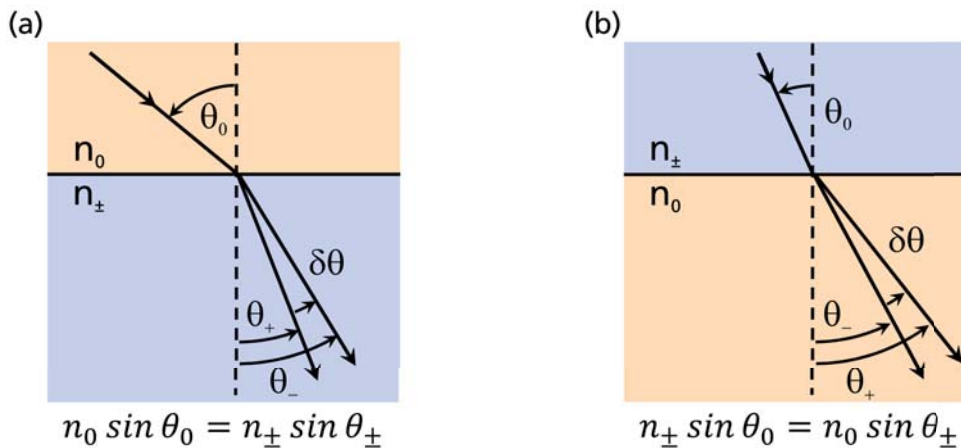


**Figure 3.1:** Schematic drawing for the refraction of a linearly polarized light beam at (a) an achiral-chiral and (b) a chiral-achiral interface (adapted from [23])

$$\delta\theta \approx -\frac{\delta n}{n} \tan \theta \quad (3.2)$$

### Internal refraction: chiral to achiral medium

As before, Snell's Law of refraction must be independently fulfilled by both circular polarization components, so we get a similar equation system:

$$(n + \delta n/2) \sin \theta_0 = n_0 \sin (\theta + \delta\theta/2) \quad (3.3a)$$

$$(n - \delta n/2) \sin \theta_0 = n_0 \sin (\theta - \delta\theta/2) \quad (3.3b)$$

Subtracting both equations from one another and using the same trigonometric relations and approximations than for the external refraction we get the following expression for the angular splitting  $\delta\theta$ :

$$\delta\theta \approx \frac{\delta n \sin \theta_0}{n_0 \cos \theta} \quad (3.4)$$

### Spatial separation and splitting enhancement

A distance  $d$  behind the chiral-achiral interface the two refracted beams are in both cases separated by a distance  $2\delta x$ , which is

$$\delta x(d) = d \cdot \tan \left[ \frac{\delta\theta_{int,ext}}{2} \right], \quad (3.5)$$

where  $\delta\theta_{int,ext}$  is the angular splitting observed for the internal or external refraction, respectively. This separation can be detected in different ways to measure  $\delta\theta$  and therefore  $\delta n$ . Moreover, the magnitude of the angular separation  $\delta\theta$  for both, the internal and external refraction, depends on the angle of incidence  $\theta_0$ . Figure 3.2 shows the angular splitting for both cases for different values of  $\theta_0$ . For the calculation we considered an interface between air ( $n_0 = 1.0$ ) and a chiral medium with a mean refractive index of  $n = 1.77$  and a circular birefringence of  $\delta n = 1 \times 10^{-6}$ .<sup>1</sup> As a result, an enhancement of  $\delta\theta$  takes place for the internal refraction when the angle of incidence is taken to be close to the angle of total internal reflection (TIR) [29]. Therefore, the TIR condition for internal refraction for SF11-glass has been used in the subsequent measurements with  $\theta_0 = 30^\circ$ .

Another enhancement can be achieved by using a diffraction grating after the chiral sample.

<sup>1</sup> This choice of parameters is motivated by the given experimental settings, which will be demonstrated in the proceeding sections.

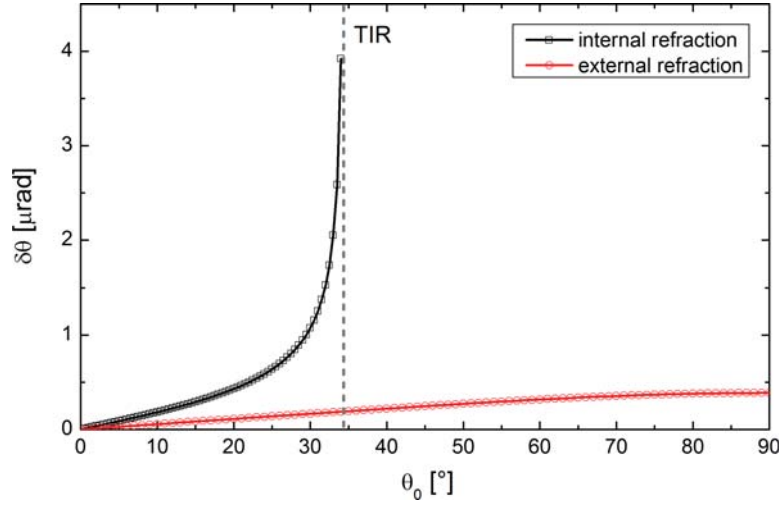


**Figure 3.2:** Angular separation  $\delta\theta$  for internal and external refraction at an interface between air ( $n_0 = 1.0$ ) and a chiral medium with a mean refractive index of  $n = 1.77$  and a circular birefringence of  $\delta n = 1 \times 10^{-6}$

This is due to the strong dependence of the diffraction angles on the angle of incidence, especially for higher diffraction orders with angles close to  $90^\circ$ . This has been demonstrated by Ghosh et al. [30] but has not been used here.

### 3.1.2 Magneto optical activity: The Faraday Effect

Any isotropic medium becomes optically active and uniaxial in the presence of a longitudinal magnetic field. This is also known as the Faraday effect. We consider the Faraday effect in a glass prism as a model system for an optically active solution with an angled interface. The plane of polarization of a linearly polarized electromagnetic wave at wavelength  $\lambda$  is rotated by an angle  $\alpha$  as the wave propagates a distance  $l$  inside the medium along the direction of the field, which is

$$\alpha = \frac{\pi l}{\lambda} (n^+ - n^-) = VB l \quad (3.6)$$

where  $V$  is the frequency dependent Verdet constant and  $B$  is the magnetic field strength. Using equations 3.2 and 3.4 the angular divergence  $\delta\theta$  between the two refracted circular polarization components can be written as [23, 28]:

$$\delta\theta_{int} \approx -\frac{VB\lambda}{\pi n} \tan \theta \quad (\text{external refraction}) \quad (3.7a)$$

$$\delta\theta_{ext} \approx \frac{VB\lambda \sin \theta_0}{\pi n_0 \cos \theta} \quad (\text{internal refraction}) \quad (3.7b)$$

The angular divergence  $\delta\theta$  is now directly proportional to the magnetic optical activity, i.e. the magnetic field strength  $B$  and the Verdet constant  $V$  of the glass prism. When  $V$  is known, the optical activity of the glass prism, i.e. the magnitude of  $\delta\theta$ , can be precisely controlled by tuning the magnetic field strength  $B$ .

Therefore, a glass prism inside a longitudinal magnetic field induced by an electromagnet serves as a model system for optical activity to test different detection methods for the angular splitting. In all subsequent measurements the prism was made from SF11-glass ( $n = 1.77$  and Verdet constant  $V = 14$  rad/Tm at  $\lambda = 633$  nm) and the magnetic field strength was detected with a Gaussmeter (MAGSYS HGM09, resolution 0.1 Gauss, accuracy  $\pm 0.5\%$ ).

## 3.2 Position method: dual polarization modulation

The first method that has been tested is the *Position Method*. The small angular deflection of the probe beam after passing the chiral / achiral interface is directly measured with a position sensitive detector. Fischer et al. [23] demonstrated with a simple setup the first measurements of optical activity making use of such a position method. By using a Photo Elastic Modulator (PEM) for the modulation between circular polarization states combined with a lock-in detection scheme they were able to measure the Optical Rotary Dispersion (ORD) of limonene and carvone. Furthermore, angular deviations  $\delta\theta$  of  $\leq 1$   $\mu$ rad have been measured with a standard deviation of  $\sim 10$  nrad. Unfortunately the modulator itself gives rise to artefacts due to beam deflections ( $\approx \mu$ rad) and/or interference effects modulated at the PEM frequency. Both arise from surface deformations of the PEM-crystal due to the modulation process and cause deviations of the data points. Nevertheless, being a versatile tool providing a variety of polarization modulation schemes a modified setup has been implemented using an additional PEM to minimize these artifacts.

### 3.2.1 Experimental setup

The setup used for the dual polarization modulation is shown in Figure 3.3. The light of a Helium-Neon (HeNe) laser with a wavelength of  $\lambda = 633$  nm and an optical output power of  $P = 10$  mW is at first linearly polarized by a polarizer with  $\beta_{pol} = 45^\circ$ . After passing the first PEM with its modulation axis horizontally ( $\beta_{PEM1} = 0^\circ$ ) the light travels through a Quarter-wave plate (QWP) and a second PEM both with their principle axis oriented parallel to the first polarizer, i.e.  $\beta_{QWP} = \beta_{PEM2} = \beta_{pol} = 45^\circ$ . The polarization of the light is now modulated between the circular states at the difference frequency  $\Delta f = |f_{PEM1} - f_{PEM2}|$  of the modulators with  $f_{PEM1} = 50$  kHz and  $f_{PEM2} = 47$  kHz, as will be shown in the next section. The polarization modulated light now enters the opti-

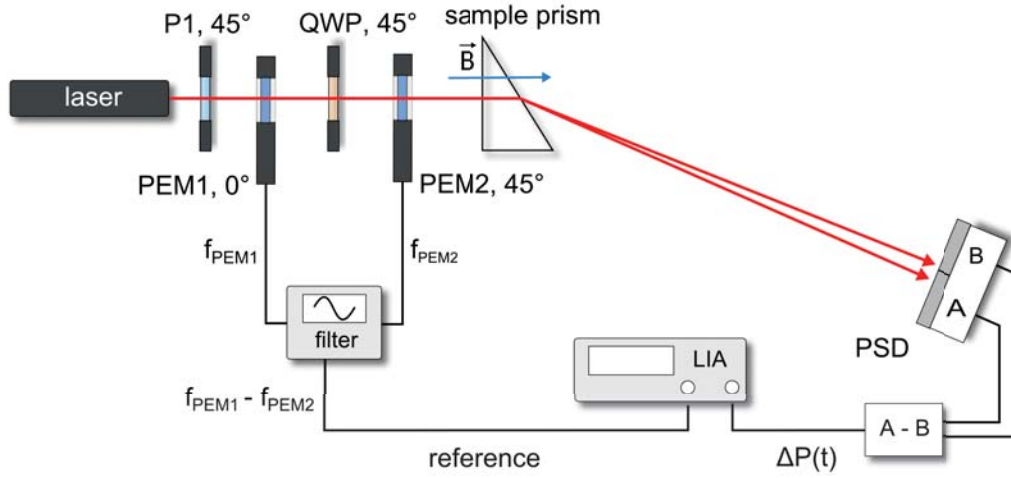


**Figure 3.3:** Setup used for Dual-polarization-Modulation. See text for details.

cally active wedge (i.e SF-11 prism inside a magnetic field, Sec. 3.1.2) and the circularly polarized light beams are refracted at the angled exit surface. A position sensitive detector (PSD, UDT SPOT-9DMI) is placed a distance  $d$  behind the prism to track the position of the beam and detect any deflections. Therefore the induced photo currents from both halves of the PSD are detected and transformed to the corresponding voltages using a transimpedance amplifier. After generating the sum and difference voltages electronically the signals are detected with a lock-in amplifier (LIA, Stanford Research Systems SR830) locked to  $\Delta f$ . The reference signal for the LIA is produced by multiplying and low-pass filtering both reference signals of the PEMs.

### 3.2.2 Model and calculations

Considering the setup described in the previous section we will now take a closer look at the polarization modulation using the Stokes-Müller-formalism. The laser emits horizontally polarized light defined by (Sec. 2.2.1)

$$\vec{H} = \begin{bmatrix} 1 \\ 1 \\ 0 \\ 0 \end{bmatrix} \quad (3.8)$$

The two PEMs are operated with the same retardation of  $\pi/2$ , so that the light component that modulates between left and right circular at the difference frequency of the two modulators is detected. The resulting Stokes-vector is calculated by successively multiplying the Müller matrices for each component to this vector:

$$\begin{aligned}\vec{S}_{out} &= [\mathbf{PEM}_{2,45^\circ}] \cdot [\mathbf{QWP}_{45^\circ}] \cdot [\mathbf{PEM}_{1,0^\circ}] \cdot [\mathbf{LP}_{45^\circ}] \cdot \vec{H} \\ &= \begin{bmatrix} 1 \\ -\cos[\delta_{M2}(t)] \sin[\delta_{M1}(t)] \\ \cos[\delta_{M1}(t)] \\ -\sin[\delta_{M2}(t)] \sin[\delta_{M1}(t)] \end{bmatrix}\end{aligned}\quad (3.9)$$

For the calculation the corresponding matrices defined in Section 2.2.1 have been used. The Photoelastic Modulator (PEM) can be described as a retarder with a time-varying retardation oscillating at a circular frequency  $\omega = 2\pi f$ :

$$\delta_{M1,2}(t) = \delta_{1,2} \sin[\omega_{1,2}t] \quad (3.10)$$

The expression for  $[S_{out}]$  can further be simplified using the following relations:

$$\begin{aligned}\cos[a \sin(bt)] &= J_0(a) + 2J_2(a) \cos(2bt) + \dots \\ \sin[a \sin(bt)] &= 2J_1(a) \sin(bt) + \dots\end{aligned}\quad (3.11)$$

The functions  $J_0(x)$ ,  $J_1(x)$  and  $J_2(x)$  are the Bessel functions of the zeroth, first, and second order, respectively. So we have:

$$\vec{S}_{out} = \begin{bmatrix} 1 \\ -2J_1(\delta_1)J_0(\delta_2) \sin(\omega_1t) - 4J_1(\delta_1)J_2(\delta_2) \sin(\omega_1t) \cos(2\omega_2t) \\ J_0(\delta_1) + 2J_2(\delta_1) \cos(2\omega_1t) \\ -4J_1(\delta_1)J_1(\delta_2) \sin(\omega_1t) \sin(\omega_2t) \end{bmatrix}\quad (3.12)$$

Since the fourth component of  $[S_{out}]$  is defined as the difference between the intensities of the circularly polarized beam components we will focus our attention on this component. It can be written as:

$$\vec{S}_{out,4} = -2J_1(\delta_1)J_1(\delta_2) \{ \cos[(\omega_1 - \omega_2)t] - \cos[(\omega_1 + \omega_2)t] \} \quad (3.13)$$

Equation 3.13 contains two time-varying terms, one oscillating with the difference and one at the sum frequency. An example calculation of  $[S_{out}]_4$  for  $f_1 = 47$  kHz and  $f_2 = 50$  kHz is shown in Fig. 3.4. The polarization of the laser beam is modulated between the circular states at the difference frequency  $\Delta f = f_1 - f_2$ . The component oscillating at the sum frequency is suppressed by using a lock-in amplifier. The displacement  $\delta x$  of the beam induced by the circular birefringence  $\delta n$  of the optically active sample will oscillate with  $\Delta\omega = 2\pi\Delta f$  with its amplitude  $\delta x_0$  proportional to  $\delta n$

$$\delta x(t) = -2J_1(\delta_1)J_1(\delta_2)\delta x_0 \cos[\Delta\omega t] \quad (3.14)$$

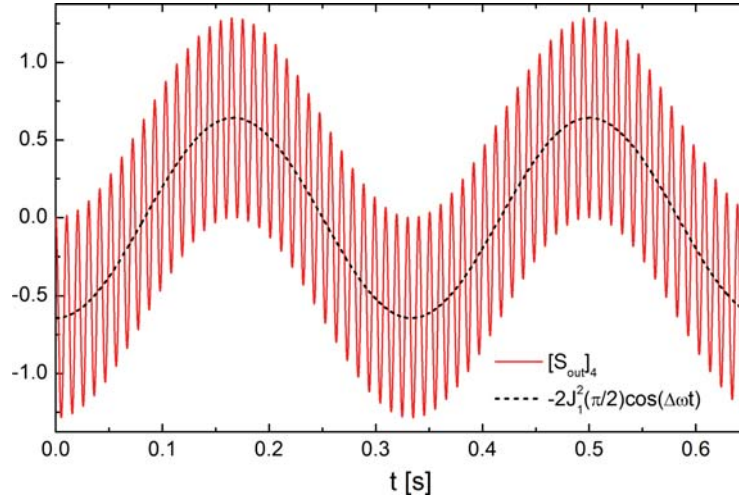


**Figure 3.4:** Example calculation of  $[S_{out}]_4$  for  $f_1 = 47$  kHz,  $f_2 = 50$  kHz and a quarterwave retardation for both PEMs, i.e.  $\delta_1 = \delta_2 = \pi/2$ . The signal is now composed of two frequency components, one at the difference and one at the sum frequency.

All other unwanted beam displacements arising from the surface deformations of the PEMs are expected to oscillate at frequencies other than  $\Delta f$ , so  $\delta x$  can be separated from these artifacts. The deflection  $\delta x$  is measured with a position sensitive detector. The detected intensity of the deflected laser beam with a Gaussian beam profile can be written as:

$$I_\delta(x,y) = I_0 \exp \left[ -2 \frac{(x + \delta x)^2 + y^2}{w^2} \right], \quad (3.15)$$

where  $w$  is the beam radius. The power  $P_A$  and  $P_B$  incident on the two halves of the PSD is calculated by an appropriate integration of  $I_\delta(x,y)$

$$P_A(t) = \int_{-\infty}^{\infty} dy \int_{-\infty}^0 I_\delta(x,y) dx \quad \text{and} \quad P_B(t) = \int_{-\infty}^{\infty} dy \int_0^{\infty} I_\delta(x,y) dx \quad (3.16)$$

Therefore we obtain for the power difference  $\Delta P = P_B - P_A$  detected by the PSD:

$$\Delta P(t) = -P_0 \operatorname{erf} \left[ \frac{\sqrt{2}\delta x(t)}{w} \right] \quad \text{with} \quad P_0 = \frac{1}{2} \pi w^2 I_0 \quad (3.17)$$

Both, the difference  $\Delta P$  and the power of the laser  $P_0$  can be expressed in terms of the difference  $\Delta U$  and the sum  $\Sigma U$  of the generated voltages  $U_{A,B}$ :

$$\Delta P = \frac{\Delta U}{10 \cdot a_{trans} \cdot g} \quad \text{and} \quad P_0 = \frac{\Sigma U}{2.5 \cdot a_{trans} \cdot g} \quad (3.18)$$

Here  $a_{trans} = 4 \times 10^4$  V/A is the gain factor of the transimpedance amplifier and  $g = 0.48$  A/W is the responsivity of the detector element. In addition  $\Delta U$  and  $\Sigma U$  are amplified by a factor of 10 and 2.5, respectively. While  $\Delta U$  is fed into the signal input of the LIA  $\Sigma U$  is detected with one of the auxiliary inputs. Since the measured lock-in amplitude  $R_{\Delta U}$  is an RMS- not a peak-to-peak-value we have to multiply it by  $\sqrt{2}$ . Our final result for the amplitude  $\delta x_0$  of the displacement is therefore

$$\delta x_0 = \frac{w}{2\sqrt{2}J_1^2(\delta)} \operatorname{erf}^{-1} \left[ \frac{\sqrt{2}R_{\Delta U}}{4\Sigma U} \right], \quad (3.19)$$

where  $\operatorname{erf}^{-1}$  is the inverse of the error function  $\operatorname{erf}(x) = (2/\sqrt{\pi}) \int_0^x e^{-t^2} dt$ . We also assumed that both PEMs have the same retardation  $\delta = \delta_1 = \delta_2 = \pi/2$ .

### 3.2.3 Measurements

To test the Dual Polarization Modulation method the following measurements have been performed. At first the PSD was placed at a distance  $d = 0.6$  m behind the SF11 sample prism. Four consecutive measurements have been taken, where the magnetic field strength  $B$  was changed in steps of  $\Delta B \approx 27$  Gauss. Each data point is an average of 100 lock-in

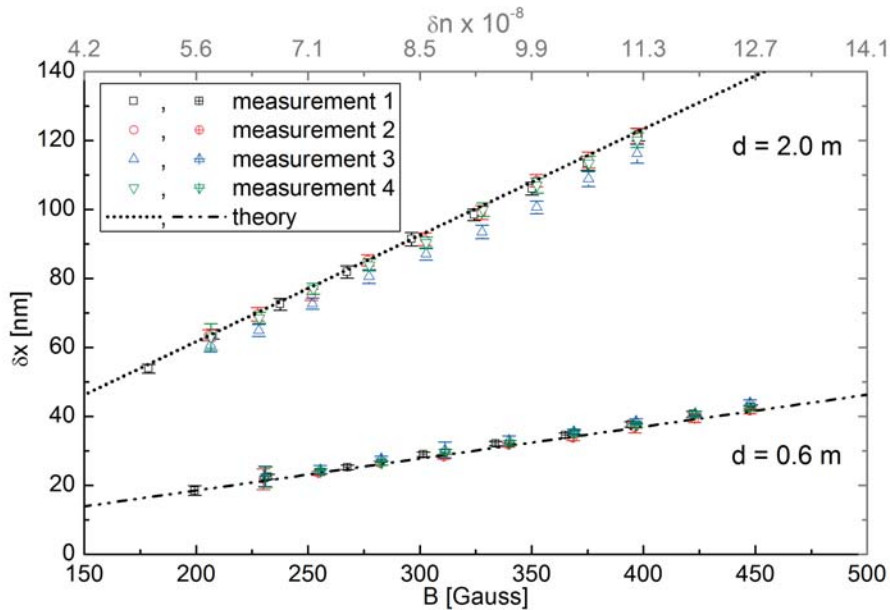


**Figure 3.5:** Measurement results using the Dual Polarization Modulation technique for two distances  $d$  between the prism and the PSD. As the distance increases so does the measured beam separation  $\delta x$ . The theoretically predicted values are also shown (dashed and dotted lines).

values, which have been taken in 100ms time intervals. The same procedure was now performed with an increased distance between prism and PSD of  $d = 2.0$  m. All measurement results are shown in Fig. 3.5 together with the theoretically predicted values calculated using Eq. 3.5. The error bars shown correspond to the standard deviation also calculated from the averages. The measurements are in agreement with theory. The shift of the first measurement of each data set is due to the magnetization of the iron core of the electromagnet. The slope of the measurement line increases as the distance  $d$  between prism and detector is increased which is what the theory predicted (see Eq. 3.5). The data has been corrected for the offset, which is introduced through the PEMs as described above. It was determined by simply using a linear fit of the uncorrected data and by taking the intercept with the  $y$ -axis ( $B = 0$  Gauss). For all measurements it was on the order of  $\delta x_{offset} \approx 50$  nm ( $d = 0.6$  m) to  $\delta x_{offset} \approx 73$  nm ( $d = 2.0$  m). Changes of  $\delta n \sim 1 \times 10^{-8}$  in the circular birefringence are well resolved.

### 3.3 Intensity method: weak value amplified detection

Ideally, a measurement yields distinct (eigen)values that can be recorded using a suitable measuring device. Aharonov, Albert, and Vaidman (AAV) considered the case of “weak measurements” in quantum mechanics, where the measurement is unable to distinguish between (eigen)values after a weak perturbation [31, 32]. AAV showed that, if prior to the measurement the system is prepared in a well-defined state, then a suitable post-selection can give rise to large expectation values and thereby permit the (eigen)values to be distinguished. They considered the displacement of the spin-components of a Gaussian ensemble of spin- $\frac{1}{2}$  particles that are detected on a screen after passing through two orthogonal Stern-Gerlach magnets. An optical weak value measurement was performed by Ritchie et al. [33], who showed that by carefully pre- and post-selecting the polarization state of a light beam, a weak value amplification scheme can be used to detect a lateral beam shift of  $0.64\mu\text{m}$  between the two linear-polarization components induced by a birefringent crystal. Hosten and Kwiat [34] reported the observation of an optical analog of the Spin Hall effect, where the lateral displacement of the two orthogonal linearly-polarized components of a light beam was measured via weak value amplification with  $\sim \text{\AA}$  sensitivity. Dixon et al. [35] similarly showed that beam deflections down to  $0.4$  prad could be detected in a Sagnac interferometer.

Here, it is shown how weak value amplification can be adapted to measure optical activity. Whilst weak value amplification has been used to determine small lateral beam shifts, it is difficult to determine the handedness of a chiral liquid with a conventional weak value measurement, as reported in the literature. Therefore a weak value measurement is combined either with an appropriate polarization modulation or with a heterodyne detection. This

enables the measurement of the handedness (sign) of weak optically active media whilst still benefiting from an increase of up to  $10^6$  in the beam separation opposed to the case without a weak value amplification.

### 3.3.1 Weak value amplified measurement of small beam deflections

Weak measurements in optics that are based on polarization entail three steps: (1) preparation of the system in a defined (polarization) state, which is termed *pre-selection*, (2) a *weak interaction* giving rise to a (small) polarization-dependent beam deflection, and finally (3) *post-selection* of the final (polarization) state, which is chosen to be nearly orthogonal to the initial state. In our case the weak interaction is due to optical activity. A coherent light beam with a Gaussian beam profile is linearly polarized and incident upon an optically active wedge (see Fig. 3.6). Here the wedge's optical activity is introduced by the Faraday effect as described before (Sec. 3.1.2), but the theory is the same for natural optical activity, e.g. a chiral liquid in a triangular cuvette. The linear polarization state of the light is equivalent to a superposition of two circular polarization states (left- and right-circular) which experience different refractive indices in the wedge.

This makes them refract at different angles of refraction at the second interface such that the light beam splits into two [23] as shown in Sec. 3.1. Since the handedness of the optically active medium determines which of the two circular components has the larger refractive index and hence the larger angle of refraction, this information is crucial in natural optical activity measurements. We will now first explain how 'conventional' weak measurements can be used to detect minute angular beam deflections. In the subsequent sections the discussion is extended to describe how to retain the sign information and hence the handedness of the optically active medium in a weak measurement with an orthogonal post-selection. Although the weak scheme was initially proposed for quantum measurements [31], the same principle can be understood using a classical treatment [32, 33, 36], as is used here.

A light beam is assumed to propagate along the  $z'$  direction and is taken to be linearly polarized along  $x'$ , denoted by  $|\mathbf{H}'\rangle$  (Fig. 3.6 and Fig. 3.7). Using Jones calculus the complex electric-field vector after the pre-selection polarizer is:

$$\mathbf{E}_1(x', y', z') = \mathcal{E}(x', y') e^{i\mathbf{k}_0 \cdot \mathbf{r}'} |\mathbf{H}'\rangle = \mathcal{E}_0 \exp \left[ -\frac{x'^2 + y'^2}{w^2} \right] e^{ik_0 z'} \begin{bmatrix} 1 \\ 0 \end{bmatrix} \quad (3.20)$$

where  $w$  is the radius of the Gaussian beam and  $\mathbf{k}_0 \parallel \hat{\mathbf{z}}'$  the wavevector with  $|\mathbf{k}_0| = 2\pi n_0/\lambda$ . After refraction at the optically active prism surface the beam now propagates along  $z$  (Fig. 3.7). The weak interaction at the interface causes an angular deflection of the left- (−) and right- (+) circularly polarized beam components. Their angular beam separation  $\delta\theta = \theta_- - \theta_+$  is proportional to the difference of their index of refraction  $\delta n$  (see Eq. 3.4). For neat (undiluted) chiral liquids  $|\delta\theta|$  is already  $\lesssim 10^{-6}$  rad and the beam separation

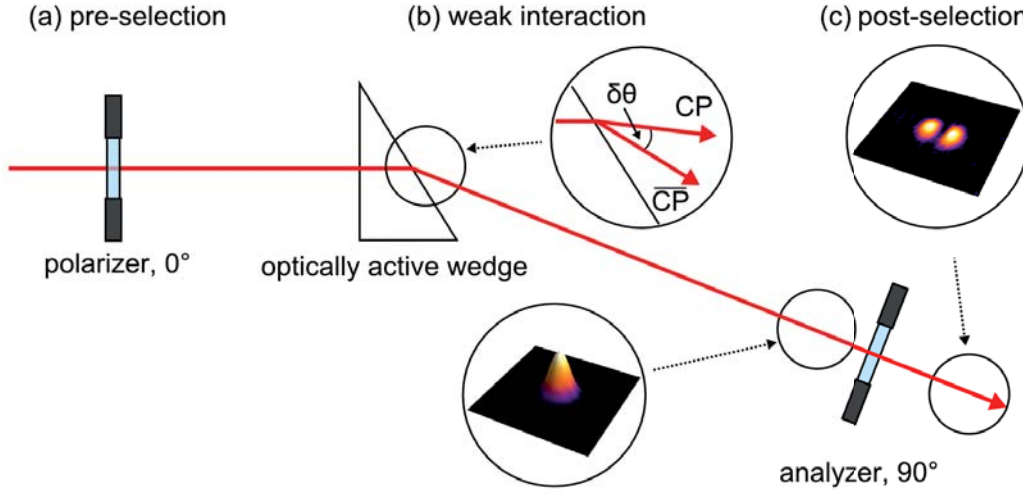


**Figure 3.6:** Usually weak measurement are based on three steps: (a) preparation of the system in a defined (polarization-) state (pre-selection), (b) weak interaction (perturbation) with the system giving here rise to different angles of refraction for two orthogonal circular polarization states ( $CP$ , and  $\overline{CP}$ ), and finally (c) post-selection of the final (polarization-) state. (taken from [P1])

compared to  $w$  ( $\sim \text{mm}$ ) is consistently small ( $\sim \mu\text{m}$ ), even after  $\sim \text{m}$ . As before we know that at a distance  $d$  after the interface the two Gaussian beam components are separated by  $2|\delta x(d)|$  (Eq. 3.5), thus:

$$\mathbf{E}_2(x,y,d) = \frac{1}{\sqrt{2}} \left[ \mathcal{E}_- e^{i\mathbf{k}_- \cdot \mathbf{r}} |\mathbf{L}\rangle + \mathcal{E}_+ e^{i\mathbf{k}_+ \cdot \mathbf{r}} |\mathbf{R}\rangle \right] \quad (3.21)$$

with

$$\mathcal{E}_\pm = \mathcal{E}(x \mp \delta x(d), y) \quad \text{and} \quad \mathbf{k}_\pm = \frac{2\pi n_0}{\lambda} [\pm \sin(\delta\theta/2) \hat{\mathbf{x}} + \cos(\delta\theta/2) \hat{\mathbf{z}}],$$

where  $n_0$  is the refractive index of the surrounding medium (here air). The vectors  $|\mathbf{L}\rangle$  and  $|\mathbf{R}\rangle$  are respectively the normalized Jones vectors for the left- and right-circularly polarized components. Because the angular beam shift is so *weak*, the circular polarization components spatially overlap except for the outermost wings of the Gaussian beam. It follows that the center of the resulting beam is still linearly polarized, and only the edges contain circular polarization components. Post-selection is achieved with an analyzer set to an angle  $\beta_{pol}$  placed after the interface and in front of the detector. If  $\beta_{pol}$  is orthogonal to the initial polarization the center is extinguished and only the circular components at the wings of the Gaussian pass the analyzer. A weak value amplification takes place as the beam separation dramatically increases from a few  $\sim \text{nm}$  or less to the width of the light beam, typically  $\sim \text{mm}$ . This amplification is maximal for an orthogonal post-selection state [33]. However, the nature of the measurement has changed, as now the intensity

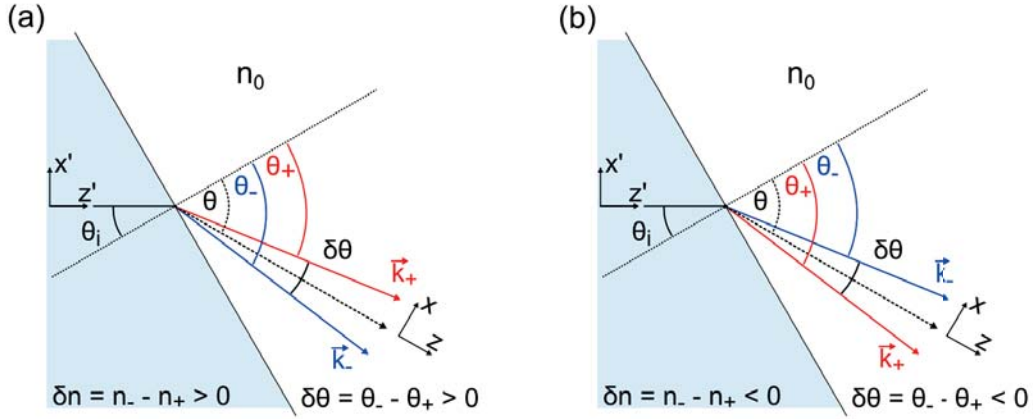


**Figure 3.7:** Refraction geometry at a chiral-achiral interface for a positive (a) and negative (b) circular birefringence  $\delta n$ . (taken from [P1])

becomes the measure of the weak interaction [32, 37]. The intensity after post-selection is directly proportional to the angular beam separation  $|\delta\theta|$ . The bigger  $|\delta\theta|$  the more intensity passes the analyzer. This can be seen from the field vector and the expression for the intensity after the analyzer:

$$\begin{aligned} \mathbf{E}_3(x, y, d) &= \frac{1}{2} \left[ \mathcal{E}_- e^{i(\mathbf{k}_- \cdot \mathbf{r} - \beta_{pol})} + \mathcal{E}_+ e^{i(\mathbf{k}_+ \cdot \mathbf{r} + \beta_{pol})} \right] (\cos \beta_{pol} |\mathbf{H}\rangle + \sin \beta_{pol} |\mathbf{V}\rangle) \\ I_3(x, y, d) &= \frac{1}{2} c_0 \epsilon_0 |\mathbf{E}_3|^2 = \frac{c_0 \epsilon_0}{8} \left[ \mathcal{E}_+^2 + \mathcal{E}_-^2 + 2 \mathcal{E}_+ \mathcal{E}_- \cos(\Delta \mathbf{k} \cdot \mathbf{r} + 2\beta_{pol}) \right] \end{aligned} \quad (3.22)$$

where  $c_0$  and  $\epsilon_0$  are the speed of light and the permittivity of the vacuum, respectively. The difference between the two wavevectors  $\mathbf{k}_\pm$  corresponding to the separated circularly polarized modes is given by:

$$\Delta \mathbf{k} = \mathbf{k}_+ - \mathbf{k}_- = 2k_0 \sin \left[ \frac{\delta\theta}{2} \right] \hat{\mathbf{x}} \quad (3.23)$$

Figure 3.8 shows plots of the intensities  $I_2(x, y, d)$  and  $I_3(x, y, d)$  calculated for two different beam displacements  $\delta x(d)$  and an orthogonal post-selection polarizer (i.e.  $\beta_{pol} = 90^\circ$ ).  $I_2$  is a single Gaussian (Fig. 3.8a and c), while  $I_3$  shows two peaks separated by a distance comparable to the beam diameter (Fig. 3.8b and d). Here, the peak intensity is proportional to the displacement of the beams. As can be seen from Fig. 3.8 and Eq. 3.22, the peak intensity after orthogonal post-selection is not sensitive to the sign of  $\delta x(d)$ , i.e. the left- and right-circular components can not be distinguished when  $\beta_{pol} = 90^\circ$ , as it is no longer clear which of the two polarization components deflects with  $\delta x(d)$  and which one deflects with  $-\delta x(d)$ . The sign information of the optical activity is therefore lost. It thus becomes necessary to combine weak value amplification with an appropriate modulation scheme

to retrieve the sign. This will be shown in the subsequent sections, where two different modulation schemes are presented and compared. In optical activity measurements the linear polarization state will necessarily rotate as it passes the optically active medium. Due to the necessary wedge geometry of the sample cell (Fig. 3.7), the light beam now traverses unequal distances through the optically active medium across the beam diameter. The optical rotation  $\alpha(x)$  also varies linearly across the beam diameter:

$$\alpha(x) = \alpha_0 + \kappa_\alpha \cdot x \quad (3.24)$$

Here  $\kappa_\alpha$  is a proportionality constant and  $\alpha_0$  is the rotation angle at the center of the beam. Now Eq. 3.22 has to be modified accordingly:

$$I'_3(x,y,z) = \frac{c_0 \epsilon_0}{8} \left\{ \mathcal{E}_+^2 + \mathcal{E}_-^2 + 2 \mathcal{E}_+ \mathcal{E}_- \cos \left[ 2 \left( k_0 \sin \left( \frac{\delta\theta}{2} \right) x + \beta_{pol} - \alpha(x) \right) \right] \right\} \quad (3.25)$$

Any polarization scheme that simply modulates the angle of the pre- or post-selection polarizers will adjust the amplification factor of the separation, but will also be sensitive to the optical rotation across the beam waist and will therefore primarily measure optical rotation (polarimetry) and not the angular deflection (beam separation). Therefore care must be taken when designing an appropriate modulation scheme, if these two phenomena are to be distinguished.

### 3.3.2 Heterodyne weak value amplified measurements

At first a heterodyne detection scheme is implemented to extract amplitude and the sign of the optical activity. The setup of Fig. 3.6 is now slightly modified (Fig. 3.9). A so called Zeeman HeNe laser is now used as a polarized light source, which emits two orthogonally circularly polarized modes with a frequency difference given by the Zeeman effect. This is realized by placing the laser cavity inside a strong longitudinal magnetic field, where the normal Zeeman effect leads to a splitting of the corresponding energy levels of the laser medium [38]. A quarter-waveplate converts the circular components into vertical and horizontal polarized Gaussian modes, polarized along  $y'$  and  $x'$  respectively. Again each mode is split into its circular polarization components at the chiral interface as described before (Sec. 3.1). A post-selecting analyzer is introduced for one of the two beams before the heterodyne beat signal is observed at the detector. As before the direction of the laser beam is taken to be along the  $z'$ -axis. Both modes have a 2D-Gaussian beam profile with the same amplitude  $\mathcal{E}(x',y')$  and beam size  $w$ . So Eq. 3.20 has to be slightly modified:

$$\mathbf{E}_4(x',y',t) = \mathcal{E}(x',y') \left[ e^{-i\omega_H t} |\mathbf{H}'\rangle + e^{-i\omega_V t} |\mathbf{V}'\rangle \right] e^{i\mathbf{k}_0 \cdot \mathbf{r}} \quad (3.26)$$

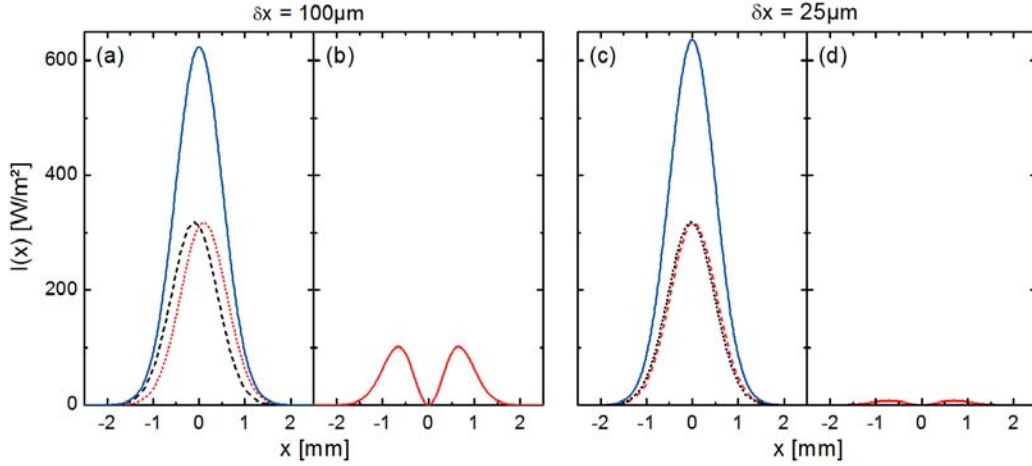


**Figure 3.8:** Calculated intensities for the sum (solid blue line) of two separated and orthogonally polarized Gaussians (dashed lines) before ((a) and (c)) and after post-selection (red line, (b) and (d)) for different beam displacements  $\delta x$ . The amplitude of the post-selected intensity is directly proportional to  $|\delta x|$  but not to the sign of  $\delta x$  [P1]

Here  $\omega_H$  and  $\omega_V$  are the angular frequencies of the horizontally and vertically polarized modes, respectively, and  $\mathbf{k}_0$  is the incident wavevector. The complex amplitudes for the horizontal and vertical polarized modes can be expressed in terms of the Jones vectors for left- and right-circular polarized light (Sec. 2.2.1).

$$\begin{aligned} |\mathbf{H}\rangle &= \frac{1}{\sqrt{2}} (|\mathbf{L}\rangle + |\mathbf{R}\rangle) \\ |\mathbf{V}\rangle &= \frac{1}{\sqrt{2}i} (|\mathbf{L}\rangle - |\mathbf{R}\rangle) = \frac{1}{\sqrt{2}}i (|\mathbf{R}\rangle - |\mathbf{L}\rangle) \end{aligned} \quad (3.27)$$

After refracting at the glass prism, the circular polarized field components of both modes are independently refracted and separated. The right-circularly polarized components of the two laser modes are deflected in the same direction, similarly the left-components. After the post-selection analyzer one obtains after a distance  $d$  behind the glass prism:

$$\begin{aligned} I_4(x, y, d, t) &= \frac{c_0 \epsilon_0}{8} \left[ (\mathcal{E}_+^2 + \mathcal{E}_-^2) + (\mathcal{E}_-^2 - \mathcal{E}_+^2) \sin \Delta\omega t + 2\mathcal{E}_+ \mathcal{E}_- \sin 2\Gamma(x) \cos \Delta\omega t \right] \\ \text{with } \Gamma(x) &= k_0 \sin \left( \frac{\delta\theta}{2} \right) x - \alpha(x) + \beta_{pol} \end{aligned} \quad (3.28)$$

The resulting intensity has contributions oscillating at the difference frequency  $\Delta\omega$  of the two laser modes. The first term is constant and not of interest. The second term oscillating at  $\sin \Delta\omega t$  is proportional to the difference of the two shifted Gaussian amplitudes  $\mathcal{E}_+$  and  $\mathcal{E}_-$  and so a measure of the splitting. The third one modulated with  $\cos \Delta\omega t$  depends on the product of  $\mathcal{E}_+$  and  $\mathcal{E}_-$  and also on the optical rotation  $\alpha(x)$  through  $\Gamma(x)$ . Assuming that a

position sensitive split detector is used for detection with  $I_4$  centered on the two halves  $A$  and  $B$  of the photodetector, then the measured time-dependent power modulated at  $\Delta\omega$  on each side of the detector can be calculated analog to Eqs. 3.16. By inserting Eq. 3.28 in Eq. 3.16 the integrals can be calculated and we obtain for the difference  $\Delta P = P_B - P_A$  of the signals:

$$\Delta P_{\Delta\omega}(t) = \frac{P_0}{2} \left\{ \operatorname{erf} \left[ \frac{\sqrt{2}\delta x}{w} \right] \sin \Delta\omega t + \cos(2b) \operatorname{erfi} \left[ \frac{aw}{\sqrt{2}} \right] \exp \left[ -\frac{2\delta x^2}{w^2} - \frac{a^2 w^2}{2} \right] \cos \Delta\omega t \right\}$$

$$\text{with } a = k_0 \sin \left( \frac{\delta\theta}{2} \right) - \kappa_\alpha \quad \text{and} \quad b = (\beta_{pol} - \alpha_0) \quad (3.29)$$

where  $P_0 = 0.25\pi\epsilon_0 c_0 \mathcal{E}_0^2 w^2$  is the power of the laser, and  $\operatorname{erf}(x) = (2/\sqrt{\pi}) \int_0^x e^{-t^2} dt$  and  $\operatorname{erfi}(x) = -i \operatorname{erf}(i x)$  are the real and complex error functions, respectively. As expected, the amplitude of the first term is proportional to the magnitude and sign of the lateral displacement  $\delta x$ , i.e. the optical activity  $\delta n$ . It can be separated from the second term due to the phase shift using lock-in detection.

### Experimental setup

The setup used for the heterodyne weak measurements is shown in Fig. 3.9. A HP 5517B Zeeman-HeNe-laser was taken as a light source, which emits both orthogonal linear polarized modes with an frequency difference of  $\Delta\omega = 2.5$  MHz and a center wavelength of  $\lambda = 633$  nm. The light passes through the 30°-sample prism (SF11-glass) inside the homogeneous longitudinal magnetic-field. The post-selection is done by a Glan-Thompson-

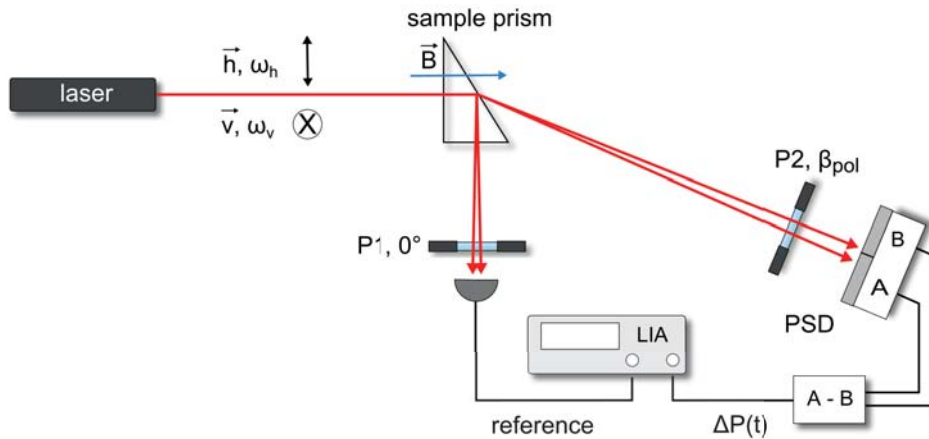


**Figure 3.9:** Experimental setup used for the heterodyne weak value amplified measurements. See text for details. (adapted from [P2])

polarizer before the position sensitive detector (PSD, UDT SPOT-9DMI). The latter is placed 0.6 m after the prism. Once again the generated left and right-side signals are electronically subtracted and sent to a lock-in amplifier (Stanford Research Systems SR844) locked to the difference frequency  $\Delta\omega$ .

The in-phase ( $X(B)$ ) and the out-of-phase component ( $Y(B)$ ) of the LIA represent the amplitudes of the signals oscillating with  $\cos \Delta\omega t$  and  $\sin \Delta\omega t$ , respectively. At the beginning of each measurement the beam was centered on the PSD. The lateral displacement  $\delta x$  can now be measured based on the lock-in amplitude  $Y(B)$  of the out-of-phase component:

$$\delta x = \frac{w}{\sqrt{2}} \operatorname{erf}^{-1} \left[ \frac{2\Delta P}{P_0} \right] = \frac{w}{\sqrt{2}} \operatorname{erf}^{-1} \left[ \frac{2\sqrt{2} Y(B)}{g_{trans} \rho_{sens} P_0} \right] \quad (3.30)$$

Here  $g_{trans} = 1 \cdot 10^4$  V/A is the gain of the transimpedance amplifier and  $\rho_{sens} = 0.48$  A/W the sensitivity of the detector element.

## Measurements

The magnetic field was tuned between 250 and 550 Gauss with a step size of 30 Gauss and the corresponding in-phase and out-of-phase lock-in amplitudes were measured. Figure 3.10 shows the results for three measurements where each is an average over five consecutively

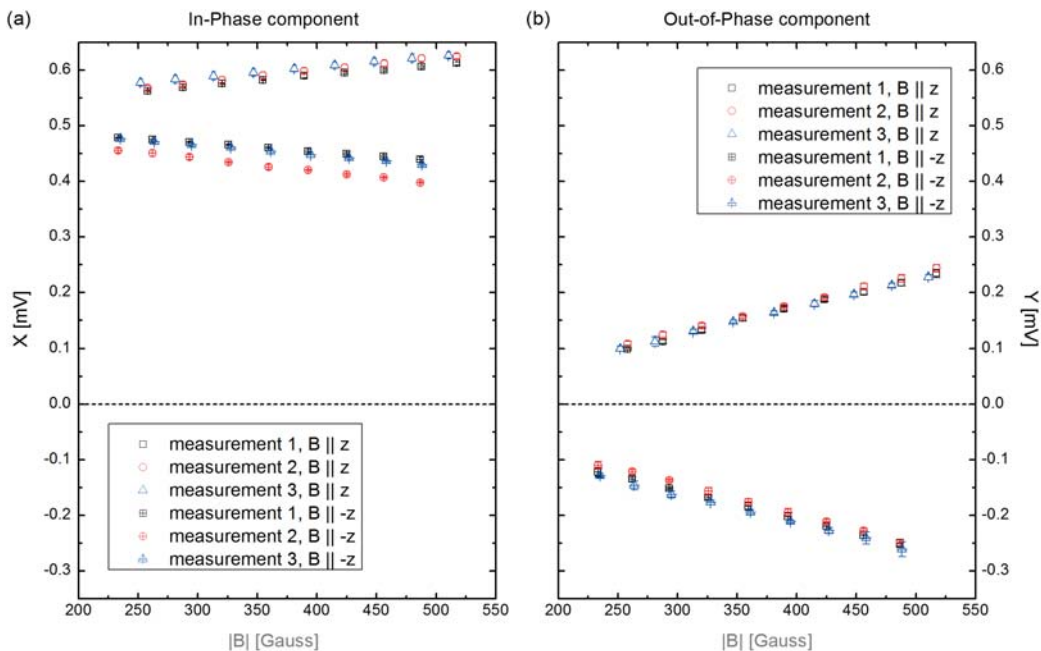


**Figure 3.10:** Measurement results using heterodyne weak value detection. Shown are both, (a) the in-phase and (b) out-of-phase component, where only the latter changes sign as the polarity of the magnetic field does.

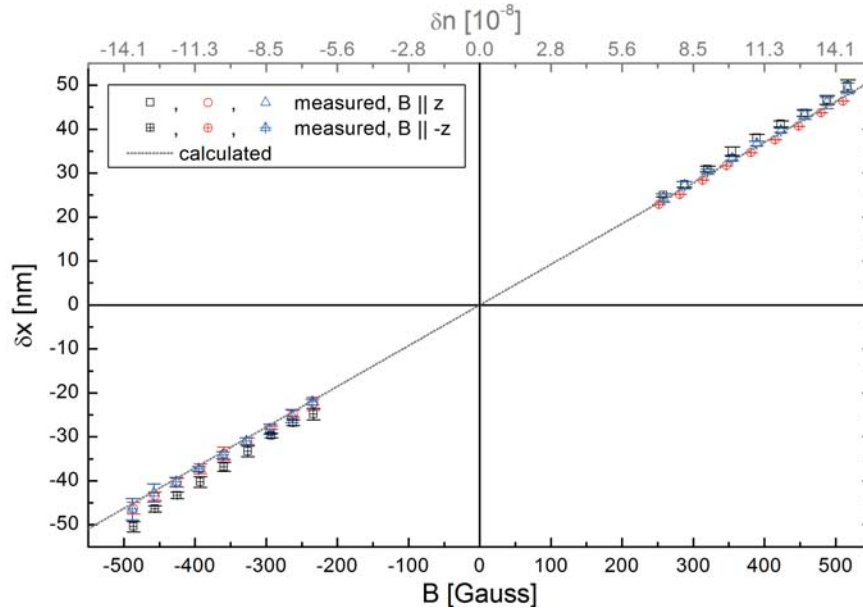


**Figure 3.11:** Comparison of the displacement values  $\delta x$  calculated from  $Y(B)$  using Eq. 3.30 and the theoretically predicted ones (Eq. 3.5). Both are in good agreement with each other.

taken data sets. Differences in the magnetic field strength of  $\Delta B = 30$  Gauss are well resolved both in  $X(B)$  and  $Y(B)$  which correspond to a difference in the circular birefringence of  $\delta n = 10^{-8}$  and an angular beam deflection of  $\delta\theta = 4.5$  nrad. Now the polarity of the B-field was changed and again three measurements were performed where both  $X(B)$  and  $Y(B)$  were recorded. As expected only the out-of-phase signal  $Y(B)$  changes sign with a reversal of the B-field polarity and is therefore sensitive to the handedness of the optical activity. Furthermore, the three measurements of each diagram show the same response of the system to linear changes of the magnetic field, which is reflected in the slopes of the three data sets. Therefore, Eq. 3.30 was used to calculate the displacement  $\delta x$  from the measured  $Y(B)$  values. The results are shown in Fig. 3.11, where they are compared with the values predicted from theory (Eq. 3.5). All measured values are in good agreement with the theoretical ones. All data sets have been recorded with no active temperature or position stabilization of the prism and the PSD, respectively.

Using the Zeeman-HeNe-laser in the heterodyne detection setup has slightly improved the sensitivity compared to the method shown before. However, the setup requires specialized equipment. In the following section an even more sensitive measurement scheme is introduced using a conventional HeNe laser.

### 3.3.3 Polarization modulated weak value amplified measurements

We now tested a combination of a weak value amplified measurement with an appropriate polarization modulation and therefor adapted the setup in Fig. 3.6. The post-selection analyzer is kept nearly orthogonal (within experimental error) and a Faraday-rotator (FR) and a quarter-wave plate (QWP) are introduced after the pre-selection polarizer as shown in Fig. 3.13. As before, the light is first polarized along  $x'$  (Eq. 3.20), but then passes the FR in combination with the QWP. The FR rotates the plane of polarization by a small angle  $\beta_{FR}$ , but since the quarter-waveplate is oriented with its fast-axis parallel to the pre-selection polarizer, the beam now contains a circular polarization component and becomes elliptical:

$$\mathbf{E}_5 = \frac{\mathcal{E}}{\sqrt{2}} e^{ik_0 \cdot \mathbf{r}} [(\cos \beta_{FR} - \sin \beta_{FR}) |\mathbf{L}\rangle + (\cos \beta_{FR} + \sin \beta_{FR}) |\mathbf{R}\rangle] \quad (3.31)$$

where the explicit  $x$  and  $y$  dependence has been suppressed for clarity. Again at the exiting surface of the optically active wedge the circular polarization components are split, and after passing the post-selecting analyzer, set at  $\beta_{pol}$ , the resultant intensity distribution at the detector becomes

$$I_5 = \frac{c_0 \epsilon_0}{8} [(\mathcal{E}_+^2 + \mathcal{E}_-^2) + (\mathcal{E}_+^2 - \mathcal{E}_-^2) \sin 2\beta_{FR} + 2\mathcal{E}_+ \mathcal{E}_- \cos 2\Gamma(x) \cos 2\beta_{FR}] \quad (3.32)$$

This expression is very similar to the one we derived for the heterodyne weak value amplified measurements in Sec. 3.3.2. A position sensitive split detector is used and the resulting power on each side of the detector can also be calculated using equations 3.16. The difference of the two signals is

$$\Delta P_{FR} = \frac{P_0}{2} \left\{ \operatorname{erf} \left[ \frac{\sqrt{2}\delta x}{w} \right] \sin 2\beta_{FR} - \sin(2b) \operatorname{erfi} \left[ \frac{aw}{\sqrt{2}} \right] \exp \left[ -\frac{2\delta x^2}{w^2} - \frac{a^2 w^2}{2} \right] \cos 2\beta_{FR} \right\}$$

$$\text{with } a = k_0 \sin \left( \frac{\delta\theta}{2} \right) - \kappa_\alpha \quad \text{and} \quad b = (\beta_{pol} - \alpha_0) \quad (3.33)$$

If the Faraday-rotator is now modulated at  $\omega_{FR}$  so that  $\beta_{FR}(t) = \Delta\beta \sin \omega_{FR} t$ , the intensity  $I_5(x, y, d, t)$  as well as the power difference  $\Delta P_{FR}(t)$  become time-dependent, which is illustrated in Fig. 3.12. Analog to equations 3.11 we can write:

$$\begin{aligned} \sin [2\Delta\beta \sin \omega_{FR} t] &= 2J_1(2\Delta\beta) \sin \omega_{FR} t + \dots \\ \cos [2\Delta\beta \sin \omega_{FR} t] &= J_0(2\Delta\beta) + 2J_2(2\Delta\beta) \cos 2\omega_{FR} t + \dots \end{aligned} \quad (3.34)$$

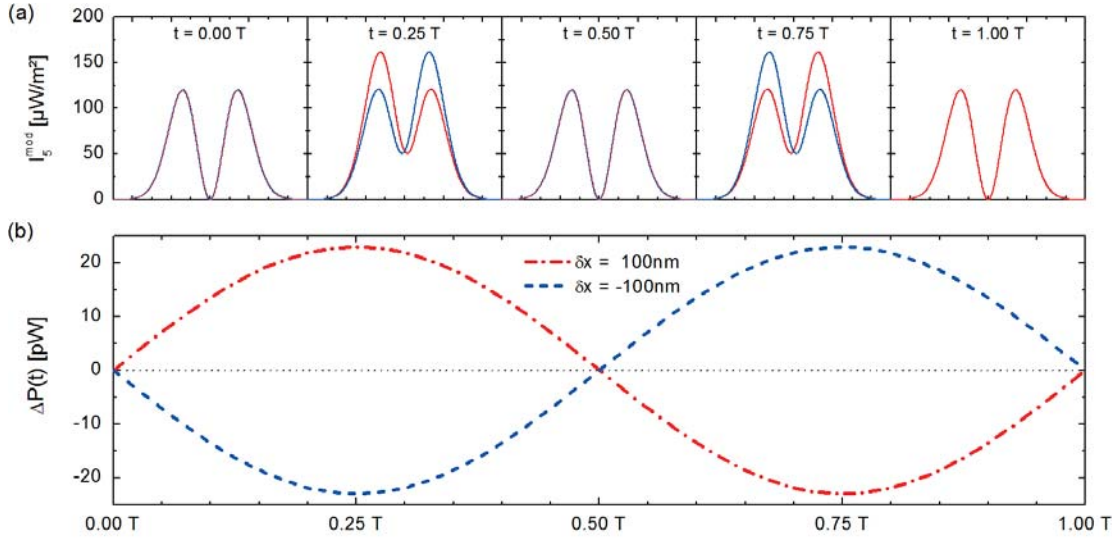


**Figure 3.12:** (a) Intensity  $I_5(x,y,z,t)$  at  $y = 0$  for beam displacements  $\delta x = \pm 100 \text{ nm}$  calculated for different fractions of the period  $T$ . (b) Resulting  $\sin \omega_{FR} t$  term of the time-dependent power difference  $\Delta P(t)$  calculated with Eq. 3.33 for  $\delta x = \pm 100 \text{ nm}$ . Both signals have the same amplitude but are phase-shifted by  $\pi$ . (taken from [P1])

Here  $J_0$ ,  $J_1$ , and  $J_2$  are the Bessel functions of the zeroth, first, and second order, respectively. As can be seen from Eq. 3.33 the first term now oscillates at the fundamental,  $\omega_{FR}$ , and is directly proportional to the splitting  $\delta x$ . The second term splits into two, a constant and one modulated at the harmonic  $2\omega_{FR}$ . Lock-in detection allows the discrimination of the first term from the others influenced by the optical rotation  $\alpha(x)$ . Figure 3.12b demonstrates, that the amplitude of the first term is proportional to  $|\delta\theta|$  and the sign of the signal is proportional to  $\text{sgn}(\delta\theta)$ . If the magnetic field  $B$  is switched off, the lateral displacement  $\delta x$  and optical rotation  $\alpha(x)$  will vanish and Eq. 3.32 simplifies to

$$I'_5 = \frac{c_0 \epsilon_0}{4} A_0^2 [1 + \cos 2\beta_{pol} \cos 2\beta_{FR}], \quad (3.35)$$

The sum of the power signals  $\Sigma P = P_A + P_B$  generated at the detector can again be calculated using equations 3.16:

$$\Sigma P(t) = \frac{P_0}{2} [1 + \cos 2\beta_{pol} (J_0(2\Delta\beta) + 2J_2(2\Delta\beta) \cos 2\omega_{FR} t)] \quad (3.36)$$

Now just the term oscillating at the second harmonic of  $\omega_{FR}$  is detected with the lock-in amplifier. The rotation angle  $\Delta\beta$  of the rotator is directly proportional to the applied voltage  $U_{FR}$ , so the resulting amplitude  $R_{LIA,2f}$  is:

$$R_{LIA,2f} = U_0 J_2(2\Delta\beta) \cos 2\beta_{pol} = U_0 J_2(2 c U_{FR}) \cos 2\beta_{pol} \quad (3.37)$$

This equation can now be used for the calibration of the Faraday rotator.

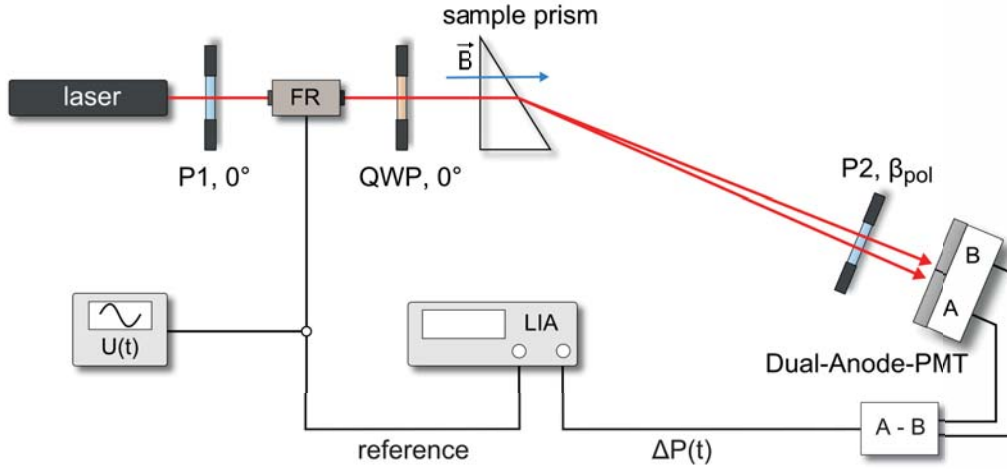


**Figure 3.13:** Setup used for polarization modulated weak measurements, involving a HeNe-laser, two Glan-Thompson-polarizers (P1 and P2), a Faraday-Rotator (FR), a quarterwave-plate (QWP), a glass prism, and a dual-anode photomultiplier tube (PMT). A lock-in amplifier (LIA) was used to detect the time varying difference signal  $\Delta P$  [P1].

### Experimental setup

For all the subsequent measurements the setup is as shown in Fig. 3.13, where a position-sensitive dual anode-photomultiplier tube (Hamamatsu R5900U-04-M4) is used as a detector and placed at a fixed distance behind the sample prism. A Helium-Neon laser with  $\lambda = 633$  nm and an output power of  $P_0 \sim 7$  mW is taken as a light source. The amplitude and the phase of  $\Delta P(t)$  are measured with a lock-in amplifier (Stanford Research Systems SR830). The lateral displacement  $\delta x$  can be calculated from the detected lock-in amplitude  $R_{LIA}$ :

$$\delta x = \frac{w}{\sqrt{2}} \operatorname{erf}^{-1} \left[ \frac{\Delta P}{J_1(2\Delta\beta)P_0} \right] = \frac{w}{\sqrt{2}} \operatorname{erf}^{-1} \left[ \frac{\sqrt{2}R_{LIA}}{g_P J_1(2\Delta\beta)P_0} \right] \quad (3.38)$$

The gain factor  $g_P$  converts between the generated power signal  $\Delta P$  and the measured lock-in amplitude  $R_{LIA}$  and has been determined experimentally to  $g_P = 2.8 \cdot 10^9$  V/W for an anode voltage of  $U_{anode} = 500$  V of the PMT <sup>1</sup>.

The Faraday rotator consists of a 5 mm thick BK7 glass plate centered in a Helmholtz coil. The output of the reference channel of the LIA was used as voltage source, so that the coil was modulated at 187 Hz with an amplitude  $U_{FR} = 3$  V (i.e.  $\sim 100$  Gauss). This causes the plane of polarization of the light incident on the QWP to be rotated by  $\pm 5$  millidegree, which can be seen from the calibration curve shown in Fig. 3.14. Here the output voltage

<sup>1</sup> Comparison between  $R_{LIA}$  and optical power measured with a power meter (HP8152 A) for different anode voltages of the PMT.

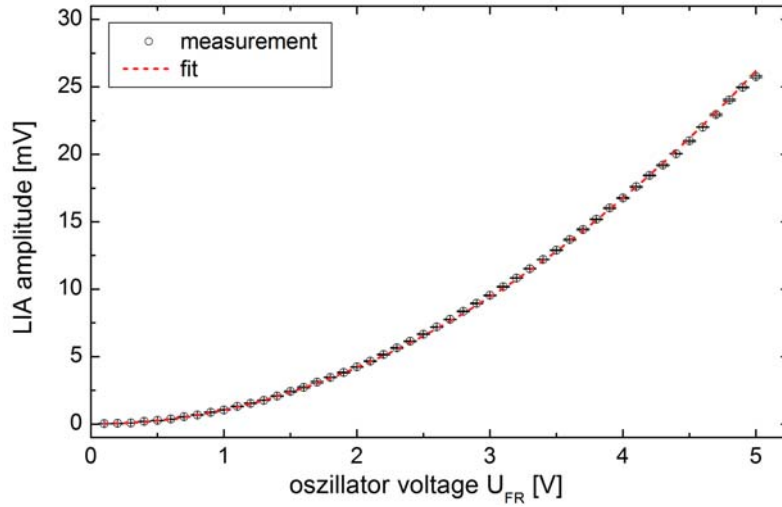


**Figure 3.14:** Calibration curve for the Faraday rotator. The LIA amplitude  $R_{2f}$  was detected while increasing the applied voltage  $U_{FR}$ . A fit with Eq. 3.37 yields the proportionality constant  $c$  to 1.65 millidegree/V.

$U_{FR}$  was increased while the LIA amplitude for the sum signal  $\Sigma P$  was recorded. Finally, a fit with Eq 3.37 to the measured data yielded  $c = 1.65$  millidegree/V.

## Measurements

First the optical activity was varied by changing the longitudinal magnetic field  $B$  across the glass prism between 100 and 400 Gauss, whilst detecting  $\Delta P(t)$ . Figure 3.15 shows the results for two measurements with the analyzer placed respectively at  $d = 0.65$  m and  $d = 1.2$  m after the prism. Each data point corresponds to an average over 100 measurements taken in 200 ms time intervals. It can be seen that as the distance between the interface and the post-selection polarizer increases, so does the intensity after the post-selection analyzer, in accordance with theory (dashed lines in Fig. 3.15). This is expected, as  $\Delta P$  is proportional to  $\delta x(d) = d \tan(\delta\theta/2)$  (see Eq. 3.33), and therefore scales linearly with distance. The distance  $d$  increases 1.846 fold in Fig. 3.15 and this is in good agreement with the experimentally observed increase in the slope of  $1.87 \pm 0.08$ . This clearly demonstrates that the setup is sensitive to the angular divergence  $\delta\theta$ , as opposed to a lateral beam shift or some effect due to optical rotation.

To demonstrate that the measurements can be used to determine the absolute sign of the optical activity, the post-selection polarizer P2 was placed a distance  $d = 1.2$  m after the prism. While changing the magnetic field in 10 Gauss steps  $\Delta P(t)$  was measured for opposite signs of the longitudinal magnetic field (optical activity). The results are depicted in Fig. 3.16a. As before each data point is an average of 100 measurements taken in 200 ms

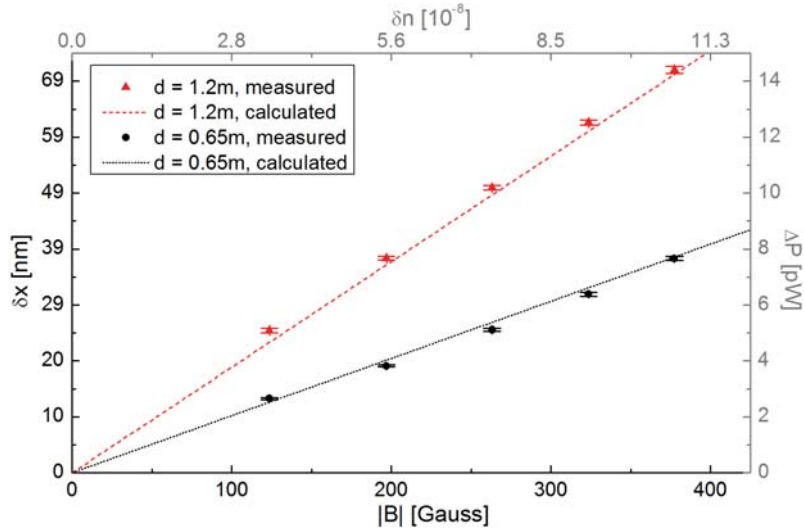


**Figure 3.15:** Measurements of  $\Delta P$  for two different distances  $d$  between the prism surface and the post-selection analyzer P2 together with the theoretically predicted power differences (Eq. 3.32, dashed lines). (adapted from [P1])

time intervals. Both data sets match the theoretically predicted lines for  $\Delta P(t)$  (Eq. 3.33). It follows that the sign (i.e. the direction) of the angular splitting, and hence the handedness are faithfully recovered in this weak value amplification scheme. Figure 3.16b depicts a zoom of a region of Fig. 3.16a delineated by the box. It can be seen, that the data points are well separated, even though the magnetic field was only increased in 10 Gauss steps. This corresponds to a change in the circular birefringence of  $\delta n = 3 \times 10^{-9}$  or to a change of  $\delta\theta = 3$  nrad in the relative angle of refraction. It could be resolved with a relative error of  $s_{rel} \leq 1\%$ .

### 3.4 Comparison of methods

The measured values for the spatial separation  $\delta x$  have been used to calculate the corresponding circular birefringence  $\delta n$  for the different detection schemes. This has been done by combining Eq. 3.4 and 3.5 to

$$\delta n = 2n_0 \frac{\cos \theta}{\sin \theta_0} \arctan \left[ \frac{\delta x}{d} \right] \quad (3.39)$$

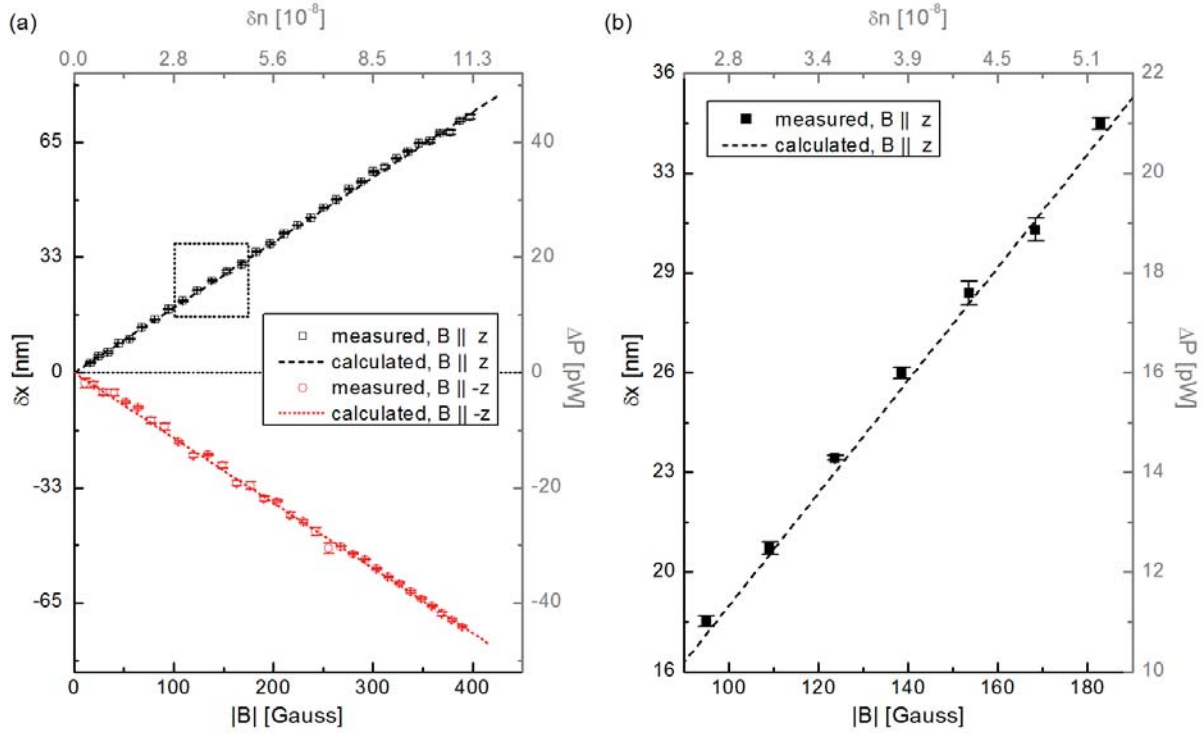


**Figure 3.16:** (a) Measurement of  $\Delta P$  for  $d = 1.2$  m with  $\mathbf{B} \parallel \hat{z}$  (black) and  $\mathbf{B} \parallel -\hat{z}$  (red). Both have the same magnitude but opposite sign and are in good agreement with theoretical predictions according Eq. 3.33 (dashed lines). (b) Zoom of the data in (a) marked by the box. The step size of  $\Delta B = 10$  Gauss corresponding to  $\delta n = 3 \times 10^{-9}$  and  $\delta \theta = 3$  mrad is well resolved. In both diagrams  $\delta x$  corresponds to the separation before the post-selection analyzer calculated from  $\Delta P$  (Eq. 3.38). (taken from [P1])

The angle of incidence at the chiral/achiral surface of the SF11-prism was  $\theta_0 = 30^\circ$  and the mean refraction angle  $\theta = 62.792^\circ$ . The results are shown in Fig. 3.17 together with the theoretical values  $\delta n_{theo} = VB\lambda/\pi$  computed from Eq. 3.6 (first row). The measurements are in good agreement with the theory for all three detection schemes. This is illustrated by the deviation values  $\Delta = \delta n - \delta n_{theo}$  also shown in Fig. 3.17 (second row). The error bars are the errors of the corresponding measurement values, i.e. the standard deviation. For all detection schemes the deviation  $\Delta$  is less than  $1 \times 10^{-8}$ , where for the polarization modulated weak value amplification (PMWVA) it is less than  $1 \times 10^{-9}$ .

The third row of Fig. 3.17 shows the relative error  $s_{rel}$  for each data point. The smallest values have been achieved with the PMWVA method, so here  $s_{rel} \leq 2\%$  for most of the measured values. Nevertheless, errors below 5% could be realized for the other methods, except for the dual polarization modulation (DPM) with  $d = 0.6$  m. The solid horizontal lines in the diagrams represent the mean relative error values. The RMS deviations  $\bar{\Delta}$  and mean relative errors have in detail been determined to:

$$\text{dual polarization modulation, 0.6 m: } \quad \bar{\Delta} = 3.1 \times 10^{-9}, \quad s_{rel} = 3.6\%$$

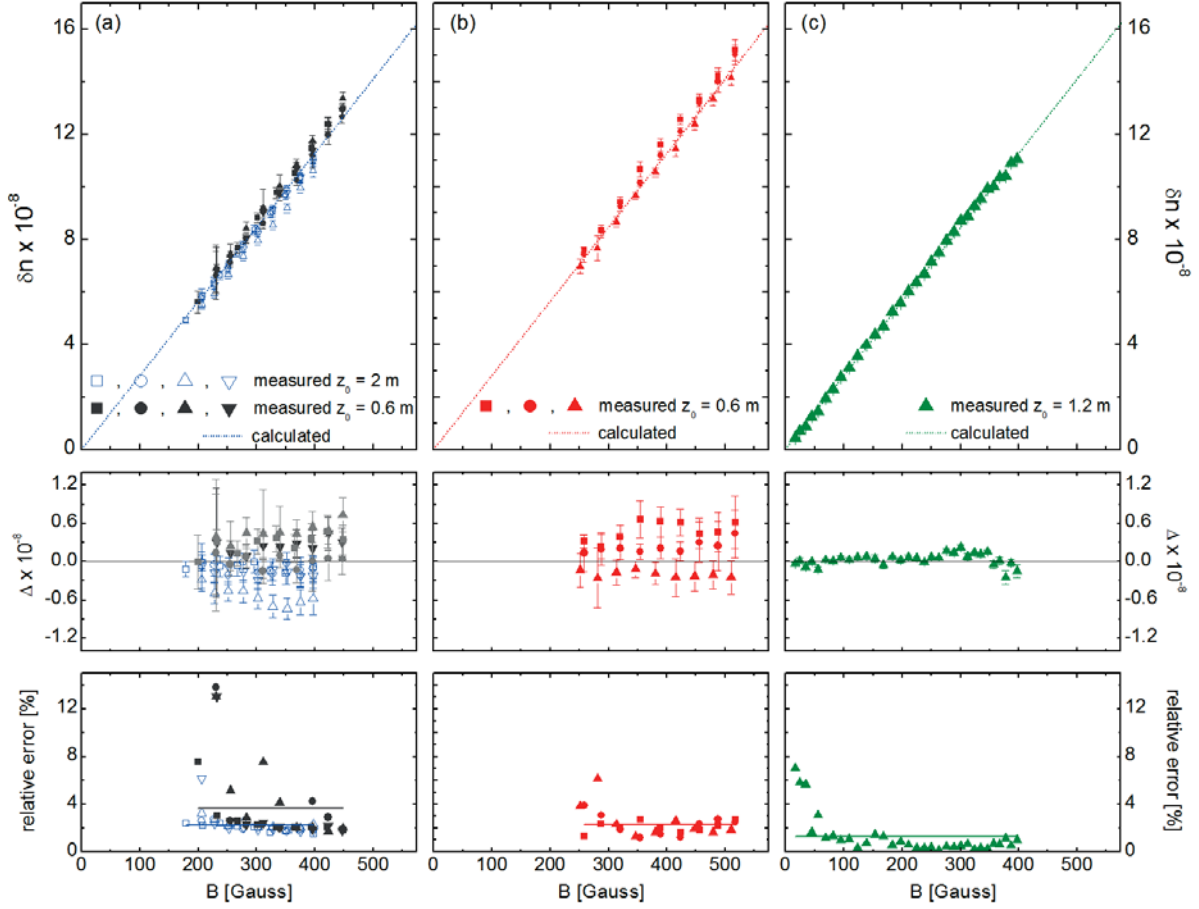


**Figure 3.17:** Comparison of the (a) dual-polarization-modulation, (b) heterodyne weak value amplification and (c) polarization modulated weak value amplification detection. Shown are the measured values for  $\delta n$  derived from Eq. 3.39 together with the theoretical ones  $\delta n_{theo}$  (first row), the deviation  $\Delta = \delta n - \delta n_{theo}$  (second row), as well as the relative error.

dual polarization modulation, 2.0 m:	$\bar{\Delta} = 2.5 \times 10^{-9}, s_{rel} = 2.2\%$
heterodyne weak value amplification:	$\bar{\Delta} = 3.2 \times 10^{-9}, s_{rel} = 2.3\%$
pol. modulated weak value amplification:	$\bar{\Delta} = 0.9 \times 10^{-9}, s_{rel} = 1.3\%$

Therefore the PMWVA method seems to be the most sensitive one for the detection of the optical activity induced spatial displacement  $\delta x$  and so for the circular birefringence  $\delta n$  in small sample volumes. The steps of  $\delta n = 3 \times 10^{-9}$  are well resolved with a mean relative error of  $\sim 1\%$  and a RMS deviation of  $\sim 1 \times 10^{-9}$ . Therefore, a sensitivity of  $\delta n_s \leq 1 \times 10^{-9}$  is assumed for this setup. This sensitivity corresponds to an optical rotation measured in a polarimeter that uses a 10 cm sample cell of about

$$\alpha_1 = \frac{\pi l}{\lambda} \delta n_s = 0.03^\circ$$

Here  $l = 10$  cm is the pathlength and  $\lambda = 633$  nm the wavelength. Such a polarimeter sample cell requires volumes of at least  $800 \mu\text{l}$ , assuming a rectangular cell with a dimension of  $2 \times 4 \times 100 \text{ mm}^3$  and a laser beam cross section of less than 2 mm. In contrast, the refraction method requires a volume of less than  $8 \mu\text{l}$  for a wedge shaped sample cell with a size of  $2 \times 4 \times 2 \text{ mm}^3$ . Using a cell of the same length in a polarimeter the 50-fold shorter pathlength of  $l_2 = 2$  mm would lead to a reduced optical rotation of

$$\alpha_2 = \frac{\pi l_2}{\lambda} \delta n_s = 0.0006^\circ$$

This is comparable to the sensitivity  $\delta\alpha$  of a commercial polarimeter, which is usually in the order of  $\delta\alpha \sim 0.001^\circ$ . Therefore, the detection of circular birefringence of  $\delta n < 1 \times 10^{-9}$  is difficult for traditionally polarimetry when using such small sample volumes but could be resolved with the presented refraction method.



# 4

## MIR Laser-Based Vibrational Optical Activity

The measurement of the difference in left- and right-circularly polarized absorption (circular dichroism) is the basis for determining the absolute configuration of a chiral molecule in solution [5]. Detection of circular dichroism in the visible and ultraviolet (ECD) has proven its use in the analysis of protein secondary structure, but generally offers only one or two broad difference bands for stereochemical analysis. Vibrational optical activity (VOA) in the mid infrared (MIR), in contrast, provides a characteristic band pattern with contributions of up to  $3N - 6$  vibrational modes all being active [39–41] where  $N$  is the number of the atoms. Vibrational circular dichroism (VCD) spectroscopy has become one of the key methods for the determination of the absolute configuration of pharmaceutically active chiral compounds and natural products [40–42]. Since VOA spectroscopy is also sensitive towards the conformation of molecules, a VOA spectrum can be interpreted as a linear combination of the spectral contributions of all conformers that are populated for the given experimental condition. Therefore, VOA and in particular VCD are not only tools for conformational analysis of small molecules [42, 43], but also a sensitive probe for secondary structure in biomolecules [44]. One difficulty in VCD spectroscopy, however, is the strong absorption of most solvents in the (M)IR. Traditional VCD instrumentation therefore limits the study of (bio)molecules to selected spectral regions and solvents.

Here, it is demonstrated that quantum cascade lasers (QCLs) are an attractive and powerful light source for VOA spectroscopy. QCLs were first demonstrated in 1994 by Faist et al. [45] and opened up new possibilities in mid-infrared (MIR) vibrational spectroscopy [46, 47]. They represent the only practical laser source available in the MIR as they are technically less demanding than nonlinear optical schemes based on frequency conversion. The latter have recently been applied to measurements of VOA [48, 49]. The spectral brightness of a QCL ( $> 10^4$ ) compared with conventional FT-light sources should allow measurements

even in strongly absorbing solvents. The measurement of the optical rotation (vibrational circular birefringence VCB) in the MIR based on the difference of the real part of the refractive index is a complementary technique [50]. It can also be used for optical activity analysis.

Therefore, VCD and VCB spectra recorded with a cw tunable mid-infrared laser are presented. The QCL measurements are compared to traditional FTIR based measurements and calculations. It is shown that QCLs are useful for both vibrational spectroscopies especially regarding aqueous solutions. This chapter has been in part published in [P3,P4]. The work was a collaboration with Dr. Steffen Lüdeke and Anja Rütter from the Institute of Pharmaceutical Sciences of the University Freiburg (Germany), who also contributed DFT calculations, FT-VCD and FTIR reference measurements, and the assignment of vibrational modes presented in this section.

## 4.1 Theory

In chapter 2 we have seen, that optical activity observed in an isotropic chiral medium manifests itself via the differential response to left- and right-circularly polarized light, which is a function of the difference in the complex refractive indices for both polarizations (Eq. 2.34). The circular birefringence (CB)  $\delta n = n_l - n_r$ , measured in the previous chapter with a chiral refractometer, is also detectable in the MIR. The differential absorption of left- and right-circularly polarized light caused by the difference in the imaginary part  $\delta\kappa = \kappa_l - \kappa_r$  gives rise to circular dichroism (CD). Analogous to the complex refractive index  $\tilde{n}$  the absorbance  $A$  and the molecular absorptivity  $\epsilon$  of the material can be defined as complex functions, too [50]:

$$\tilde{A} = A'_{L,R} + i \cdot A''_{L,R} \quad \text{and} \quad \tilde{\epsilon} = \epsilon'_{L,R} + i \cdot \epsilon''_{L,R} \quad (4.1)$$

VCD and VCB can therefore be translated to a difference in the real and imaginary part of the complex absorbance  $\Delta\tilde{A}$  or molecular absorptivity  $\Delta\tilde{\epsilon}$  (see Eq. 2.40) [12]:

$$\text{VCB:} \quad \Delta A' = \frac{4\pi\nu z_0}{\ln(10)} \delta n \quad \text{and} \quad \Delta \epsilon' = \frac{4\pi\nu}{\ln(10) \cdot C} \delta n \quad (4.2a)$$

$$\text{VCD:} \quad \Delta A'' = \frac{4\pi\nu z_0}{\ln(10)} \delta \kappa \quad \text{and} \quad \Delta \epsilon'' = \frac{4\pi\nu}{\ln(10) \cdot C} \delta \kappa \quad (4.2b)$$

Here  $z_0$  and  $C$  are the path length and the concentration of the sample, respectively, and  $\nu = 1/\lambda$  is the frequency in wavenumbers. Since both,  $\Delta A'$  and  $\Delta A''$ , scale linearly with the path length  $z_0$ , they benefit from powerful light sources, that can propagate through long path-lengths (and strongly absorbing samples). So both spectroscopies can therefore potentially benefit from QCLs.

### 4.1.1 Measurement of vibrational circular dichroism, VCD

Typically the setup used for VCD measurements consist of a light source (LS), a linear polarizer (LP), a photoelastic modulator (PEM), the sample (S) and a detector (D). Schematically we can write [12]:

$$\boxed{LS} \rightarrow \boxed{LP} \rightarrow \boxed{PEM} \rightarrow \boxed{S} \rightarrow \boxed{D}$$

Here the light source is a quantum cascade laser emitting linearly polarized light ( $\vec{V}$ ). The light from the laser is sent trough a ZnSe PEM, which modulates the light at the frequency  $\omega_{PEM} = 2\pi f_{PEM}$  between left- and right-circularly polarization states. Using a Mueller-Matrix formalism the intensity  $I_1(t)$  at the detector can be calculated [12]. The resulting Stokes vector  $\vec{S}_f$  is:

$$\vec{S}_f = [D] [S] [PEM_{45^\circ}] \vec{V} \quad (4.3)$$

The PEM is modeled as a retarder with a time-varying retardation and its principal axis is oriented with  $\theta_{PEM} = 45^\circ$  (Tab. 2.3). The general Müller matrix of the optically active sample is given by [12]:

$$[S] = 10^{-A''} \begin{bmatrix} 1 & 0 & 0 & CD \\ 0 & 1 & CB & 0 \\ 0 & -CB & 1 & 0 \\ CD & 0 & 0 & 1 \end{bmatrix} \quad (4.4)$$

$CD = \ln 10 \Delta A''/2$  and  $CB = \ln 10 \Delta A'/2$  represent the intensity changes induced by the sample's circular dichroism and circular birefringence [12].  $A''$  is the decadic absorbance. The detector is assumed to have no birefringence and measures the intensity, so it is represented simply by a  $4 \times 1$  matrix:

$$[D] = \begin{bmatrix} 1 \\ 0 \\ 0 \\ 0 \end{bmatrix} \quad (4.5)$$

Using Eqs. 3.10 and 3.11 for the time-varying retardation of the PEM we finally can write for the intensity  $I_1(t)$  at the detector [12, 50, 51]:

$$\begin{aligned} I_1(t) &= I_0 10^{-A''} [1 - J_1(\delta_0) \ln(10) \Delta A'' \sin(\omega_{PEM} t)] \\ &= I_{DC} - I_{AC} \sin(\omega_{PEM} t) \end{aligned} \quad (4.6)$$

$J_1$  is the Bessel function of the first order and  $\delta_0 \approx \pi/2$  the phase retardation introduced by the PEM. The difference in the absorbance  $\Delta A''$  for the two circular polarizations leads to

an intensity modulated at the frequency of the PEM. The amplitude  $I_{AC}$  of the modulated term is detected using a lock-in amplifier (LIA). The VCD spectrum  $\Delta A''$  or  $\delta k$  can be derived from Eq. 4.6:

$$\Delta A'' = \frac{1}{\ln(10) \cdot J_1(\delta_0)} I_{AC}/I_{DC} \quad \delta k = \frac{1}{4\pi\nu z_0 \cdot J_1(\delta_0)} I_{AC}/I_{DC} \quad (4.7)$$

#### 4.1.2 Measurement of vibrational circular birefringence, VCB

For the measurement of VCB spectra we now insert an additional linear polarizer after the sample set at  $45^\circ$  with respect to the input polarization and parallel to the optical axis of the PEM [12]:

$$\boxed{LS} \rightarrow \boxed{LP} \rightarrow \boxed{PEM} \rightarrow \boxed{S} \rightarrow \boxed{LP} \rightarrow \boxed{D}$$

Again the polarization is modulated by the PEM from vertical to circular and back at a frequency of  $2\omega_{PEM}$ . Without a sample the same intensity can pass the polarizer for both polarizations and no modulated signal is observed. When inserted the difference in the refractive index real part  $\delta n$  of the sample rotates the vertically polarized light when passing it. It now has an additional small polarization component along the  $\pm 45^\circ$  axis compared to the circular states, which can pass the polarizer. Therefore, the intensity is modulated at twice the frequency of the PEM,  $2\omega_{PEM}$ . This can be seen by calculating the intensity using the Mueller-Matrix formalism and Eq. 3.11 [12, 50]:

$$\begin{aligned} I_2(t) &= \frac{I_0}{2} 10^{-A''} [1 - J_1(\delta_0) \ln(10) \Delta A'' \sin(\omega_{PEM} t) - J_2(\delta_0) \ln(10) \Delta A' \cos(2\omega_{PEM} t)] \\ &= I_{DC} - I_{AC,1} \sin(\omega_{PEM} t) - I_{AC,2} \cos(2\omega_{PEM} t) \end{aligned} \quad (4.8)$$

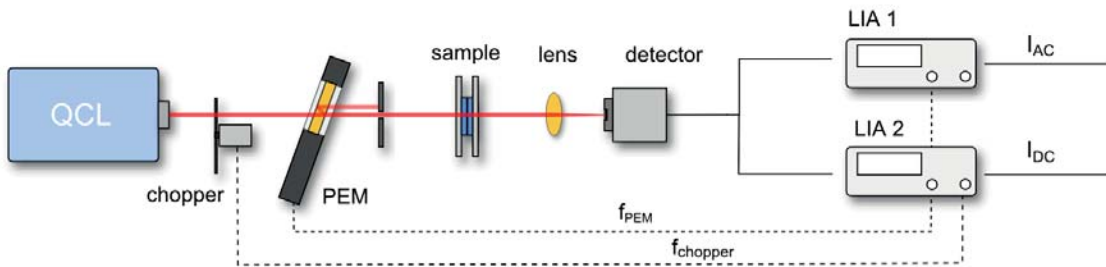


**Figure 4.1:** Setup used for QCL based VCD measurements, consisting of a quantum cascade laser (QCL), a photoelastic modulator (PEM), a liquid cell, an optical chopper, a lens, and an IR detector. The two lock-in amplifiers (LIA) are used to extract the VCD and IR signals (adapted from [P4]).

$J_1$  and  $J_2$  are the Bessel functions of the first and second order. By tuning the LIA to twice the PEM frequency it is possible to measure the amplitude  $I_{AC,2}$  and calculate the VCB spectrum:

$$\Delta A' = -\frac{2}{\ln(10) \cdot J_2(\delta_0)} I_{AC,2}/I_{DC} \quad \delta n = -\frac{1}{2\pi\nu z_0 \cdot J_2(\delta_0)} I_{AC,2}/I_{DC} \quad (4.9)$$

## 4.2 Optical setup

### 4.2.1 Quantum cascade laser-based setup for VCD measurements

The setup for the VCD measurements is shown in Fig. 4.1. A tunable external-cavity QCL (EC-QCL, Daylight Solutions TLS-21078) is used as the light source. It provides linearly polarized light with up to 200 mW (cw) in the spectral range of 1220–1320  $\text{cm}^{-1}$  (Fig. 4.2a). A ZnSe photoelastic modulator (Hinds PEM 80,  $f_{PEM} = 37$  kHz) is set to quarter-wave retardation at 1270  $\text{cm}^{-1}$ . To minimize noise at the modulation frequency due to etalon and interference effects the modulator is tilted. This allows the separation of the beam reflected inside the PEM from the transmitted beam. It is found that a tilt angle of  $\sim 30^\circ$  is sufficient (Fig 4.2b). The reflected beam is blocked by an aperture. After passing the sample cell the light is focused onto a detector. In a first configuration a thermoelectrically (TE) cooled Mercury-Cadmium-Telluride-detector (MCT) from VIGO System S.A. (PVMI-3TE-10.6) is used. It has a detectivity ( $D^*$ ) of  $3 \times 10^9$   $\text{cm}\sqrt{\text{Hz}}/\text{W}$  and a Silicon immersion lens. A

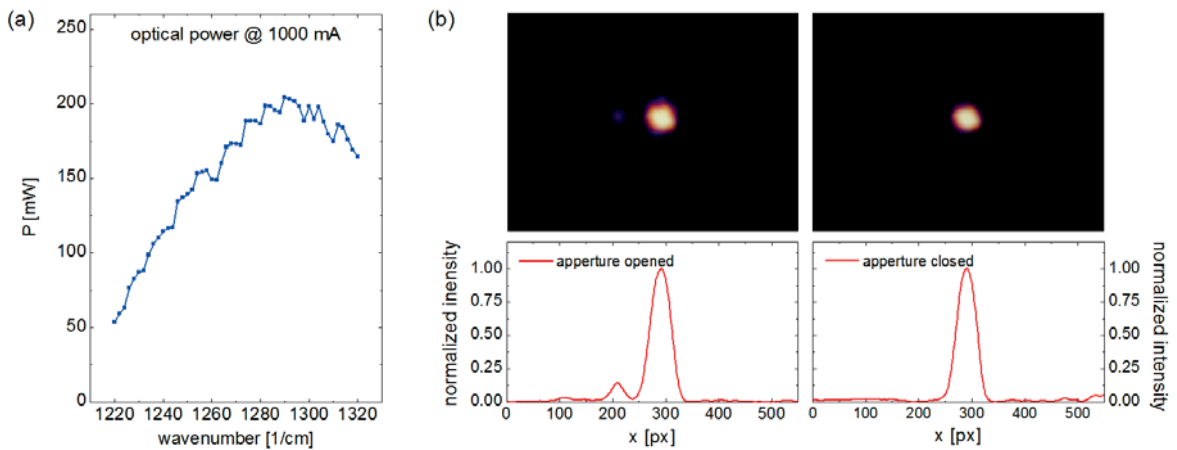


**Figure 4.2:** (a) Optical output power of the QCL in cw-mode at a laser diode current of 1000 mA. (b) MIR-camera images of the laser beam after passing the tilted PEM. The reflected beam is well separated and could be blocked by the aperture.

modified setup involves a MCT detector with liquid  $N_2$ -cooling and an enhanced detectivity ( $D^*$ ) of  $1 \times 10^{10} \text{ cm}\sqrt{\text{Hz}}/\text{W}$  (InfraRed Associates Inc., L-8575 HCT-70). Due to the small diameter and the collimation of the laser beam no additional focusing element (lens) was needed. It was therefore omitted in later experiments, also because MIR transparent lenses often exhibit small linear birefringence resulting in instrumental artifacts. Due to the AC coupling of both detectors an optical chopper is used to record the absorption spectra. The modulated detector signal is processed and recorded by two lock-in amplifiers (Stanford Research Systems SR830) locked to the PEM and the chopper frequency, respectively. Data were recorded by tuning the wavelength of the EC-QCL over the examined spectral region with a step size of  $0.5 \text{ cm}^{-1}$ . Each frequency data point is an average of 100 lock-in readings (time constant 100 ms), and standard deviations are used to gauge the noise. The measurement time for one scan was  $\sim 20 \text{ min}$ . Artifacts due to instrumental birefringence were reproducible and could thus be eliminated by background subtraction of the pure solvent spectra. To suppress higher-frequency spectral components, which are attributed to interference effects, the data were processed with a Fourier or a moving average filter set to a cutoff-frequency of  $4 \text{ cm}^{-1}$ , if not otherwise noted.

#### 4.2.2 Quantum cascade laser-based setup for VCB measurements

The VCB spectra were recorded using the slightly modified setup shown in Fig. 4.3. Here an additional polarizer is added right behind the sample with its transmission axis oriented at  $45^\circ$  with respect to the incoming vertically polarized laser light. One of the lock-in amplifiers is set to twice the PEM frequency  $2f_{PEM}$ . Data were taken and processed as mentioned above by scanning the wavelength in  $0.5 \text{ cm}^{-1}$  steps and averaging over 100 lock-in readings.

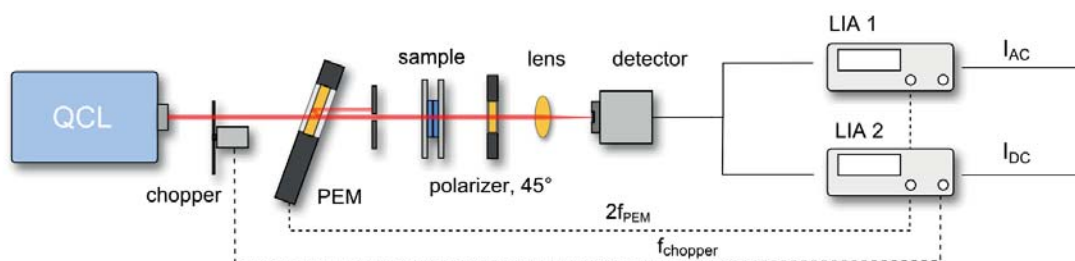


**Figure 4.3:** Slightly modified setup for QCL based VCB measurements. A polarizer is added right behind the sample. To extract the VCB signal one of the lock-in amplifiers is set to twice the PEM frequency  $2f_{PEM}$  (adapted from [P4]).

### 4.2.3 Reference spectra and theoretical calculations

VCD reference spectra were recorded on a Bruker Tensor 27 FTIR spectrometer equipped with a Bruker PMA 50 VCD side-bench module with a resolution of  $4\text{ cm}^{-1}$ . Each spectrum has been averaged over 20 min. For measurements between  $1800$  and  $800\text{ cm}^{-1}$  the photoelastic modulator (PEM) was set to quarter-wave retardation at  $1400\text{ cm}^{-1}$ . Since VCD and VCB are Kramers-Kronig transforms of one another, the VCB reference spectra are calculated from the VCD spectra. Theoretical calculations for the relative dipole and rotational strength have been performed by Dr. Steffen Lüdeke on basis of density functional theory (DFT). For this purpose the software *Gaussian03* was used on different levels of computation .

## 4.3 QCL based measurements of vibrational optical activity

The spectral region between  $1320\text{ cm}^{-1}$  ( $7.6\text{ }\mu\text{m}$ ) and  $1220\text{ cm}^{-1}$  ( $8.2\text{ }\mu\text{m}$ ) was examined for different chiral compounds. The QCL-based measurements are compared with those from a commercial Fourier transform (FT) VCD spectrometer (Bruker) and with the results of calculations. A modified VCD-setup comprising a MCT detector with liquid  $\text{N}_2$ -cooling and a different PEM was also tested.

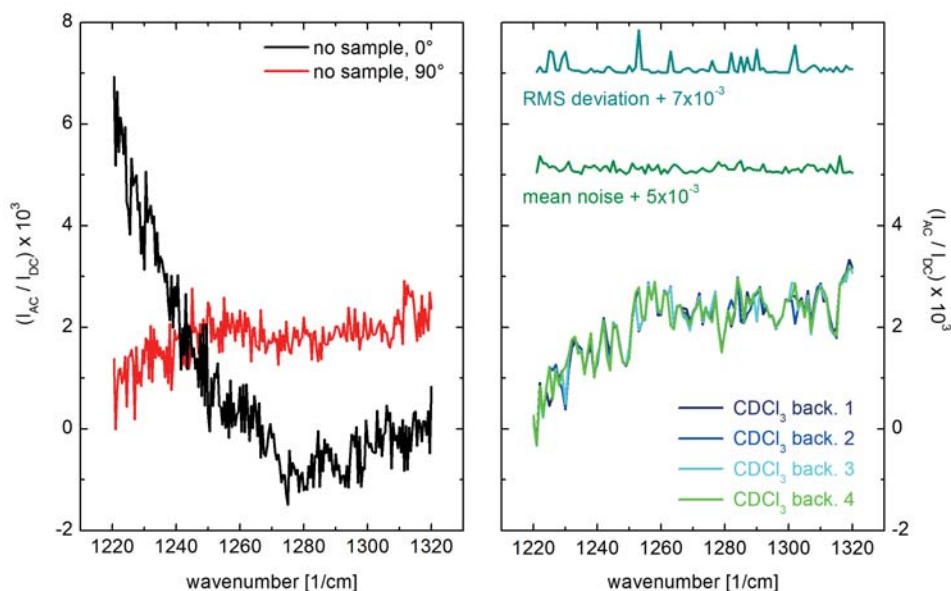


**Figure 4.4:** Background spectra taken for two orientations of the TE-cooled MCT detector (left panel). Four consecutively recorded background spectra for deuterated chloroform ( $\text{CDCl}_3$ ) in a 1 mm KBr-cell (right panel). See text for details.

### 4.3.1 Noise and stability

First the background stability and noise of the QCL-VCD-setup shown in Fig. 4.1 was tested. Two spectra with the sample cell removed were taken for two orientations of the TE-cooled detector. A rotation of  $90^\circ$  with respect to the optical axis reduced the artifacts caused by instrumental birefringence (Fig. 4.4). This is likely due to the polarization sensitivity of the detector as proposed by Nafie et al. [12, 51]. Afterwards four VCD spectra were taken consecutively for deuterated chloroform ( $\text{CDCl}_3$ ) filled in a 1 mm KBr-cell. The results are shown in Fig. 4.4. The high frequency artifacts in the data are attributed to interference effects inside the PEM. As can be seen, the solvent spectra are reproducible, which is important for background subtraction. This becomes obvious from the RMS-value of the deviations between consecutive spectra, shown in Fig. 4.4 together with the mean noise (average over the noise data of the four spectra). The RMS deviation has a mean of  $3 \times 10^{-4}$  and shows some spikes with a maximum value of  $8 \times 10^{-4}$ .

### 4.3.2 VOA measurements I: Ni-sparteine complex

The nickel-(–)-sparteine complex ( $\text{Ni(sp)Cl}_2$ ) was synthesized at the Institute of Pharmaceutical Science (University Freiburg) as described in the literature [52]. The open-shell complex exhibits strong VCD signals but has a molar absorptivity  $\epsilon$  comparable to those of

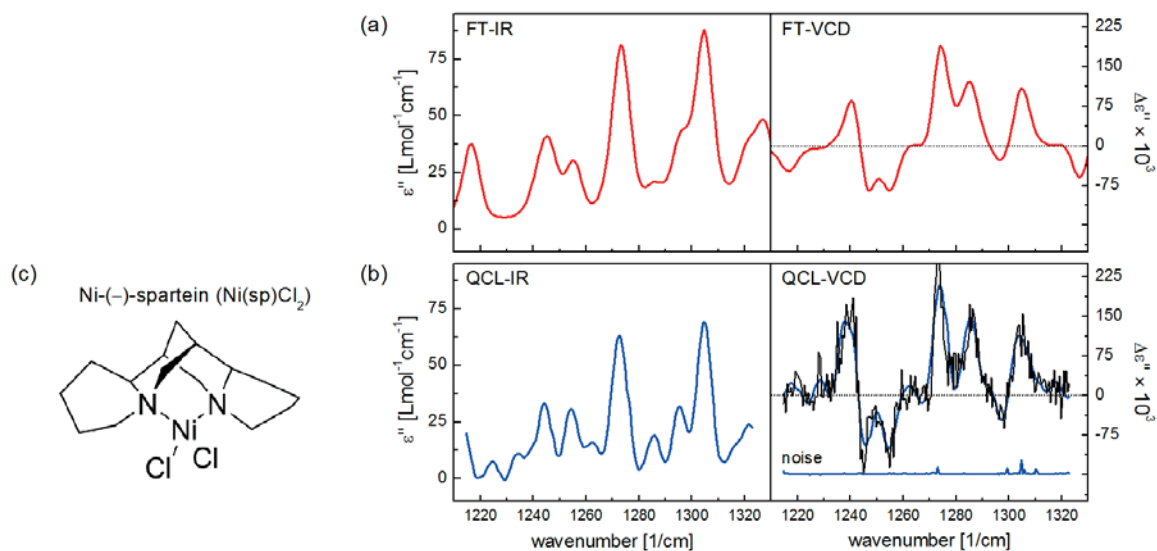


**Figure 4.5:** Vibrational spectra of a 200 mM solution of  $\text{Ni(sp)Cl}_2$  in  $\text{CDCl}_3$ . (a) FT-IR and FT-VCD data recorded in a  $100 \mu\text{m}$  path length  $\text{BaF}_2$  cell. (b) QCL based measurements taken in a  $1000 \mu\text{m}$  KBr cell. All spectra are shown with a resolution of  $4 \text{ cm}^{-1}$ . The black line is the raw unfiltered data. (c) Molecular structure of  $\text{Ni(sp)Cl}_2$ . (adapted from [?])

typical organic and inorganic molecules [53]. It has been shown, that the vibronic coupling of low-lying magnetic-dipole-allowed d-d transitions to the vibrational modes of the ground state results in a VCD enhancement for all modes [54]. Figure 4.5c shows the structure of the complex.

VCD and IR spectra were recorded with the QCL-based setup (Fig. 4.1) including the TE-cooled MCT detector. Together with measurements from a lamp-based FT instrument the results are depicted in Fig. 4.5. A 200 mM solution of the complex in deuterated chloroform  $\text{CDCl}_3$  was used in both cases. It was measured in either a 100  $\mu\text{m}$  path length  $\text{BaF}_2$  cell (FTIR) or a 1000  $\mu\text{m}$  KBr cell (QCL). All of the bands observed in the FT measurements (Fig. 4.5a) are clearly reproduced in the QCL spectra (Fig. 4.5b). Here additional spectral features can be seen. The QCL data were recorded with a scan step size of  $0.5 \text{ cm}^{-1}$  and processed with a  $4 \text{ cm}^{-1}$  Fourier filter in order to suppress the higher-frequency spectral components that are attribute to interference effects. This is illustrated by the unfiltered data also shown in Fig. 4.5b (black line).

### 4.3.3 VOA measurements II: Limonene

Non-polar aromatic terpenoids, such as pinene and limonene, are small, rigid molecules, and show few intra- and inter-molecular interactions, which allows for the accurate computation of their chiroptical properties using high-level *ab initio* or DFT methods [50, 55, 56]. In contrast to the chiral Ni-complex these compounds have no low-lying transitions and show therefore weaker VCD signals – typically  $10^{-4}$  to  $10^{-3}$  of the corresponding IR transitions

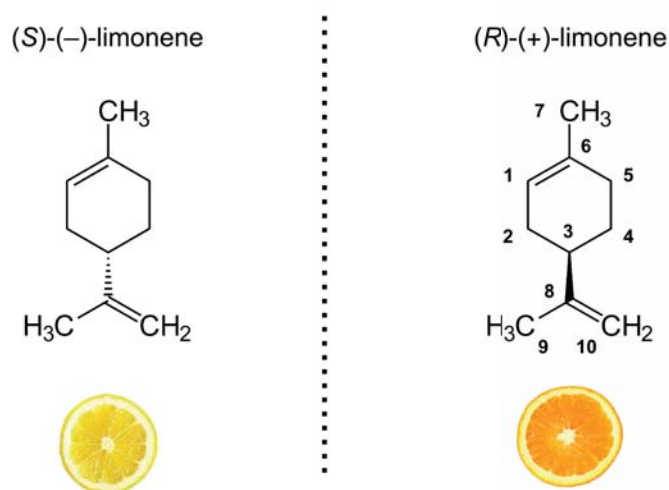


**Figure 4.6:** Structure of (*S*)-(-)- and (*R*)-(+)-limonene. The more common (*R*)-isomer of the aromatic terpenoid shows a strong smell of oranges whereas the (*S*)-configuration has a lemonlike aroma. (adapted from Wikimedia Commons)

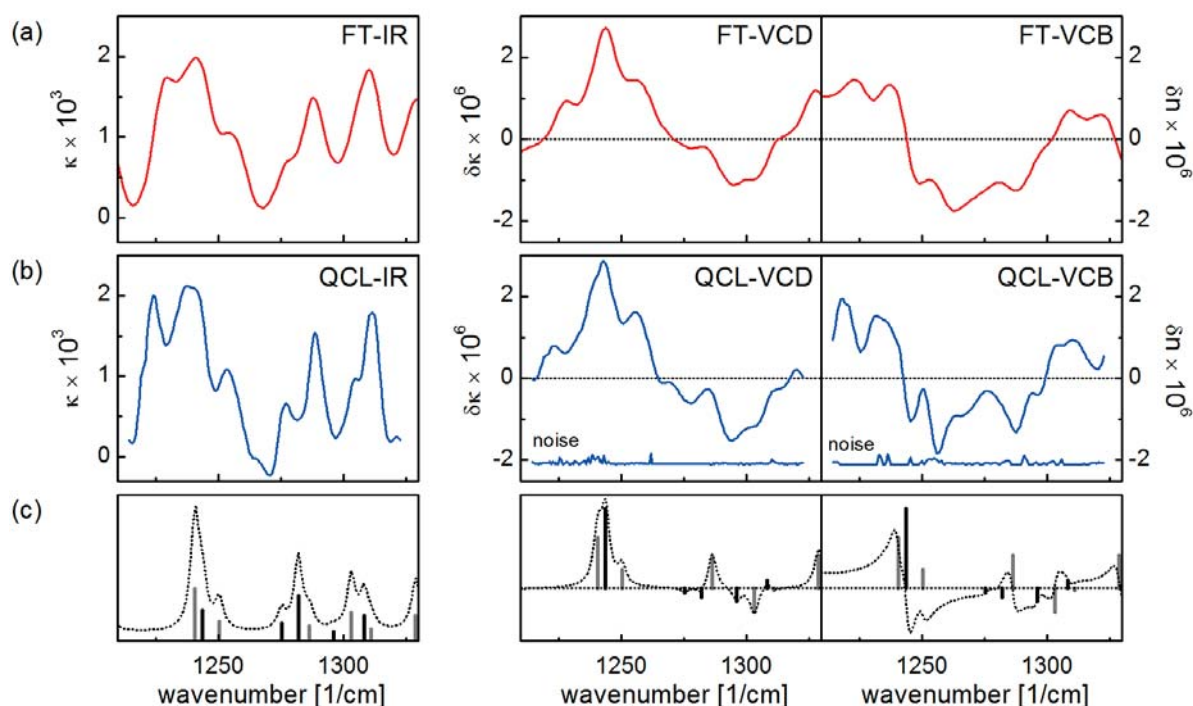


**Figure 4.7:** Spectra of a 3 M solution of (*R*)-(+)-limonene in  $\text{CDCl}_3$ . (a) FT-IR and FT-VCD spectra recorded in a  $100 \mu\text{m}$   $\text{BaF}_2$  cell, and FT-VCB data calculated from the corresponding VCD spectra. (b) QCL measurements recorded in a 1 mm KBr cell. All spectra are shown with a resolution of  $4 \text{ cm}^{-1}$ . (c) Theoretically predicted Boltzmann-weighted dipole and rotational strengths for the two most abundant conformers (grey and black vertical lines) convolved with dispersive (VCB) and absorptive (IR and VCD) Lorentzian line shape functions. (images adapted from [P3,P4]).

[39, 41, 57]. Here the terpenoid limonene was examined, a colorless liquid hydrocarbon which is the monoterpene most frequently found in natural products. It takes its name from lemons since most citrus fruits contain considerable amounts contributing to the odor of the fruits. The more common (*R*)-(+)-isomer shows a strong smell of oranges whereas (*S*)-(–)-limonene has a more lemon-like aroma. Limonene, and mainly the (*R*)-(+)-isomer, is used in chemical synthesis as a precursor to other terpenoids, as a biogenic solvent, or as a flavor for cosmetics and food. The molecular structures of both, (*R*)-(+)- and (*S*)-(–)-limonene, are shown in Fig. 4.6. VOA spectra have been measured using the QCL based setups shown before and the TE-cooled MCT detector (Fig. 4.1 and 4.3). All data are presented in refractive index units ( $\delta n$ ,  $\delta k$ ) and a resolution of  $4 \text{ cm}^{-1}$ . The QCL spectra were smoothed by Fourier-filtering. For both VCD and VCB a 3 M solution of (*R*)-(+)-limonene in  $\text{CDCl}_3$  was examined in the same sample cells as used for the chiral Ni-complex ( $100 \mu\text{m}$   $\text{BaF}_2$  cell (FTIR) or a  $1000 \mu\text{m}$  KBr cell (QCL)).

First the VCD spectrum of the limonene solution was recorded. In Fig. 4.7a and b we compare the respective FT and QCL vibrational spectra. The QCL measurements could

clearly reproduce all bands observed in the FT-spectra, as was the case in the Ni(sp)Cl<sub>2</sub> measurements shown before. Additionally the broad band around  $\approx 1308\text{ cm}^{-1}$  in the FT-IR spectrum, appears as a doublet ( $1311$  and  $1305\text{ cm}^{-1}$ ) in the QCL-IR spectrum. It corresponds to the in-phase wagging modes of the hydrogens at C1, C3, C4, and C5 (see Fig. 4.6 for atom numbering) with contributions from the two most abundant conformers, which are rotamers regarding the C3-C8 axis. Moreover the C-H twisting modes of these conformers at  $\sim 1240\text{ cm}^{-1}$  are resolved in the QCL-VCD data.

In Fig. 4.7 the measured QCL-VCB spectrum of the same limonene solution is shown together with FT-based data. Since VCD and VCB are Kramers-Kronig transforms of one another, the FT-VCB spectrum has been calculated from the FT-VCD reference spectrum (Fig. 4.7a). Compared to FT-VCB additional features are observed in the QCL-data, which also leads to an improved agreement with the calculation results.

The relative dipole and rotational strength for both conformers have been computed at the B3PW91/cc-pVTZ level. In Fig. 4.7c the calculation results are compared with the measured QCL data. The black and gray vertical lines represent the dipole and rotational strength for one or the other conformer, which were Boltzmann-weighted in respect to their relative energies ( $0.57$  and  $0.43$ , respectively). The black solid lines show calculated spectra, which are linear combinations of dispersive (VCB) and absorptive (IR and VCD) Lorentzian line shape functions weighted with the corresponding dipole or rotational strength. All data are shown with a resolution (linewidth) of  $4\text{ cm}^{-1}$ . Both, the VCD and VCB data taken with the QCL are in good agreement with the calculations.

#### 4.3.4 VOA measurements III: Proline

In contrast to nonpolar organic solvent/solute systems, aqueous solutions not only are strongly absorbing but also give rise to more complex solvation characteristics. Aqueous VCD studies are computationally and experimentally demanding, but often inevitable for systems of biological molecules. High concentrations of, for example, proteins and peptides are often necessary in order to allow for the use of short-path-length sample cells, which permit a sufficient transmission of intensity. This can lead to aggregation problems [5]. Nevertheless, some aqueous VCD studies have been reported with  $< 25\ \mu\text{m}$  cells [58–60]. Here the amino acid proline is examined. It is one of the twenty proteinogenic amino acids, and can be synthesized by the human body. The molecular structure of both zwitterion enantiomers is provided in Fig. 4.8, where it can be seen, that the common L form possesses *S* stereochemistry. Figure 4.9 shows the measured QCL-IR and VCD spectra of a 3 M aqueous solution taken in a  $100\ \mu\text{m}$  sample cell. The molar absorptivity of water in the studied spectral range is  $\sim 4.5\text{ Lmol}^{-1}\text{cm}^{-1}$  [61] so that the samples had an optical density of up to 3.5, of which 2.0 is due to water (Fig. 4.9a). Nevertheless, satisfactory spectra of L- and D-proline were observed, albeit with a slight asymmetry and noticeable noise in the

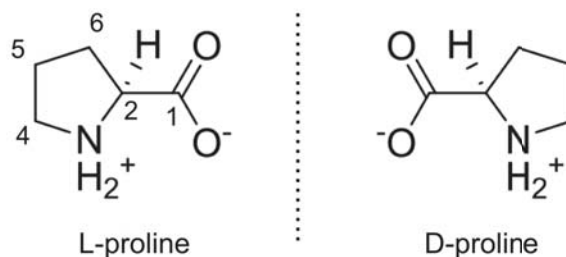


**Figure 4.8:** Structure of both enantiomers of the amino acid proline [P3]

optically dense parts of the spectrum. While a racemic mixture (3 M in water) was used for the background correction in Fig. 4.9b, pure water was used in the spectrum shown in the inset. Here the different strengths in the absorbance of the pure solvent and the solution resulted in a deviation of the corresponding baselines. This complicated the background subtraction and was responsible for the observed offset.

For the assignment of modes DFT calculations based on the B3LYP/6-311++G(d,p) model were performed combined with a polarized continuum model (PCM) to simulate the influence of water [62]. Previous studies of zwitterionic L-proline in aqueous solution iden-

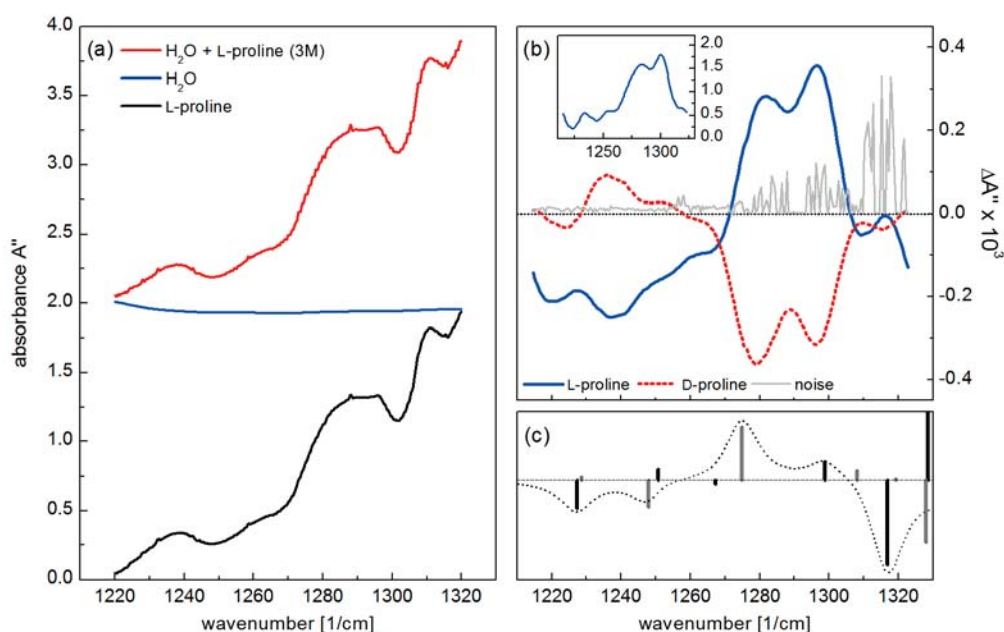


**Figure 4.9:** Vibrational spectra of 3 M aqueous solutions of proline. (a) IR-absorbance of  $\text{H}_2\text{O}$  and L-proline, showing an optical density of up to 3.5 for the solution. (b) QCL-VCD spectra of L- and D-proline in a  $100 \mu\text{m}$   $\text{CaF}_2$  cell. Data were background-corrected using a racemic mixture (Inset: corrected with pure water). (c) Relative VCD intensities computed for the two ring-puckering conformers of L-proline (gray and black vertical lines). (adapted from [P3])

tified two dominant ring-puckering conformers equally populated corroborated by NMR data [63]. The results of the rotational strength for both conformers are shown in Fig. 4.9c (black and gray vertical lines) together with the corresponding theoretical spectrum (dotted line) [P7]. On the basis of the results, the two positive bands at  $1295\text{ cm}^{-1}$  and at  $1286\text{ cm}^{-1}$  in the measured spectra are most likely explained by wagging vibrations of one conformer ( $1299\text{ cm}^{-1}$ ) and H-N-C2 bending of the other conformer ( $1275\text{ cm}^{-1}$ ) (see Fig. 4.8 for atom numbering). The two negative bands at  $1248\text{ cm}^{-1}$  and  $1227\text{ cm}^{-1}$  in the theoretical spectrum are correlated to twisting and rocking of ring protons of the two conformers. Both can be seen in the measured spectrum as a small dip at  $1253\text{ cm}^{-1}$  and a band at  $1239\text{ cm}^{-1}$ . The strong negative band at  $1317\text{ cm}^{-1}$  in the theoretical spectrum originates from carboxylate bending and C-C stretching of C1 and C2. It just appears as a decline at the end of the measured spectrum.

### 4.3.5 Modified optical setup

The sensitivity of the QCL-based setup presented in the previous section is primarily limited by the reproducibility of the high-frequency background due to interference effects inside the PEM (Fig. 4.4) and the sensitivity of the detector. The latter is especially important for measurements of strongly absorbing samples, i.e. aqueous solutions. To further reduce the interference artifacts the PEM was replaced by a different photoelastic modulator. Apart from a higher modulation frequency of  $f_{PEM2} = 70\text{ kHz}$  the new PEM also provided an optical element with an anti-reflection coating. This resulted in reduced

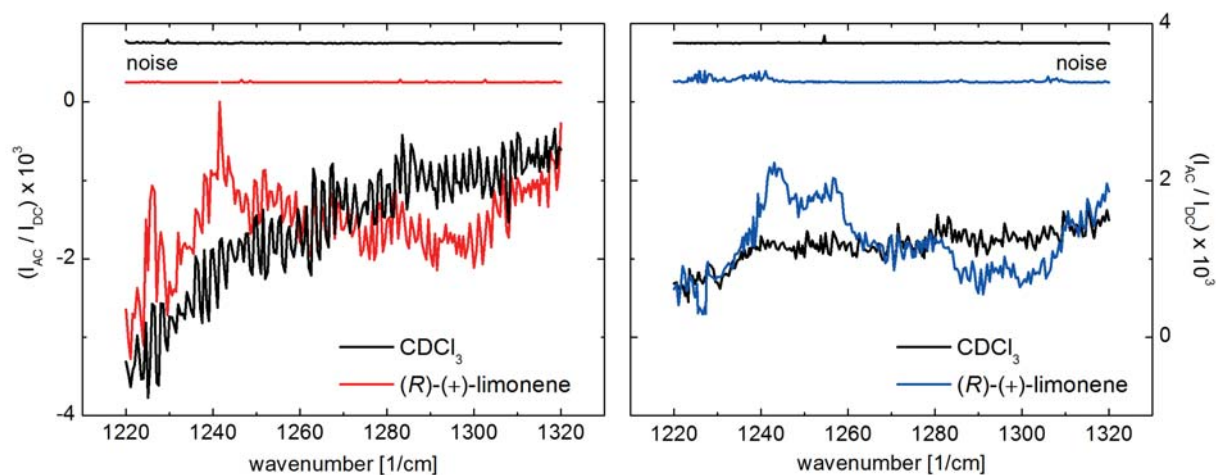


**Figure 4.10:** Comparison of VCD data taken before (left panel) and after (right panel) the replacement of the PEM. A reduction of the high-frequency components due to the anti-reflection coating of the new modulator is clearly visible.

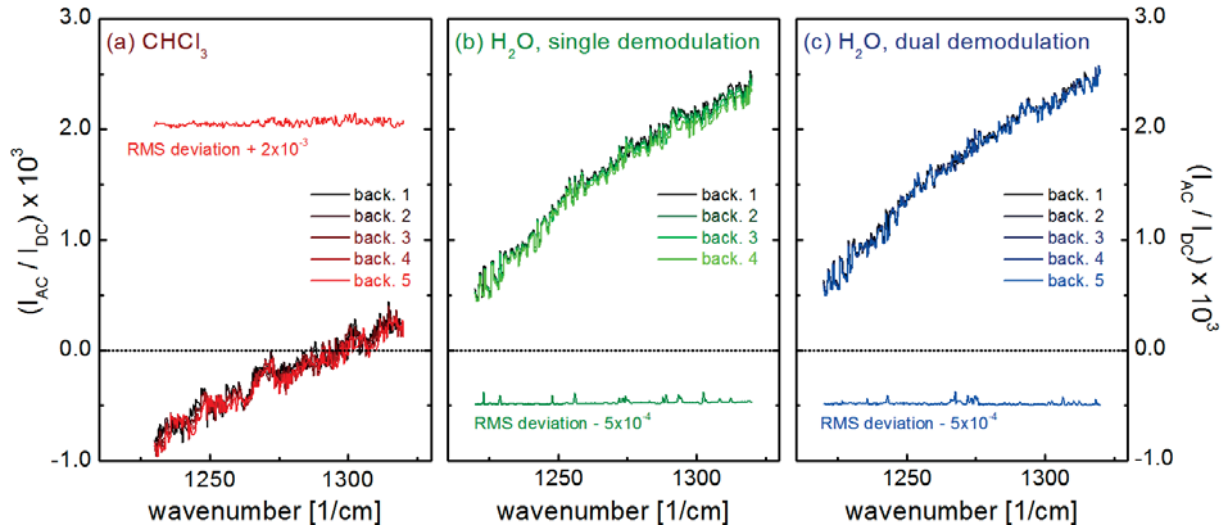


**Figure 4.11:** Test of the repeatability of the modified setup. Shown are consecutively recorded spectra of (a)  $\text{CHCl}_3$  and (b)  $\text{H}_2\text{O}$ . (c) For the water measurements a dual demodulation technique according to [64] has also been tested. RMS deviations are depicted with offsets for clarity.

background artifacts as can be seen in Fig. 4.10. Here the VCD data taken before and after the replacement of the PEM are compared with each other. Both, a 3 M solution of (*R*)-(+)-limonene and the pure solvent  $\text{CDCl}_3$  have been measured in a 1 mm KBr cell. The reduction of the high-frequency components is clearly visible.

To further increase the sensitivity, the TE-cooled detector was replaced by the MCT detector with liquid  $\text{N}_2$  cooling providing an enhanced detectivity. The stability of the modified setup was tested by consecutively taking 4 to 5 background spectra. The RMS deviations between successive data sets are shown in Fig. 4.11 with results for both chloroform ( $\text{CHCl}_3$ ) and pure water filled in a 1 mm-KBr or a  $100 \mu\text{m}$ - $\text{CaF}_2$  cell, respectively. Compared to the previous results (Fig. 4.4) a decreased RMS deviation is observed (Tab. 4.1). For  $\text{CHCl}_3$  (Fig. 4.11a) the deviation shows a mean value of  $6 \times 10^{-5}$  and a maximum

	mean value	maximum
setup 1, $\text{CDCl}_3$	$3 \times 10^{-4}$	$8 \times 10^{-4}$
setup 2, $\text{CDCl}_3$	$6 \times 10^{-5}$	$1.5 \times 10^{-4}$
setup 2, single demodulation, $\text{H}_2\text{O}$	$3 \times 10^{-5}$	$1.3 \times 10^{-4}$
setup 2, dual demodulation, $\text{H}_2\text{O}$	$2 \times 10^{-5}$	$1.3 \times 10^{-4}$

**Table 4.1:** Mean and maximum values for the RMS deviation of the different setups. Setup 1 comprises a TE-cooled detector and a modulator without coatings. Setup 2 has a detector with  $\text{LN}_2$  cooling and a modulator with anti-reflection coating.

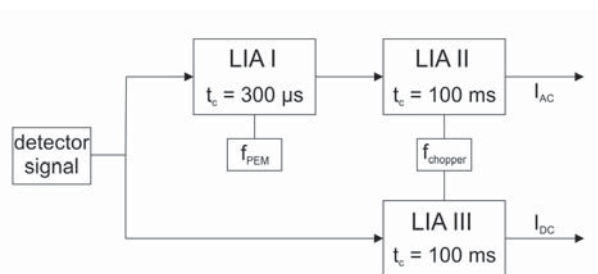


**Figure 4.12:** Schematic drawing of the electronic layout for the double demodulation technique following [64] using three lock-in amplifiers (LIA). See text for details.

of  $1.5 \times 10^{-4}$ . For the water measurements a slightly reduced mean value of  $3 \times 10^{-5}$  is achieved (Fig. 4.11b). This is in part because of the reduced laser power at the detector due to the strong absorbance. The MCT detector is noisy if operated near saturation. As before, the RMS deviation shows spikes with maximum values up to  $1.3 \times 10^{-4}$ . They are attributed to wavelength tuning errors of the QCL, i.e. the wavelength slightly varies from scan to scan. For the pure water sample a double demodulation detection scheme according to [64] was also tested (Fig. 4.11c). Here the detector signal is processed by three lock-in amplifiers (LIA) to further suppress background noise. One LIA is still locked to the chopper frequency providing the MIR absorption spectra. The remaining two LIAs are locked to the PEM and the chopper frequency, respectively. The LIA locked to the PEM is operated with a short time constant ( $t_c = 300 \mu s$ ) and its output signal is fed into the third LIA locked to the chopper. Therefore only signals modulated both at the PEM and the chopper frequency are detected. A small improvement of the RMS deviation is observed resulting in a mean deviation of  $2 \times 10^{-5}$ .

#### 4.3.6 VOA measurements IV: Test of the modified setup

The modified setup is further tested with VCD measurements of different samples using the dual demodulation technique. All spectral data were recorded as before through wavelength tuning and averaging over 50 lock-in readings. The data shown were processed with a  $4 \text{ cm}^{-1}$  moving average (limonene, BINOL) or a Fourier filter of  $4 \text{ cm}^{-1}$  (proline). First the vibrational spectra (IR and VCD) of 3 M solutions of (*R*)-(+)- and (*S*)-(-)-limonene in  $\text{CDCl}_3$  were measured in the 1 mm KBr cell. The results are depicted in Fig. 4.13 in absorbance units with a resolution of  $4 \text{ cm}^{-1}$  after filtering. All VCD bands are clearly seen as mirror image spectra for both enantiomers. The slight difference in the absolute values is likely due to small differences in the concentration of the solutions.

A second sample was prepared with the chiral organic compound BINOL (1,1'-Bi-2-naphthol). It finds use as a ligand in catalyzed stereo selective synthesis [65, 66]. The enantiomers of

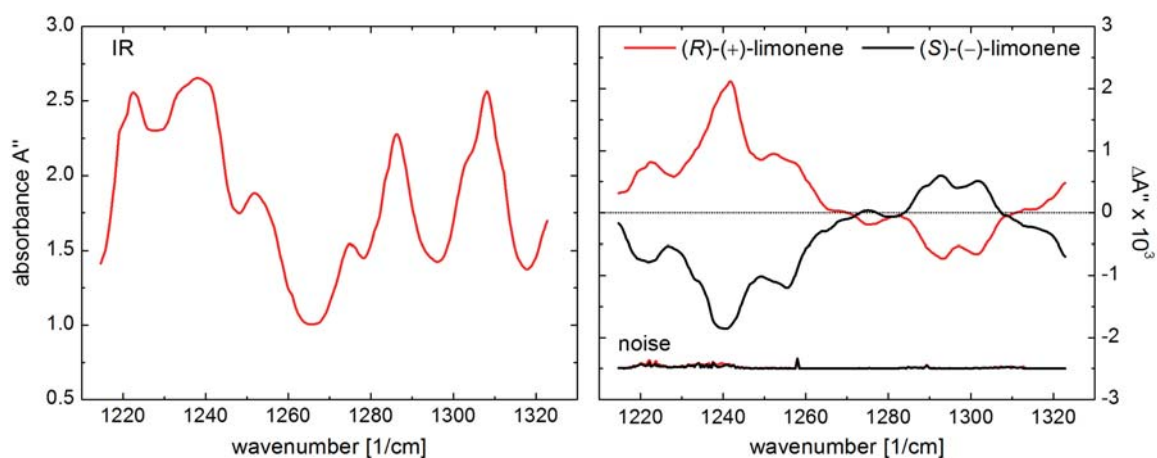


**Figure 4.13:** Vibrational spectra (IR: left panel, VCD: right panel) for a 3 M solution of both limonene enantiomers recorded with the modified QCL setup in a 1 mm KBr cell. (adapted from [P8])

BINOL exhibit axial chirality (Fig. 4.14). They can either be separated by high-performance liquid chromatography (HPLC) with chiral stationary phases [67] or synthesized separately in enantioselective reactions [68]. For both enantiomers, (*M*)- and (*P*)-BINOL a 150 mM solution in  $\text{CDCl}_3$  was prepared and measured in a 1 mm KBr cell. The corresponding IR and VCD spectra are shown in Fig. 4.15. As expected, the VCD signals of the two enantiomers resolve and reproduce almost all bands with opposite signs.

Finally the aqueous solution (3 M) of L-proline was investigated in the  $100 \mu\text{m}$   $\text{CaF}_2$  sample cell as used before (Sec. 4.3.4). Figure 4.16 shows the corresponding IR and VCD spectra. Due to the enhanced sensitivity of the  $\text{LN}_2$ -cooled detector, the pure solvent ( $\text{H}_2\text{O}$ ) and solution measurements showed no baseline deviations. Therefore a water spectrum could be used for VCD background subtraction. Compared to the previous results (Fig. 4.9b and inset), the data could be recorded with reduced noise and no observable offset. An enhancement of the mean signal-to-noise (SNR) ratio from 28 to 40 was observed. Additionally the negative band at  $1248 \text{ cm}^{-1}$  in the calculated spectrum (Fig. 4.9c) originating from

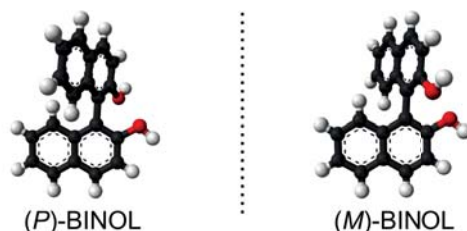


**Figure 4.14:** Molecular structure of both BINOL (1,1'-Bi-2-naphthol) enantiomers. The organic compound exhibits axial chirality. (images taken from Wikimedia Commons)

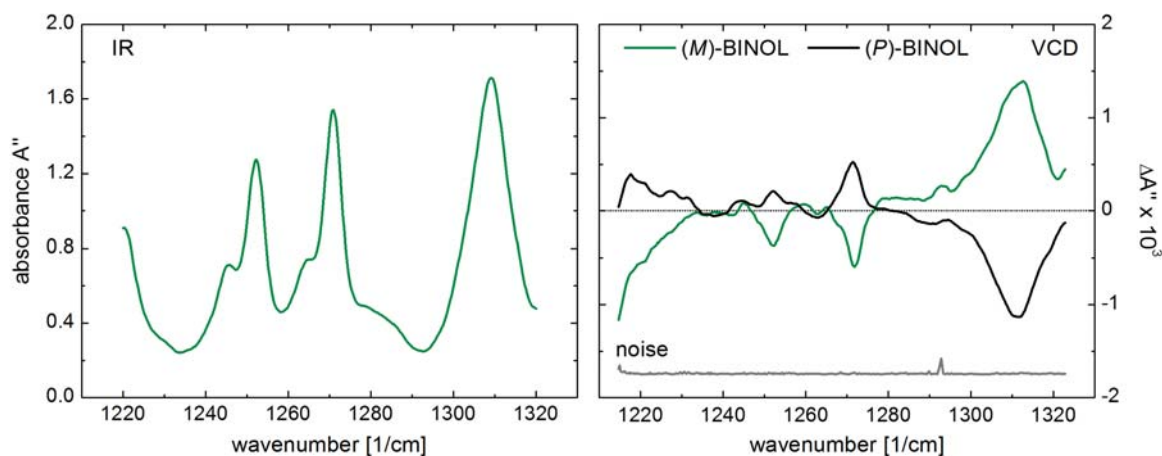


**Figure 4.15:** IR (left panel) and VCD (right panel) spectra for a 150 mM solution of (*M*)- and (*P*)-BINOL in  $\text{CDCl}_3$ . Both solutions have been measured in a 1 mm KBr cell with the modified QCL-setup. (adapted from [P8])

twisting and rocking of ring protons is now clearly visible in the measured spectrum as a small negative band at  $1253 \text{ cm}^{-1}$ .

The enhanced sensitivity and reproducibility of the modified QCL-based VCD-setup are promising for time-resolved studies of optical activity in aqueous solutions. This is also supported by the moderate measurement time of  $\sim 20$  min compared to aqueous studies with FTIR-VCD instrumentations. While IR absorbance measurements just reveal substance-specific informations of a sample, VCD in contrast provides information about the three dimensional arrangement of the molecule, i.e. configuration and conformation. The chiral

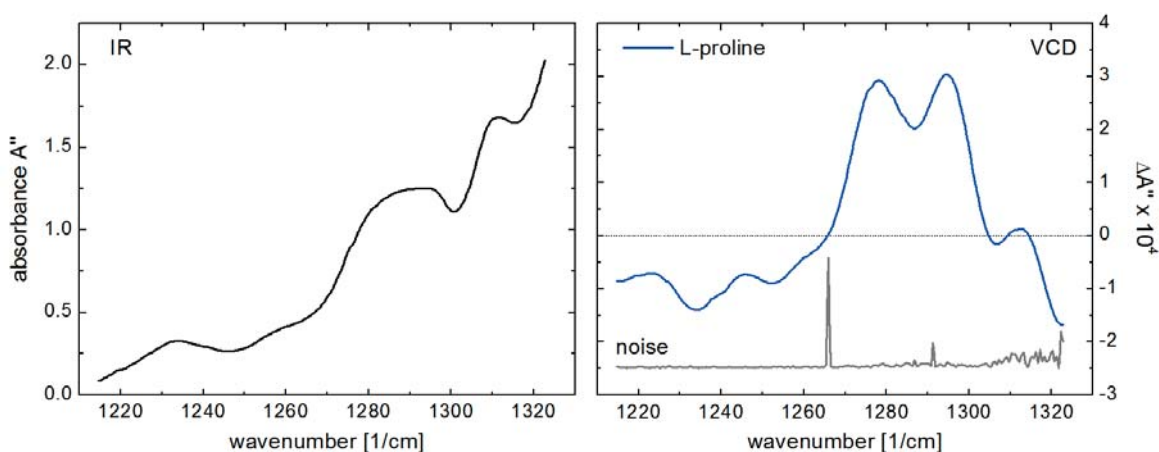


**Figure 4.16:** Vibrational data for a 3 M aqueous solution of L-proline measured in a  $100 \mu\text{m}$   $\text{CaF}_2$  cell using the modified setup. Due to the enhanced sensitivity data could be background corrected with pure water and recorded with reduced noise (see Fig. 4.9).

information from VCD spectra can also be evaluated quantitatively. The potential of VCD for real-time monitoring of enantiomeric excess (ee) had recently been demonstrated [69]. This might be useful to optimize reaction conditions leading to a maximum ee (enantiomeric excess) which may not be the same yielding maximum product. For enantioselective (enzymatic) reactions for example, maximum ee is often achieved before maximum yield and may decrease again over time [70]. The time resolution of such reaction-monitoring measurements depend on the signal to noise (SNR) ratio of the used setup. With the actual setup it is possible to follow a reaction at a rate of a spectrum every  $\sim 20$  minutes. By further increasing the SNR and reproducibility of the QCL measurements the time resolution could be further increased.

A first test of the use of laser-based VCD spectroscopy for reaction monitoring was performed in collaboration with the group of Dr. S. Lüdeke (University Freiburg) [P7, P9]. Therein the change of the VCD signals of an aqueous proline solution due to protonation of the amino acid have been investigated. The pH-value of the solution was changed from 11.5 to 2 by titration with hydrochloric acid (HCl) in  $\sim 400$  minutes, where spectra were recorded every 20 minutes. Significant changes in the signals reproduced by both enantiomers (L- and D-proline) could be observed. All results and further details are going to be published in [P7, P9]. These studies show that reactions involving chiral compounds in aqueous solutions can be followed and the IR and VCD spectra recorded.



# 5

## Mid-Infrared Refractometry

Typically, absorption spectroscopy is based on measuring intensity changes to reveal vibrational resonances, which in turn require stable light sources if weakly absorbing (e.g. dilute) species are to be detected. However, despite the higher power levels and the compact rugged design, quantum cascade lasers (QCL) are often plagued by intensity fluctuations, which affect the achievable sensitivity in absorption measurements. In this chapter it is therefore examined how vibrational spectra may be obtained without direct measurement of the QCL's intensity.

The infrared spectrum of molecules is mostly characterized by distinct absorption bands, i.e. imaginary part of the refractive index. The Kramers-Kronig transformation relates the real ( $n(\nu)$ ) and imaginary ( $\kappa(\nu)$ ) parts of the complex refractive index  $\tilde{n} = n + i\kappa$  of a medium, as has been shown in chapter 2. It follows that knowledge about the real part is sufficient to obtain the imaginary part and *vice versa*. The refractive index real part is generally observed via changes in beam direction and chiral refractometer (see for instance in chapter 3). Changes in the real part of the refractive index across an absorption band in the MIR can be much larger than what is commonly observed at visible frequencies. For instance, across the  $\sim 700 \text{ cm}^{-1}$  resonance a benzene solution's real part of the index changes by  $\pm 0.6$  refractive index units [71]. This raises the question whether the change in the real part can give rise to a measurable deflection of the IR beam. Observing the deflection as a function of wavelength could then be related to the IR absorption band.

The measurement of refractive indices (refractometry) is well established in the visible [72]. Efforts have been made to transfer some of those methods to the MIR and these include refractometry with a hollow prism, an Abbe refractometer, or using interferometric methods [73–78]. An early refractive index measurement by Pfund et al. in 1935 [79] recorded the dispersion of  $\text{CS}_2$  and  $\text{CCl}_4$  in the solvents' transparent IR regions. Fahrenfort et al. [80]

used attenuated total reflection (ATR) to measure the optical constants of benzene. They showed that the refractive index can be calculated from a measurement of the reflectivity for two angles of incidence. However, since all these methods rely on absolute intensity measurements, they all have problems acquiring refractive index data for strongly absorbing samples.

Here, a more convenient experimental geometry involving a QCL is examined, whereby the change in the index is observed in an imaging setup. It is a form of refractometry where the beam of a QCL is imaged on an infrared camera. The change in the beam profile at a total internal reflection interface is used to deduce the absorption peak without measuring absolute intensities. Furthermore it is possible to simultaneously extract  $n(\nu)$  and  $\kappa(\nu)$  of the analyte, as will be shown next. Since only relative intensity measurements within the beam profile are made this technique should be immune to the QCL's intensity fluctuations.

After describing the theoretical model and experimental setup, measurements on dichloromethane (DCM) are presented. How this approach may also be applied to chiral liquids is discussed. Parts of this chapter have been published in [P5].

## 5.1 Experimental setup

The experimental setup for the MIR-refractometer is shown in Fig. 5.1. The Quantum Cascade Laser (QCL, Daylight Solutions TLS-21078) also used for the VCD measurements shown in the previous chapter, provides linearly polarized light in the spectral range of  $1220 - 1320 \text{ cm}^{-1}$ . The horizontal polarization of the laser is defined by the polarizer P1. The laser beam is expanded and collimated with two spherical mirrors (SM1 with

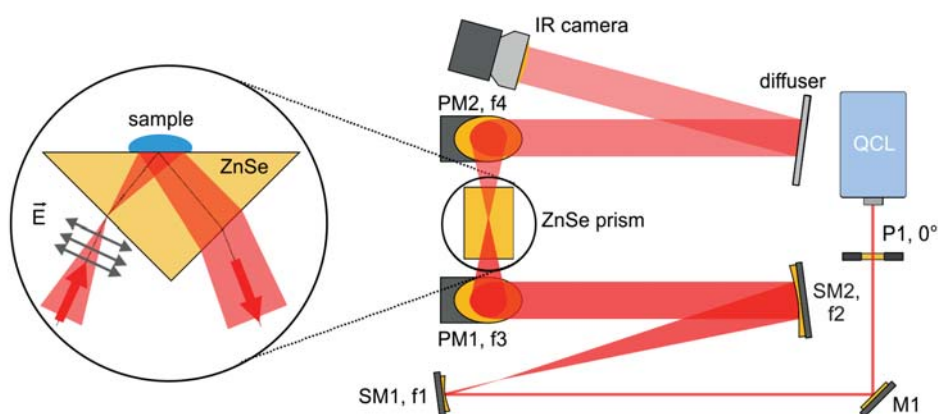


**Figure 5.1:** Setup of the MIR-refractometer (top-down view). The linearly polarized light of a QCL is expanded, collimated and finally refocused onto the entrance side of a ZnSe-prism. The inset is a detailed view of the prism (side-view). (adapted from [P5])

$f1 = 25$  mm and SM2 with  $f2 = 200$  mm) to a beam diameter of  $d = 30$  mm. The beam is then focused onto the entrance surface of a ZnSe-prism with a parabolic mirror (PM1 with  $f3 = 101.6$  mm). After reflection at the prism/sample interface the beam exits the prism (see inset of Fig. 5.1). After re-collimation with a second parabolic mirror PM2 ( $f4 = 101.6$  mm) the beam is directed onto a diffuser. The attenuated reflection of the laser beam's profile is imaged by a infrared camera ( $640 \times 480$  pixels, Thermoteknix Miricle 307K-25u). Because the focus is at the entrance face of the prism, the angle of incidence at the prism/sample interface varies across the beam profile. If no sample is present (prism/air), then all angles fulfill the condition for total internal reflection (TIR) and the entire beam is reflected. However, when a sample with an index of refraction  $n > 1$  is present, then the condition for TIR is no longer fulfilled for all angles. It follows that the intensity profile imaged by the camera will no longer be symmetric, as parts of the beam will be transmitted into the sample where they also experience absorption. It is now shown that the complex refractive index  $\tilde{n}$  of the sample can be measured by detecting and analyzing this intensity profile.

## 5.2 Theoretical model

The angle of incidence (AOI)  $\gamma_0$  of the center of the beam at the second surface of the prism (Zn-Se prism/sample interface) is a function of the AOI  $\alpha_0$  at the entrance side of the prism, as can be seen in Fig. 5.2a. The prism has a refractive index  $n_p$  and prism angle  $\theta_1$ , therefore we can write:

$$\gamma_0 = \theta_1 + \arcsin \left[ \frac{1}{n_p} \sin \alpha_0 \right] \quad (5.1)$$

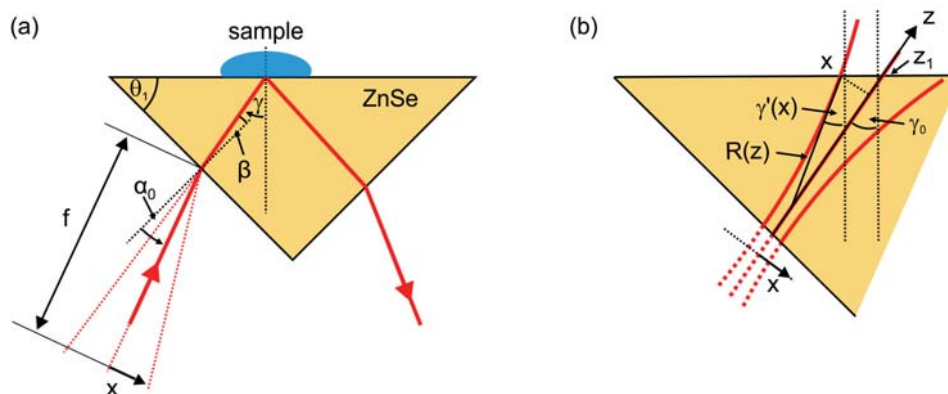


**Figure 5.2:** Detailed views of the beam path inside the prism for (a) geometrical ray optics (b) a Gaussian beam profile. (taken from [P5])

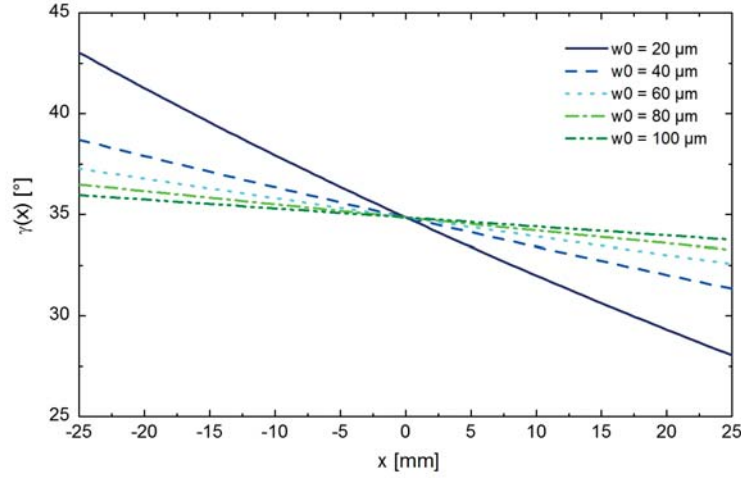


**Figure 5.3:** Comparison of  $\gamma(x)$  for a Gaussian beam profile with different beam waists  $w_0$  at the focus

Accounting for the spatial extent of the beam ( $x$ ) with Gaussian beam optics a waist  $w_0$  is assumed for the beam profile at the entrance surface of the prism. The beam's lateral components propagate a distance  $z(x)$  to the second surface of the prism (prism/sample interface), which depends on their distance  $x$  from the center of the beam. The radius of curvature of the wavefront is  $R(z(x)) = R(x)$  at the intersection with the prism/sample interface (Fig. 5.2b). The angle of incidence  $\gamma(x)$  at this point is defined by the surface normal and  $R(x)$ :

$$\gamma(x) = \gamma_0 - \arcsin \left[ \frac{x}{R(x)} \right] = \theta_1 + \arcsin \left[ \frac{1}{n_p} \sin \alpha_0 \right] - \arcsin \left[ \frac{x}{R(x)} \right] \quad (5.2)$$

The radius  $R(x)$  is further defined as [81]:

$$R(x) = z(x) \left[ 1 + \left( \frac{z_0}{z(x)} \right)^2 \right] \quad \text{with} \quad z_0 = \frac{\pi w_0^2}{\lambda/n_p} \quad (5.3)$$

The distance  $z(x)$  is described by  $z(x) = z_1 + x \cdot \tan \gamma_0$  where  $z_1$  is shown in Fig. 5.2b. It has been experimentally determined that  $z_1 = 10.8$  mm. The variation of the angles of incidence over the beam cross section follow if Eq. 5.3 is inserted into Eq. 5.2:

$$\gamma(x) = \gamma_0 - \arcsin \left\{ \frac{x}{z_1 + x \cdot \tan \gamma_0} \cdot \left[ 1 + \left( \frac{z_0}{z_1 + x \cdot \tan \gamma_0} \right)^2 \right]^{-1} \right\} \quad (5.4)$$

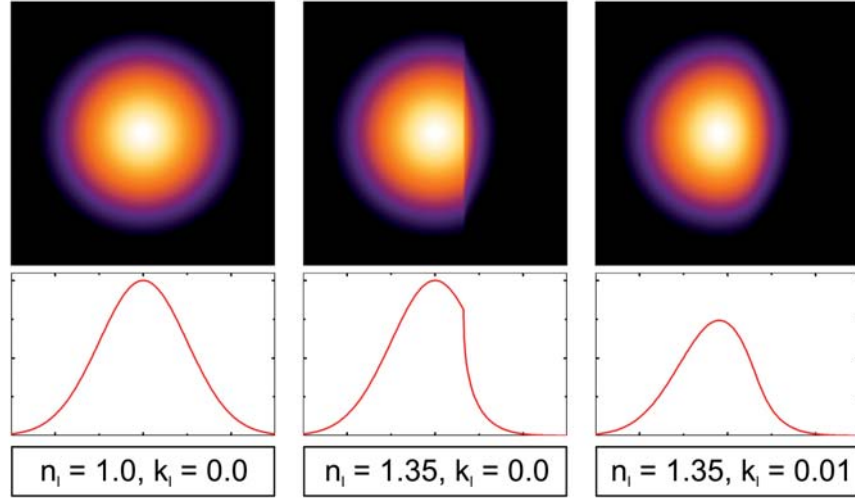


**Figure 5.4:** Calculations of the predicted intensity profile for model liquids with different values of the refractive index  $\tilde{n}_l$  using Eq. 5.6 with  $w_0 = 30 \mu\text{m}$ ,  $\alpha_0 = 25^\circ$ ,  $\theta_1 = 45^\circ$  and  $n_p = 2.4$  [P5].

For different values of the beam waist, i.e. focus spot size  $w_0$  the angle  $\gamma(x)$  is calculated and shown in Fig. 5.3. It is obvious, that the smaller the focus spot is, the more pronounced is the variation of  $\gamma(x)$  over the beam cross section. The polarization of the beam is chosen such that it is  $p$ -polarized, i.e. parallel to the plane of incidence at the prism/sample interface. Therefore the Fresnel coefficients for the reflected beam components are calculated to be [15]:

$$r_p(x) = \frac{\tilde{n}_l^2 \cos \theta_x - n_p \sqrt{\tilde{n}_l^2 - n_p^2 \sin^2 \gamma(x)}}{\tilde{n}_l^2 \cos \theta_x + n_p \sqrt{\tilde{n}_l^2 - n_p^2 \sin^2 \gamma(x)}} \quad (5.5)$$

Here the liquid sample is assumed to have the complex index of refraction  $\tilde{n}_l = n_l + i\kappa_l$ . The intensity profile detected by the IR camera can now be calculated assuming a Gaussian profile:

$$I_1(x,y) = I_0(x,y) \cdot |r_p(x)|^2 \quad \text{with} \quad I_0(x,y) = I_0 e^{-2\frac{x^2+y^2}{w^2}} \quad (5.6)$$

The real and imaginary components of the liquid's index of refraction  $n_l$  and  $\kappa_l$  may now be determined by fitting Eq. 5.6 to the experimentally detected intensity profile. Theoretical beam profiles after reflection are shown in Fig. 5.4 for a Gaussian beam with a focus spot size of  $w_0 = 30 \mu\text{m}$  and different values of the liquid's refractive index  $\tilde{n}_l$  (here  $\alpha_0 = 25^\circ$ ,  $\theta_1 = 45^\circ$  and  $n_p = 2.4$ ).

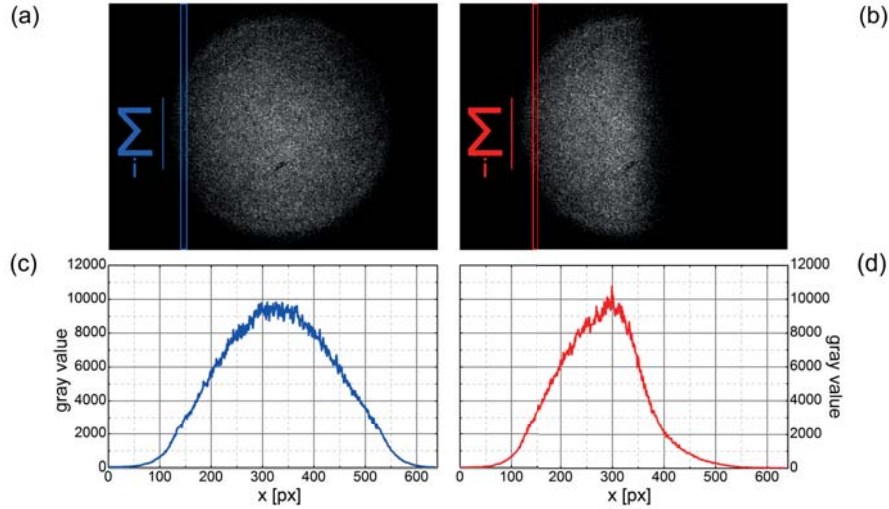


**Figure 5.5:** Image analysis and data processing. Shown are two camera images, one without (a) and one with (b) liquid sample. The gray scale values of the images are added as indicated in the figure. Equation 5.6 is fitted to the one-dimensional profiles (c, d). (adapted from [P5])

### 5.3 Measurements

Dichloromethane (DCM) exhibits an absorption peak in the tuning range of the QCL (see FTIR measurement, Fig. 5.7 rhs.) and serves as a model solution to test the MIR-refractometer. Less than 100  $\mu\text{l}$  of neat (undiluted) DCM are pipetted on the upper surface of the prism. The QCL is then wavelength-scanned in 1  $\text{cm}^{-1}$  steps over the complete tuning range and an image is recorded by the IR-camera for each step. The images are processed as schematically shown in Fig. 5.5. First, all the gray scale values for each camera pixel-column are summed to obtain a 1-D beam profile. A theoretical fit of Eq. 5.6 to this profile reveals both,  $n_l$  and  $\kappa_l$ .

The focus spot size  $w_0$ , important for the calculation of  $\gamma(x)$ , is determined for each wavelength using an ABCD-matrix formalism [81] together with measurements of the beam waist directly behind the laser. Thus camera images are taken without a sample. A fit of the resulting 1-D profiles with a Gaussian function (Eq. 5.6) shows a linear decrease of the beam diameter of the laser with increasing wavenumber (Fig. 5.6a). The beam waist is measured at three wavelengths in the interval between 1220  $\text{cm}^{-1}$  and 1320  $\text{cm}^{-1}$  (movable detector and a razor blade). The other values are calculated by a linear approximation (Fig. 5.6b). For the ABCD-matrix algorithm the so called complex beam parameter  $q$  is defined as [81]:

$$\frac{1}{q} = \frac{1}{R} - i \frac{\lambda}{\pi w^2} \quad (5.7)$$

where  $R$  is the radius of curvature of the wavefront and  $w$  the beam radius. So both,  $R$  and  $w$ , are given by the real and imaginary part of  $q$ . The parameter  $q_2$  of a Gaussian beam after passing an optical system is related to the beam parameter  $q_1$  at the entrance by:

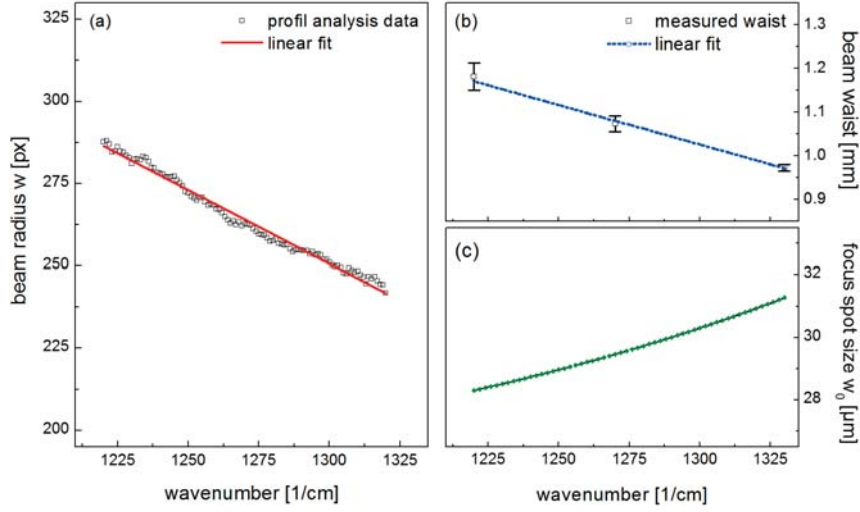


**Figure 5.6:** (a) Beam radius values gained from refractometer measurement without sample. (b) Measured beam waists. A linear fit of the data is used for calculation of the focus spot size. (c) Calculated values for the focus spot size.

$$q_2 = \frac{A \cdot q_1 + B}{C \cdot q_1 + D} \quad (5.8)$$

The real parameters  $A$ ,  $B$ ,  $C$ ,  $D$  are written as a  $2 \times 2$  matrix. Each optical element of the system is described by such a matrix. Analogous to the Jones and Müller formalism the ABCD matrix of the system is calculated by multiplying the matrices for each optical element. Here the matrices  $\underline{p}(d)$  for the free space propagation of a distance  $d$  and  $\underline{l}(f)$  for a thin lens with focal length  $f$  are needed [81]:

$$\underline{p}(d) = \begin{bmatrix} 1 & d \\ 0 & 1 \end{bmatrix} \quad \text{and} \quad \underline{l}(f) = \begin{bmatrix} 1 & 0 \\ -1/f & 1 \end{bmatrix} \quad (5.9)$$

The focus spot size  $w_0$  is calculated using the measured values for  $w$  and  $R = 0$  (since it is the beam waist) and the ABCD-matrix  $\underline{M}$  is then given by:

$$\underline{M} = \underline{p}(d_3) \cdot \underline{l}(f_3) \cdot \underline{p}(d_2) \cdot \underline{l}(f_2) \cdot \underline{p}(d_1) \cdot \underline{l}(f_1) \cdot \underline{p}(d_0) \quad (5.10)$$

were  $d_0 = 500$  mm is the distance between the laser output aperture and the first spherical mirror SM1,  $d_1 = f_1 + f_2$  is the distance between SM1 and SM2,  $d_2 = f_2$  is the distance from SM2 to PM1, and finally  $d_3 = f_3$  is the distance from the parabolic mirror PM1 to the entrance surface of the ZnSe prism (see Fig. 5.1). The results of the calculation are shown in Fig. 5.6c. Also important for the evaluation is the index of refraction  $n_p$  of the ZnSe-prism, which is determined with the corresponding Sellmeier equation [15]:

$$n_p^2 = 1 + \frac{4.2980149\lambda^2}{\lambda^2 - 0.1920630^2} + \frac{0.62776557\lambda^2}{\lambda^2 - 0.37878260^2} + \frac{2.8955633\lambda^2}{\lambda^2 - 46.994595^2} \quad (5.11)$$

The results from the Gaussian beam optics model are shown in Fig. 5.7, where they are compared to conventional FTIR-measurements. The FTIR values for the real part of the refractive index  $n_l$  have been derived from absorbance measurements using a Kramers-Kronig transformation. For the refractometer data neat DCM was used, whereas a 3M solution of DCM in deuterated chloroform ( $\text{CDCl}_3$ ) was used for the FTIR spectra. It is seen that the dispersion and absorption line profiles qualitatively agree for both measurements, but the absolute values differ. This is in part because any distortion of the beam (partly induced by the diffuser) will affect the quality of the fit. Therefore the RMS error is calculated and shown for comparison in Fig. 5.7. The error is computed from the RMS value of the fit residuals weighted by the peak height. Overall this error is  $< 10\%$ . For  $\nu < 1260 \text{ cm}^{-1}$  the deviation is larger because here the camera pixel noise increases as the intensity incident on the camera becomes small. The image noise on the camera is similarly analyzed and

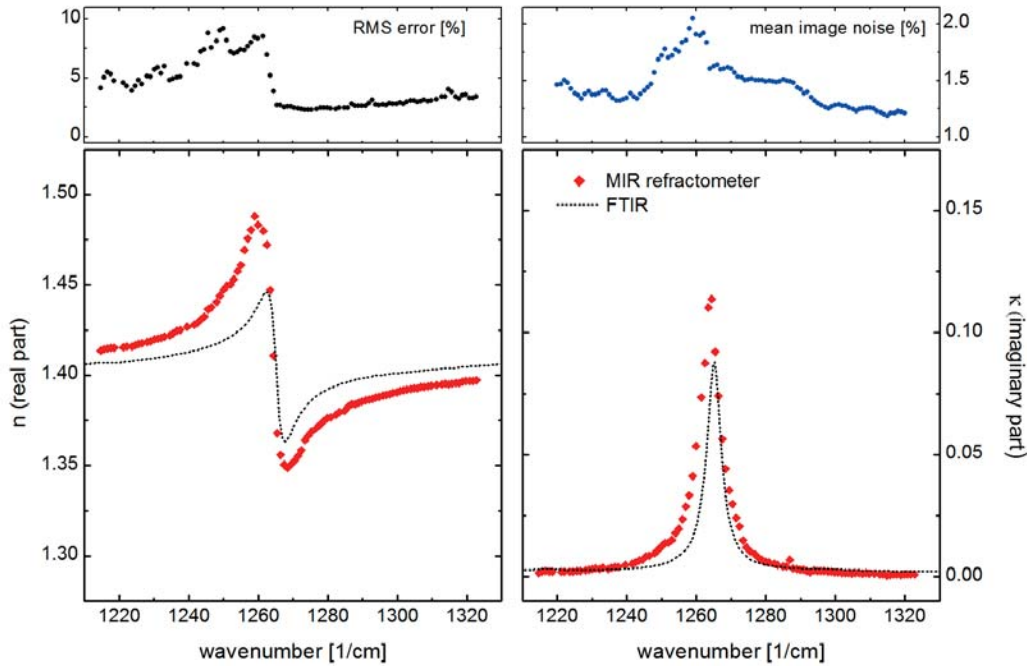


**Figure 5.7:** Results of MIR refractometer measurements of dichloromethane (DCM). Gaussian beam profiles in the fits are compared to direct FTIR absorption measurements. In the FTIR data  $n$  has been determined from the corresponding  $\kappa$  values using a Kramers-Kronig transformation. The RMS error and the mean image noise are plotted in the upper panels (see text for details). (taken from [P5])

shown in Fig. 5.7. It is calculated by first smoothing the raw data of the beam profile with a moving average filter. Afterwards the RMS deviation between smoothed and raw data is computed and weighted by the peak value.

In the present setup the refractometer requires an expensive imaging setup and is limited by any distortions of the beam profile. Improvements in sensitivity and ease of implementation could be provided by position sensitive detectors (PSD) in the MIR, which are however not yet commercially available. Sensitive position detection schemes using PSDs are presented in chapter 3 (chiral refractometer) for the visible spectral region and could also be implemented here. Together with a wedge-shaped sample cell and an appropriate polarization modulation (as shown in chapter 3) this would allow the detection of the vibrational circular birefringence (VCB)  $\delta n$  via measurements of the optical activity induced beam deflection and splitting in the MIR. The corresponding VCD spectrum of the optically active substance could then be revealed by a Kramers-Kronig transform. Therefore, the VCD analysis of optically active substances would be possible without the need for direct intensity measurements.





# 6

## Chiral Scattering and Colloidal Molecules

This chapter is based on [P6]. It has been shown, that the interaction potential of spherical colloids can be tuned to mimic the potentials that drive certain atomic and ionic processes. It allows a direct visualization of solid state phenomena difficult to observe at the atomic level, such as crystallization, melting, and dislocation dynamics [82–86]. In analogy to “colloidal atoms” [87] the name “colloidal molecules” [88] has been proposed to describe small non-spherical clusters of particles representing molecules and their interactions at the mesoscale.

In this context the colloidal counterparts of chiral molecules are particularly interesting, since they could serve as mesoscopic model systems that may permit the visualization of molecular phenomena that are otherwise difficult to observe. These include several useful effects like the propeller effect, which have not been demonstrated on the molecular scale due to the weak symmetry-breaking of chiral molecules. Because surface minimization generally favors the growth of symmetric particles it is, however, difficult to synthesize chiral colloids. So available synthetic approaches generally yield particles that are either spherical or highly symmetric [89–93]. Only a few methods have been published that can produce enantiopure chiral colloids [94,95] but none of them being able to generate large numbers of colloids with programmable shape, chirality and material composition.

In this chapter it is shown how glancing angle physical vapor deposition (GLAD) can be used for the batch-production of large numbers of helical colloids with defined handedness and shape. Moreover, the differential scattering of circular polarized light is shown to be a useful diagnostic tool for the characterization of the corresponding colloidal solutions and to observe the mirror-asymmetric nature of colloids with different handedness. The measurement results are compared to theoretical predictions based on a simple analytical model. Finally the chiral colloids are used for the experimental demonstration of the

propeller effect, first predicted in 1978 by Baranova and Zel'dovich [96]. It is used for the separation of a racemic mixture of colloids with opposite handedness. The work has been performed at the Max-Planck-Institute for Intelligent Systems (Stuttgart, Germany) and has been published in [P6]. The main contribution of the author (Marcel Pfeifer, M.P.) was the calculation and measurement of the Circular Differential Scattering (CDSI).

## 6.1 Synthesis of chiral colloids

Many strategies like geometrical confinement (e.g. by microwells or emulsion droplets), controlled surface nucleation, phase separation approaches or cluster-formation through the application of external fields or the inclusion of magnetic patches have been developed to produce colloidal molecules [89–93]. But since colloids, contrary to atoms, generally lack directional interaction most of the approaches tend to yield mixtures of different clusters with high symmetry. Glancing angle deposition (GLAD) has been used to grow a large number of colloids with defined shape, chirality, and in-built dipole functionality. GLAD as a physical vapor deposition (PVD) technique can grow  $\sim \mu\text{m}$ -sized particles with a variety of shapes. Moreover it allows the inclusion of a number of different materials and thus functionalities such as magnetic properties or surface chemistries, in a one-step process [97,98]. In Fig. 6.1 the used fabrication principle is shown.

At first a silicon wafer is coated with a monolayer of silica seed particles using vertical colloidal deposition. The monodisperse silica particles with a diameter of about 300 – 400 nm were synthesized by Debora Schamel (D.S.) according to a modified Stoeber-Method [99] and surface-treated with allyltrimethoxysilane [100]. A dispersion of these particles in chloroform was dropped onto the surface of a Langmuir-Blodgett trough. A monolayer was

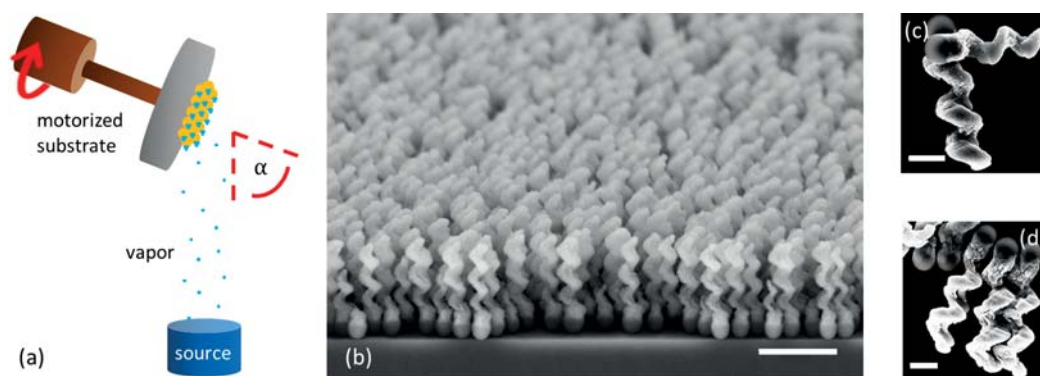


**Figure 6.1:** (a) Schematic of the GLAD technique as described in the text. (b) SEM image of a wafer containing helices representative of those used in this work. (c) Left- and (d) right-handed chiral particles released in solution. Scale bar in (b) is  $2 \mu\text{m}$ , (c) and (d) are  $0.5 \mu\text{m}$ . (taken from [P6]).

transferred onto a 2"-wafer at a surface pressure of about 20 mN/m (work by D.S.). The patterned wafer is brought into the GLAD chamber, where the material to be used is heated with an electron beam and deposited onto the silica microspheres at a glancing angle of  $\alpha \approx 85^\circ$  (Fig. 6.1a). For the growth of helices an azimuthal rotation of the wafer during the deposition process is implemented. The chirality and pitch of the particles can be easily tuned by adjusting the rotation direction and speed at a given vapor flux, i.e. the faster the rotation the smaller the pitch. For magnetic properties, as used for the experimental verification of the propeller effect (Sec. 6.3), the deposition of nickel is used which is ferromagnetic already as a thin film and relatively stable in aqueous solutions. The number of helices produced in one batch is of the order of  $10^{10}$  on a 2"-wafer. The particles are released from the wafer into solution by sonicating a wafer piece. The GLAD growth has been undertaken by Dr. John Gibbs and D.S..

## 6.2 Optical characterization

This section is work by the present author (M.P.) and has only in part been published in [P6]. To characterize the handedness and geometrical shape of the colloidal solutions of glass helices the differential scattering of circularly polarized light has been used. This effect was first demonstrated experimentally in 1982 by Bustamante et al. who measured the scattering of helical octopus sperm heads [101]. They showed that the chirality of colloidal scatterers clearly manifests itself in circular differential scattering spectra even in the absence of chromophores [101, 102]. Moreover, the differential scattering reveals information about chiral structural elements of the colloids on the order of the wavelength used in the experiment. Due to this sensitivity of the circular differential scattering intensity (CDSI) to the chiral geometry [21, 103, 104] it can serve as a diagnostic to ensure that colloidal solutions obtained from helices with opposite handedness grown on different wafers are enantiomers. Indeed, since the octopus sperm head used in the previous study is only available in one helicity and geometry, CDSI has previously not been validated for pairs of enantiomers [105–107].

### 6.2.1 Calculation of circular differential scattering (CDSI)

All calculations are based on the analytical model first proposed by Bustamante et al. [21]. Here a small error that appears in their final expression for the circular differential scattering intensity (in Ref. [21]) has been corrected. The calculations are also extended to consider helical scatterers of finite thickness. Results from both, the corrected single helical scatterer (based on [21]) as well as the thick helix are shown.

As shown in Sec. 2.2.3 is the circular differential scattering intensity (CDSI) defined as [101]:

$$CDSI = \frac{I_r(\theta) - I_l(\theta)}{I_r(\theta) + I_l(\theta)} = \frac{\Delta I}{TSI} \quad (6.1)$$

where  $I_{l,r}(\theta)$  are the intensities of the scattered light propagating in the direction defined by the angle  $\theta$  for left or right circularly polarized light incident upon the sample and  $TSI$  the total scattered intensity. In general, scattering processes are modeled by considering a finite object to consist of a set of point polarizabilities arranged in space, where each is represented by a tensor  $\underline{\alpha}_j$  and emits a wave according to Eq. 2.46. The total scattered wave  $\mathbf{E}^s$  is the sum over all the emitted fields. At a distance  $r'$  to the scattering volume it is then given by [21]:

$$\mathbf{E}^s(r') = \frac{k^2}{r'} e^{-ikr'} (1 - \hat{\mathbf{k}}\hat{\mathbf{k}}) \cdot \sum_j e^{i\Delta\mathbf{k}\cdot\mathbf{r}_j} \underline{\alpha}_j \cdot \mathbf{E}^0 \quad (6.2)$$

where  $\mathbf{E}^0$  and  $\mathbf{k}_0$  are the electric field amplitude and wave vector of the incident field and  $k = 2\pi/\lambda$ . The wave vector of the scattered radiation is  $\mathbf{k} = (2\pi/\lambda)\hat{\mathbf{k}}$  and  $\Delta\mathbf{k} = \mathbf{k} - \mathbf{k}_0$ . The tensor for each point polarizability is written in terms of its components along a single principal axis  $\hat{\mathbf{t}}_j$  [21]:

$$\underline{\alpha}_j = \alpha_j \hat{\mathbf{t}}_j \hat{\mathbf{t}}_j \quad (6.3)$$

Using Eq. 6.3 together with Eq. 2.31 for a left- or right-circularly polarized incident plane wave,  $\Delta I$  and  $TSI$  can be calculated from Eq. 6.2. For an isotropic suspension of colloids or macromolecules, both the difference  $\Delta I$  and the sum  $TSI$  have to be averaged over all orientations of the scatterer. This is possible by expressing all quantities in Eq. 6.2 in terms of a well-defined space-fixed and a scatterer-fixed coordinate system [21]. The isotropic differential scattering intensity  $\langle \Delta I \rangle$  for a scatterer of arbitrary shape is then [21, 103]:

$$\begin{aligned} \langle \Delta I \rangle = & \frac{8\pi^4}{\lambda^4 r'^2} \sum_{ij} \alpha_i^* \alpha_j (\hat{\mathbf{t}}_j \times \hat{\mathbf{t}}_i) \cdot \hat{\mathbf{R}}_{ij} \left[ (\hat{\mathbf{t}}_i \cdot \hat{\mathbf{t}}_j) \left( \frac{j_2(q)}{q} - j_1(q) \right) \right. \\ & \left. - (\hat{\mathbf{t}}_i \cdot \hat{\mathbf{R}}_{ij}) (\hat{\mathbf{t}}_j \cdot \hat{\mathbf{R}}_{ij}) \left( \frac{5j_2(q)}{q} - j_1(q) \right) \right] \left[ \sin \frac{\theta}{2} + \sin^3 \frac{\theta}{2} \right] \end{aligned} \quad (6.4)$$

where  $\mathbf{R}_{ij} = |\mathbf{r}_j - \mathbf{r}_i| \hat{\mathbf{R}}_{ij}$  is the distance vector between the polarizabilities  $\alpha_i$  and  $\alpha_j$  with principal axis  $\hat{\mathbf{t}}_i$  and  $\hat{\mathbf{t}}_j$ . The functions  $j_1$  and  $j_2$  are spherical Bessel functions of the first kind of, respectively, first and second order. Their argument is given by [21]:

$$q = \left( \frac{4\pi R_{ij}}{\lambda} \right) \sin \frac{\theta}{2}$$

Similarly, an analogous expression for the total scattering intensity TSI can be derived [21].

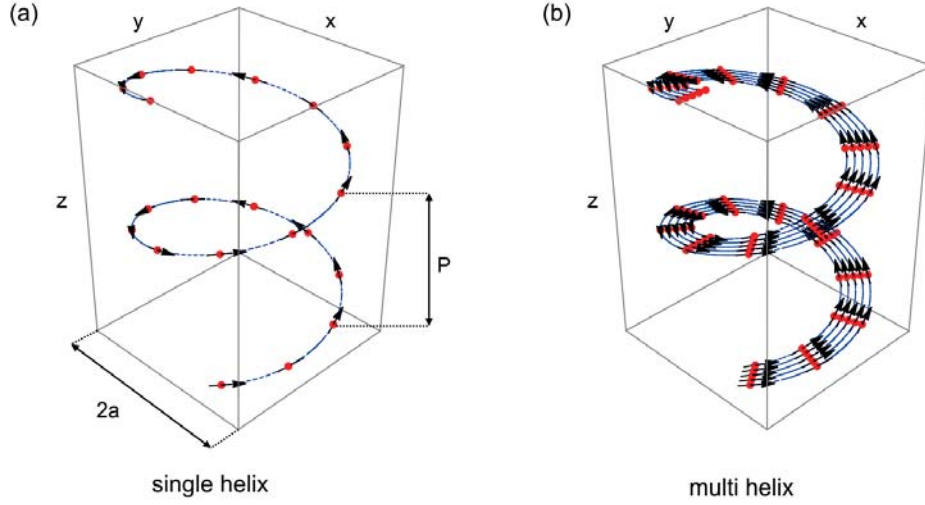


**Figure 6.2:** (a) Scheme of a single helical scatterer with pitch  $P$  and radius  $a$  made up of uniaxial point polarizabilities (red dots) evenly spaced. Their principal axes are oriented tangential to the helix (black arrows). (b) A set of concentric helices with the same pitch but increasing radius is used to describe a helical scatterer of finite thickness [P6].

Even only achiral dipole polarizabilities  $\underline{\alpha}$  have been considered, circular differential scattering can be obtained if these polarizabilities are arranged in a chiral geometry. A number of simplifications can be made for the special case of a helical scatterer. The geometry can be expressed in terms of the radius  $a$  and pitch  $P$  and the uniaxial point polarizabilities are supposed to be evenly spaced along the helix with their principal director aligned tangential to it (Fig. 6.2a). We can then write  $\mathbf{r}_i$  and  $\hat{\mathbf{t}}_i$  as a function of  $a$  and  $P$  [21]:

$$\mathbf{r}_i = a \cos(i\tau_0)\hat{\mathbf{e}}_x + a \sin(i\tau_0)\hat{\mathbf{e}}_y + i\frac{P\tau_0}{2\pi}\hat{\mathbf{e}}_z \quad (6.5a)$$

$$\hat{\mathbf{t}}_i = -\frac{a}{M} \sin(i\tau_0)\hat{\mathbf{e}}_x + \frac{a}{M} \cos(i\tau_0)\hat{\mathbf{e}}_y + \frac{P}{2\pi M}\hat{\mathbf{e}}_z \quad (6.5b)$$

$$\text{with } M = \sqrt{a^2 + \frac{P^2}{4\pi^2}}$$

here  $\tau_0$  is the angular distance between subsequent polarizabilities  $i$  and  $i + 1$  in radians, and  $\hat{\mathbf{e}}_x$ ,  $\hat{\mathbf{e}}_y$ ,  $\hat{\mathbf{e}}_z$  are the unit vectors along the scatterer fixed coordinate system. Using Eqs. 6.5 and  $\tau_{ij} = (j - i)\tau_0$  in Eq. 6.4 we can write:

$$\begin{aligned} \langle \Delta I \rangle_h = & \frac{2\pi^3 a^2 P}{M^4 \lambda^4 r^2} \sum_{ij} \frac{\alpha_i^* \alpha_j}{\sqrt{G_{ij}}} \left( 4 \sin^2 \frac{\tau_{ij}}{2} - \tau_{ij} \sin \tau_{ij} \right) \left[ \left( a^2 \cos \tau_{ij} + \frac{P^2}{4\pi^2} \right) \left( \frac{j_2(q)}{q} - j_1(q) \right) \right. \\ & \left. - \frac{1}{G_{ij}} \left( a^2 \sin \tau_{ij} + \frac{P^2}{4\pi^2} \tau_{ij} \right)^2 \left( \frac{5j_2(q)}{q} - j_1(q) \right) \right] \left( \sin \frac{\theta}{2} + \sin^3 \frac{\theta}{2} \right) \quad (6.6) \end{aligned}$$

with  $G_{ij} = |\mathbf{R}_{ij}|^2 = 4a^2 \sin^2(\tau_{ij}/2) + (P\tau_{ij}/2\pi)^2$ . In the prefactor of Eq. 6.6  $G_{ij}$  has been replaced by  $\sqrt{G_{ij}}$  and  $\alpha_i^* \alpha_j$  appears here (it was missing in the equation given in [21]). Due to the helical symmetry we can replace the double summation by  $\sum_{k=1}^{N-1} (N-k)$ , where  $N$  is the total number of polarizabilities. This gives the following expression for the differential scattering intensity of a thin helix:

$$\begin{aligned} \langle \Delta I \rangle_h = & \frac{2\pi^3 a^2 P}{M^4 \lambda^4 r'^2} \sum_{k=1}^{N-1} \frac{(N-k) |\alpha_k|}{\sqrt{G_k}} \left( 4 \sin^2 \frac{k\tau_0}{2} - k\tau_0 \sin k\tau_0 \right) \\ & \left[ \left( a^2 \cos k\tau_0 + \frac{P^2}{4\pi^2} \right) \left( \frac{j_2(q)}{q} - j_1(q) \right) \right. \\ & \left. - \frac{1}{G_k} \left( a^2 \sin k\tau_0 + \frac{P^2}{4\pi^2} k\tau_0 \right)^2 \left( \frac{5j_2(q)}{q} - j_1(q) \right) \right] \left( \sin \frac{\theta}{2} + \sin^3 \frac{\theta}{2} \right) \end{aligned} \quad (6.7)$$

In order to model helical colloids with a finite thickness, i.e. an inner and outer radius ( $a_{in}$ ,  $a_{out}$ ), we consider a stack of  $n_h$  concentric “thin” helices with the same pitch but increasing radius ( $a_{in} \leq a \leq a_{out}$ ) (Fig. 6.2b). The CDSI value for the colloid is either calculated by independently simulating each thin helix using Eq. 6.7, or by summing a helix stack. For the latter approach we have to slightly modify Eq. 6.7. First the radius is defined as a function of the index  $i$ , the number of turns  $T$ , the number of polarizabilities per turn  $n_p$  and the number of helices  $n_h$ :

$$a(i) = a_{in} + \left\lfloor \frac{i}{T n_p} \right\rfloor \left( \frac{a_{out} - a_{in}}{n_h} \right) \quad (6.8)$$

Here  $\lfloor x \rfloor$  is the floor function giving the greatest integer less than or equal to  $x$ . Next we use  $a(i)$  and Eq. 6.5 to redefine the following parameters:

$$\mathbf{r}_i = a(i) \cos(i\tau_0) \hat{\mathbf{e}}_x + a(i) \sin(i\tau_0) \hat{\mathbf{e}}_y + c_i \frac{P\tau_0}{2\pi} \hat{\mathbf{e}}_z \quad (6.9a)$$

$$\hat{\mathbf{t}}_i = -\frac{a(i)}{M_i} \sin(i\tau_0) \hat{\mathbf{e}}_x + \frac{a(i)}{M_i} \cos(i\tau_0) \hat{\mathbf{e}}_y + \frac{P}{2\pi M_i} \hat{\mathbf{e}}_z \quad (6.9b)$$

$$M_i = \sqrt{a(i)^2 + \frac{P^2}{4\pi^2}}, \quad c_{ij} = (c_j - c_i)\tau_0, \quad c_i = i - \left\lfloor \frac{i}{T n_p} \right\rfloor T n_p \quad (6.9c)$$

$$G_{ij} = a(i)^2 + a(j)^2 - 2a(i)a(j) \cos \tau_{ij} + \left( \frac{P c_{ij}}{2\pi} \right)^2 \quad (6.9d)$$

Finally, using the equations above we can express the spatially averaged differential intensity for the multi-helix stack as:

$$\langle \Delta I \rangle_{mh} = \frac{2\pi^3 P}{\lambda^4 r'^2} \sum_{ij} \frac{\alpha_i^* \alpha_j}{\sqrt{G_{ij}} M_i^2 M_j^2} \left( a(i)^2 + a(j)^2 - a(i)a(j) (2 \cos \tau_{ij} + c_{ij} \sin \tau_{ij}) \right) \dots$$

$$\begin{aligned} & \dots \left[ \left( a(i)a(j) \cos \tau_{ij} + \frac{P^2}{4\pi^2} \right) \left( \frac{j_2(q)}{q} - j_1(q) \right) \right. \\ & \left. - \frac{1}{G_{ij}} \left( a(i)a(j) \sin \tau_{ij} + \frac{P^2 c_{ij}}{4\pi^2} \right)^2 \left( \frac{5j_2(q)}{q} - j_1(q) \right) \right] \left( \sin \frac{\theta}{2} + \sin^3 \frac{\theta}{2} \right) \end{aligned} \quad (6.10)$$

In what follows CDSI intensities are computed for both models and a variety of helix geometries.

### Convergence criteria

For the subsequent calculations the vacuum wavelength and the refractive index of the solvent are  $\lambda_0 = 532$  nm and  $n_{sl} = 1.33$  (water), respectively, which gives a wavelength inside the solvent of  $\lambda_1 = 400$  nm. Furthermore we only consider helical scatterers made out one material, so we can write  $\alpha_i = \alpha$  for all  $i$  and  $\alpha_i^* \alpha_j = \alpha^2$ . Because  $\alpha^2$ , which is proportional to the refractive index of the used material, is then simply a scaling factor for  $\langle \Delta I \rangle$  (Eq. 6.7 and 6.10), we can set  $\alpha^2 = 1$  in this qualitative analysis for simplicity.

At first  $\langle \Delta I \rangle$  is calculated for a single helix while increasing the number of polarizabilities per turn  $n_p$ . The other parameters pitch, radius and number of turns are fixed and  $P = 250$  nm,  $a = 150$  nm and  $T = 2$ , respectively. The results for five different values of  $n_p$  using Eq. 6.7 are shown in Fig. 6.3a. As can be seen the shape of the  $\langle \Delta I \rangle$  signals is unchanged, only the absolute values scale quadratically with  $n_p$ . This is also shown by the ratios of the signals for  $n_p = 10$ , shown in Fig. 6.3b, and the corresponding mean values in Fig. 6.4a. Therefore a number of  $n_p = 20$  polarizabilities per turn is sufficient for a qualitative analysis. Here the lateral distance between adjacent polarizabilities is approxi-

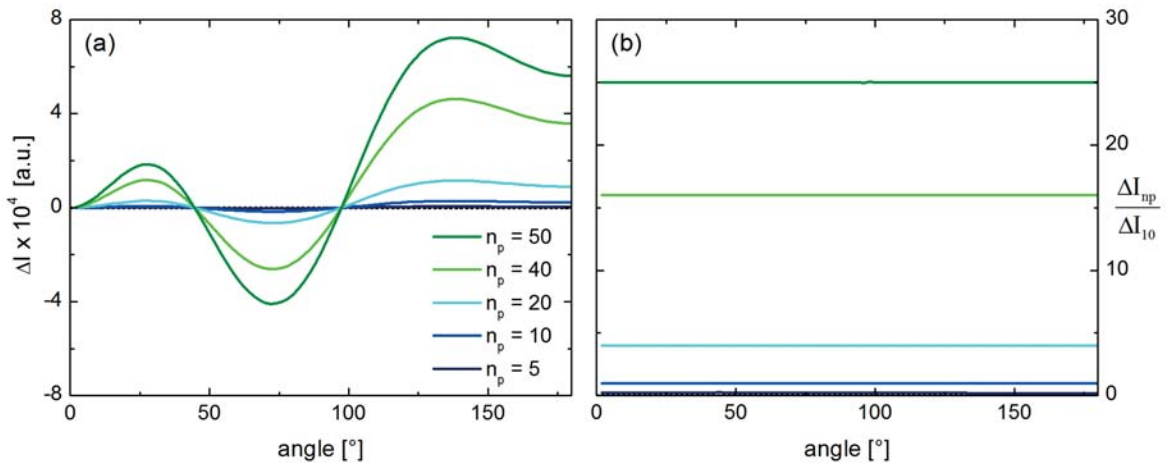


**Figure 6.3:** Variation of the number of polarizabilities per turn  $n_p$ . Shown are the (a)  $\Delta I_{n_p}$  signals and (b) the ratios  $\Delta I_{n_p}/\Delta I_{10}$ .

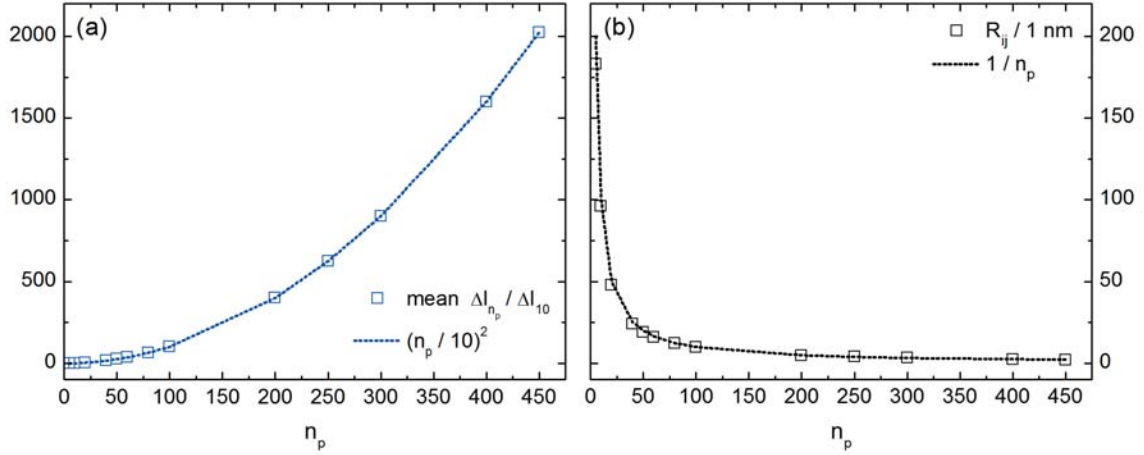


**Figure 6.4:** (a) Mean values of the ratios  $\Delta I_{np}/\Delta I_{10}$ , which scale quadratically with  $n_p$ . (b) Lateral distance for adjacent polarizabilities for different values of  $n_p$ .

mately  $R_{i,i+1} = 50$  nm (Fig. 6.4b). For a multi-helix stack the number of thin helices  $n_h$  varies. We examined a multi-helix with the following parameters:  $P = 250$  nm,  $T = 2$ ,  $a_{in} = 150$  nm and  $a_{out} = 175$  nm. We set the number of polarizabilities per turn to  $n_p = 20$  and calculate the multi helix signal  $\langle \Delta I \rangle_{mh}$  (Eq. 6.10). The results are shown in Fig. 6.5a together with the ratio  $\Delta I_{nh}/\Delta I_2$  of the signals and the signal for  $n_h = 2$  (Fig. 6.5b). The differential intensity for a multi-helix stack scales with the number of thin helices  $n_h$ . Moreover, a slight change in the root positions can be observed, as seen in the increasing ‘spikes’ in the ratio signals (Fig. 6.5b) and also in Fig. 6.6. Here the values  $\theta_{zero}$  for the two roots are plotted against  $n_h$ . For values of  $n_h \geq 5$  the changes in  $\theta_{zero}$  are small ( $\leq 0.05^\circ$ ). So for the multi-helix stack five thin helices are sufficient for calculations.

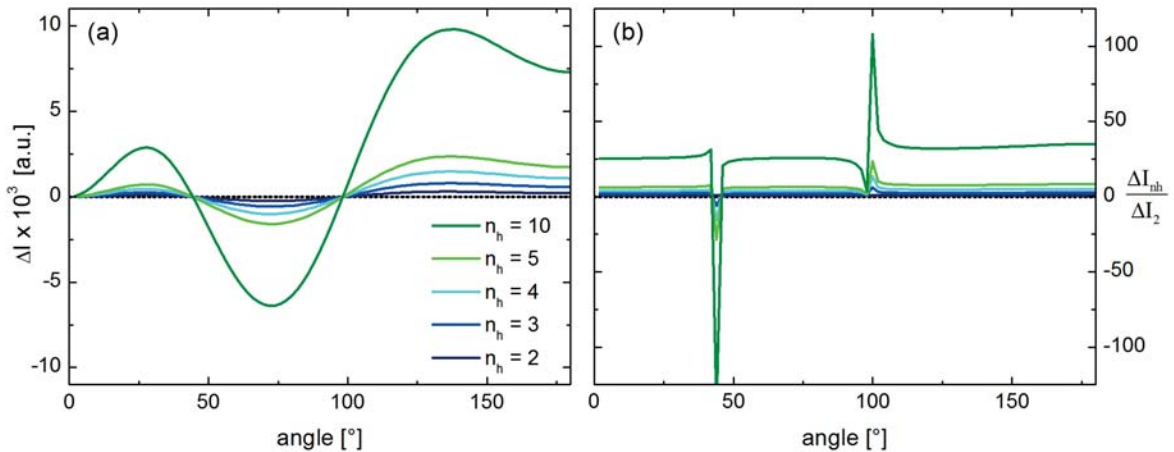


**Figure 6.5:** Variation of the number of thin helix  $n_h$  composing a multi-helix stack. (a) The values for  $\Delta I_{nh}$  calculated with Eq. 6.10. (b) Ratio  $\Delta I_{nh}/\Delta I_2$  for different values of  $n_h$ .

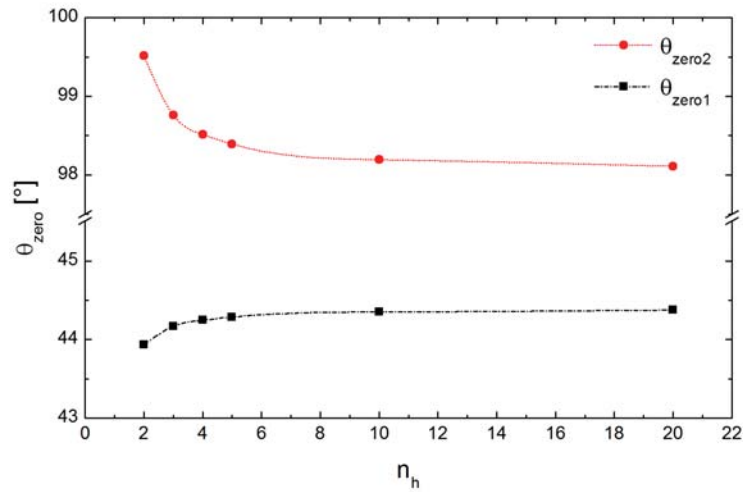


**Figure 6.6:** Position of the roots of the  $\Delta I_{np}$  signal for different  $n_h$ . For  $n_h \geq 5$   $\theta_{zero}$  changes by less than  $\leq 0.05^\circ$ .

### Variation of geometrical parameters

Next we will have a look how the  $\langle \Delta I \rangle$  signals change with respect to variations of geometrical parameters of the helix. Here only a thin single helix is considered, since the behavior should be the same for  $\langle \Delta I \rangle_{mh}$ . At first the number of turns  $T$  is changed for a helix with  $P = 250$  nm,  $a = 150$  nm and  $n_p = 20$ . Figure 6.7 shows the results for  $\langle \Delta I \rangle$  along with the ratio  $\Delta I_T / \Delta I_2$ . Again the absolute value of the differential scattering scales with the number of turns while the shape of the signal is mainly unchanged except for a small shift of the roots (see Fig. 6.7b).

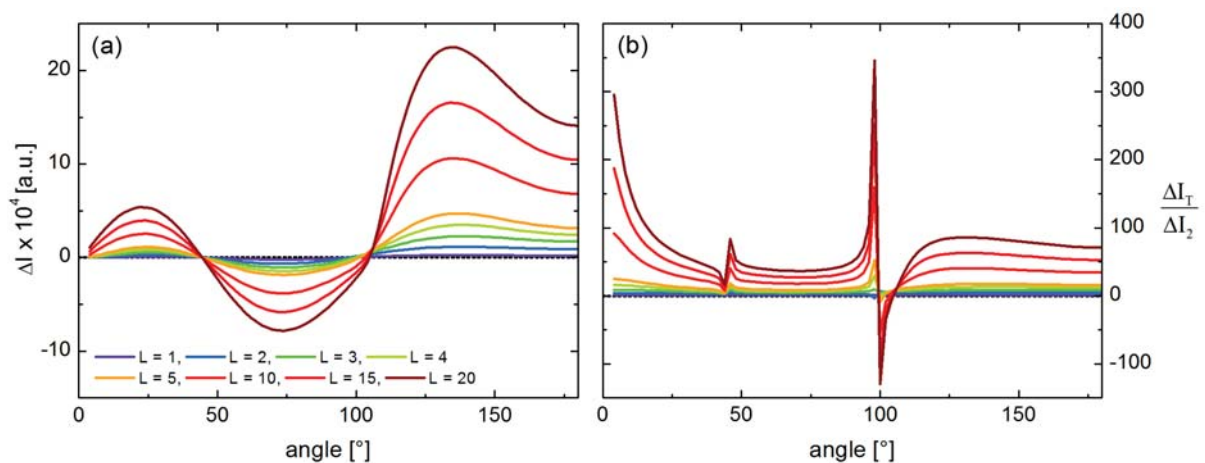


**Figure 6.7:** (a) Differential scattering intensity  $\Delta I$  for single helices with increasing number of turns  $T$ . (b) Ratio of the signals with  $\Delta I_2$ .

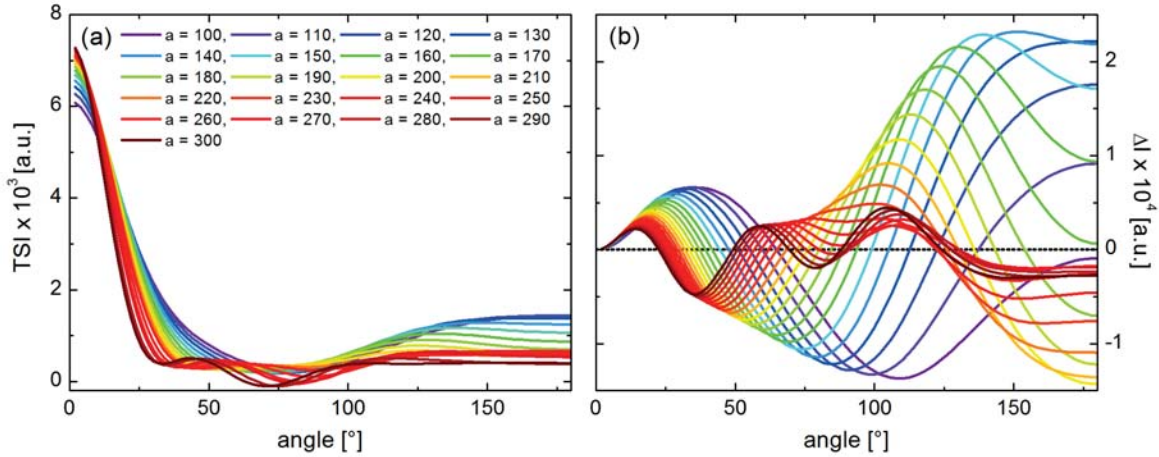


**Figure 6.8:** (a) Total and (b) differential scattering intensity for single helices with  $P = 250$  nm,  $T = 3$  and increasing radius  $a$ .

In contrast, the differential scattering intensity is very sensitive to small changes of the radius  $a$  or the pitch  $P$  of the helix. To see how  $\langle \Delta I \rangle$  varies the signals have been calculated for a helix with three turns ( $T = 3$ ), where either the radius or the pitch is increased. In Fig. 6.8 the results for both the total scattering intensity (TSI) and  $\Delta I$  are shown for helical scatterers with  $P = 250$  nm and different radius  $a$ . The TSI values have been calculated using the formula given in [21]. One can see, that the  $\Delta I$  signals change dramatically when  $a$  is increased. Especially the number of roots, and therefore the number of maxima and minima of the signal grows with an increasing radius  $a$ . This is illustrated by Fig. 6.9. Here the number and the position of the corresponding roots of the signal are given for the different values of  $a$ .

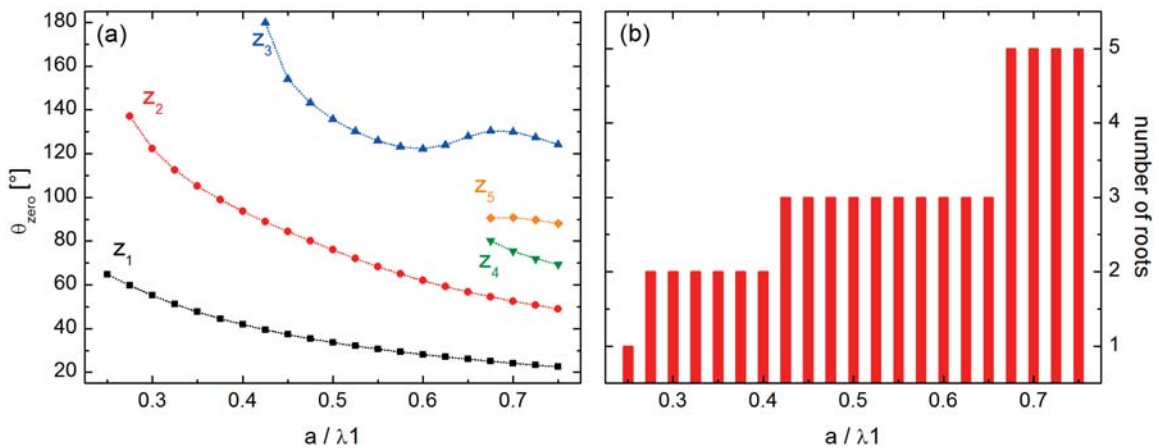


**Figure 6.9:** (a) Changing root positions  $\theta_{zero}$  of the  $\Delta I$  spectra with increasing radius  $a$  of the helix. (b) The number of roots increases with the radius  $a$  of the helix.

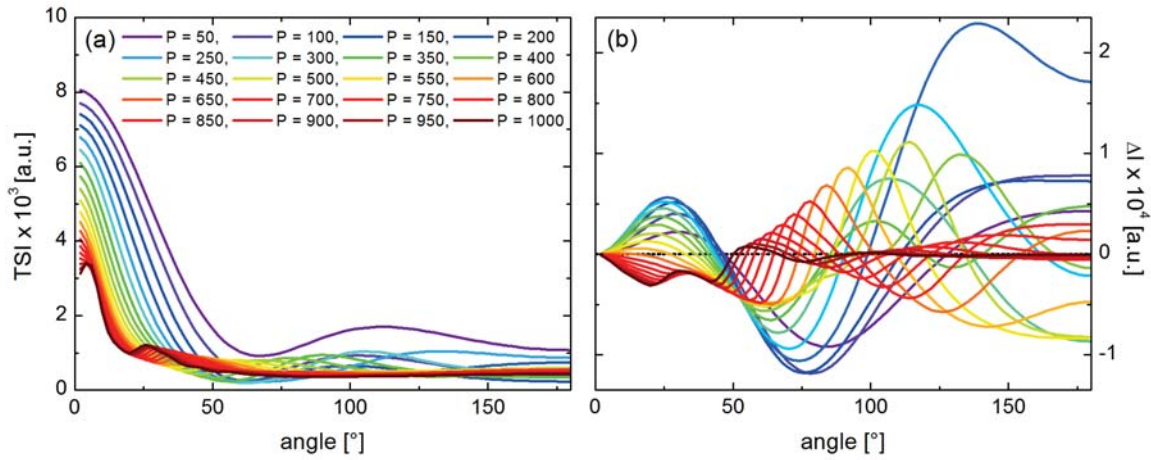


**Figure 6.10:** (a) Total and (b) differential scattering intensity for single helices with  $a = 150$  nm,  $T = 3$  and increasing pitch  $P$ .

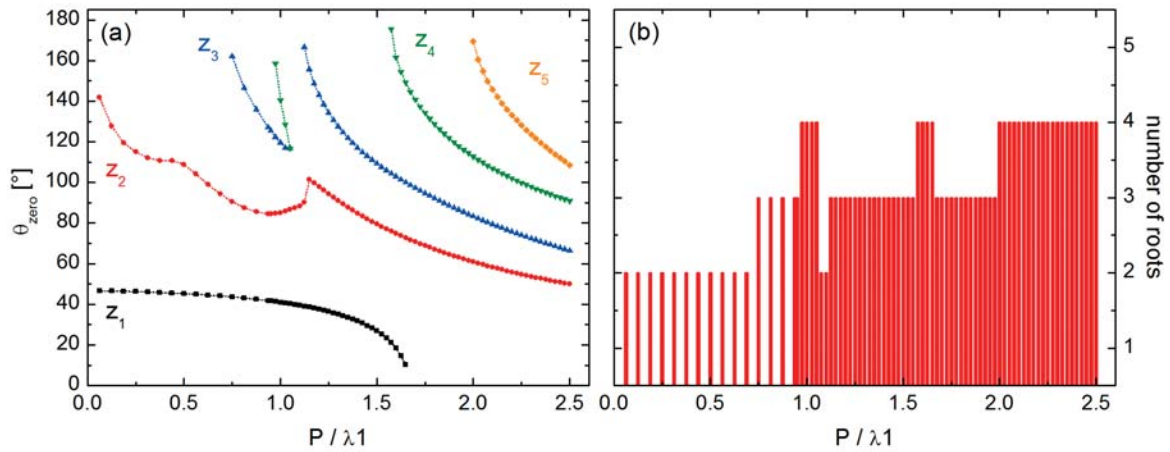


**Figure 6.11:** (a) Root positions  $\theta_{zero}$  of the  $\Delta I_{lr}$  spectra with increasing pitch  $P$  of the helix. (b) The number of roots also varies when the pitch  $P$  of the helix is changed.

An analogous response of the differential scattering intensity  $\Delta I$  to changes of the pitch  $P$  can be found. For helices with a radius of  $a = 150$  nm and three turns the  $TSI$  and  $\Delta I$  signals have been calculated while increasing the pitch. The results are shown in Fig. 6.10. Here also the number and position of the roots, and therefore of the extrema, varies for the different values of  $P$ , which is visualized in Fig. 6.11.

## Comparison of calculation methods

Finally the two simulation models for the thick helix are compared. Therefore we assumed two multi-helix stacks, one with a pitch of  $P = 250$  nm, two turns ( $T = 2$ ), and an inner and outer radius of  $a_{in} = 150$  nm and  $a_{out} = 175$  nm, respectively. Whereas for other we set  $P = 550$  nm,  $T = 3$ ,  $a_{in} = 100$  nm and  $a_{out} = 275$  nm. The stacks are composed of five thin helices, each having  $n_p = 20$  point polarizabilities per turn. The  $\Delta I$  signals are calculated by either considering each thin helix independently using Eq. 6.7 and summation of the five spectra, or by using the multi-helix approach of Eq. 6.10. Figure 6.12a and c show the results of the five thin helix, whereas in Fig. 6.12b and d the sum of these signals is depicted together with the multi helix signal. It is obvious that the multi helix signal is in both cases bigger than the sum by a factor of  $\sim 5$ , also validated by the ratios  $\Delta I_{mh}/\Sigma\Delta I_{sh}$  shown in Fig. 6.13. Here the ‘spikes’ indicate shifts of the root positions between the signals, which is

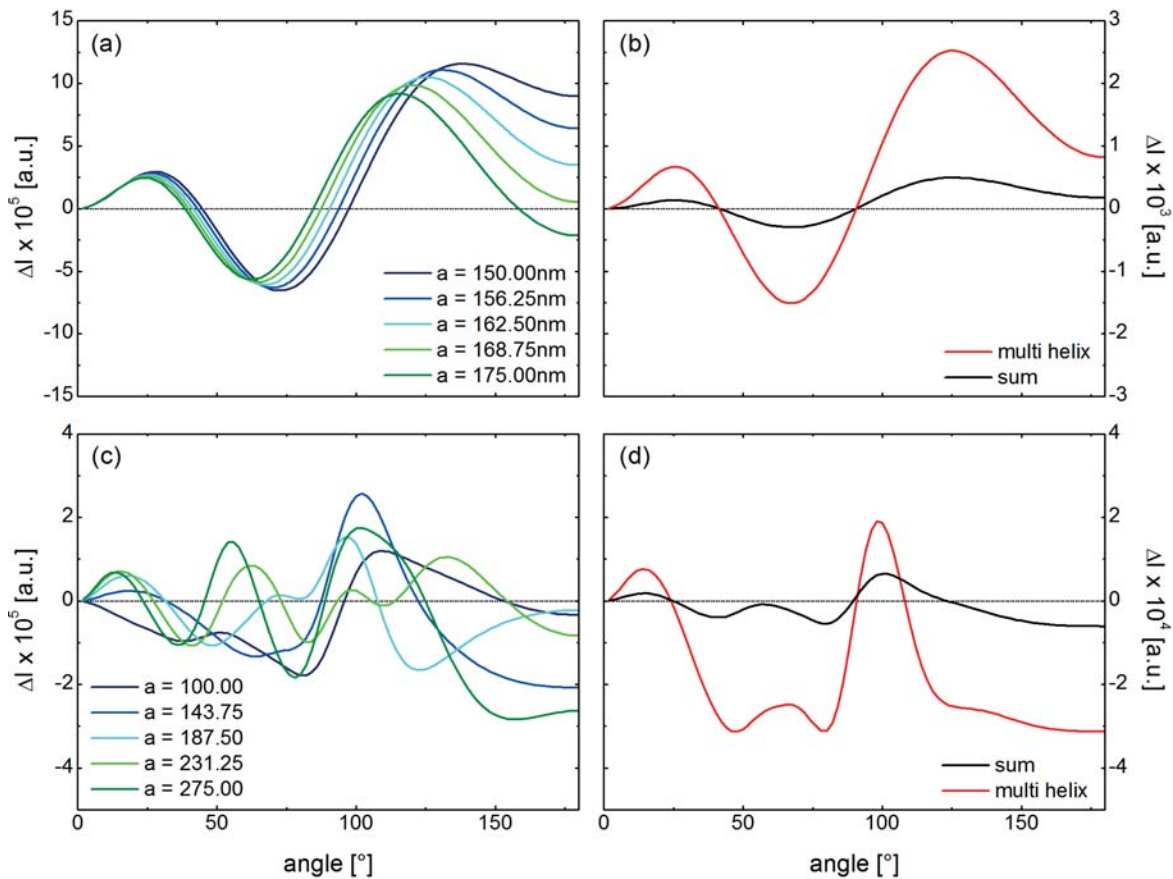


**Figure 6.12:** Comparison of two different calculation methods. Calculated spectra of  $\Delta I$  for thin helices with (a) pitch  $P = 250$  nm or (c) pitch  $P = 550$  nm and radius  $a$  using Eq. 6.7. (b) and (d) Sum of the spectra shown in (a) and (c) (black line) compared with the result obtained using the multi helix approach (Eq. 6.10).

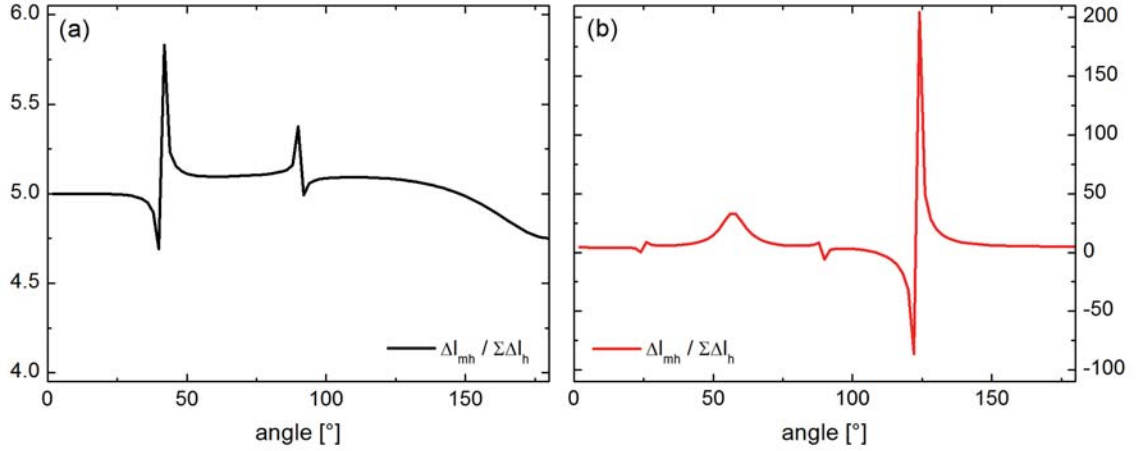


**Figure 6.13:** Ratios of the multi-helix signal  $\Delta I_{mh}$  and the sum of the single helix signals  $\Sigma \Delta I_{sh}$  for the spectra shown in (a) Fig. 6.12b and (b) Fig. 6.12d. The multi-helix signal is in both cases approximately five times bigger than the sum. The spikes also indicate a shift of the root positions, which are more pronounced for (b).

more pronounced for the thicker helix stack (Fig. 6.13b). These differences are likely due to the fact, that the multi-helix approach considers also cross-terms between polarizabilities on different thin helices inside the stack. In contrast, these interference terms are neglected in the simple summation of the thin helix spectra. Therefore, when considering helical scatterer of finite thickness, the multi-helix approach (Eq. 6.10) should be used for more accurate results.

### 6.2.2 Experimental setup

The setup used for the differential scattering experiments is shown in Fig. 6.14. A diode pumped solid state laser (DPSS) with an optical output power of  $P = 100$  mW (cw) and a wavelength of  $\lambda = 532$  nm was used as a light source. After passing an optical chopper ( $f_{chopper} = 300$  Hz) the light is first linearly polarized ( $\theta = -45^\circ$ ) and then sent to a photoelastic modulator (PEM). The PEM modulates between left- and right-circular polarization states at  $f_{PEM} \approx 50$  kHz, before the light is incident on a cylindrical scattering cell that contains the colloidal solution. The scattered light is detected using a photomultiplier tube (PMT) mounted on a precision goniometer with an angular resolution of  $< 1^\circ$ . The distance between the PMT and the center of the sample cell is  $d = 10$  cm and together with an entrance aperture of 1.5 mm of the PMT this results in an angular resolution of  $0.86^\circ$ .

The detector signal is electronically processed by two lock-in-amplifiers (LIA) locked to the modulation frequency of either the chopper or the PEM. While the PMT moves around

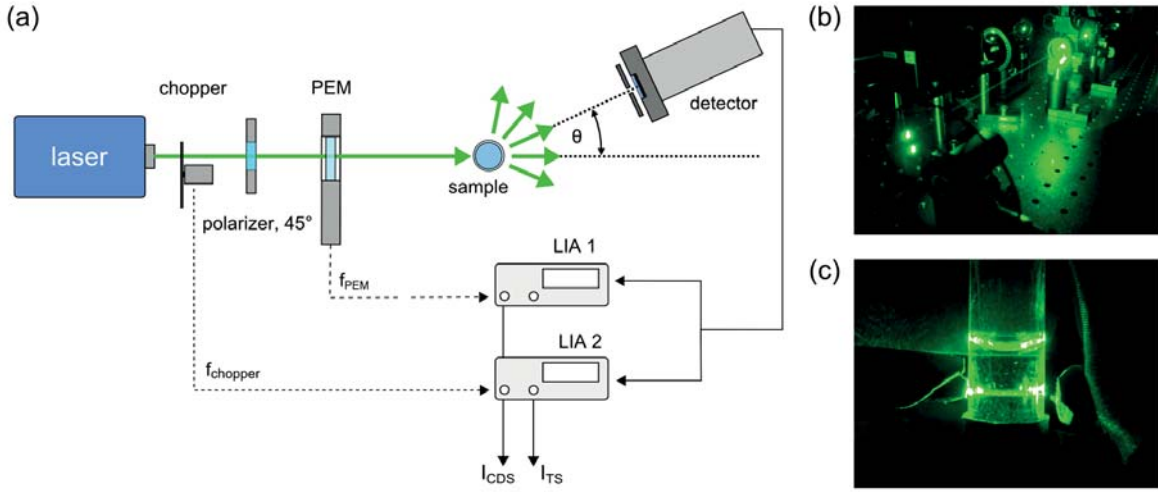


**Figure 6.14:** (a) Optical and electronic setup used for the differential scattering experiments [P6]. Pictures showing parts of the setup (b) and the illuminated cylindrical sample cell (c). Further details can be found in the text.

the sample in an arc of  $1^\circ$ -steps, 50 data points are taken and averaged for every angular position of the detector. The total scattering intensity (TSI) can be derived from the LIA locked to the chopper frequency whereas the difference in the scattering between the circular polarization states is detected by the second LIA. The circular differential scattering intensity (CDSI) as defined in Section 6.2.1 is calculated according to [12]:

$$CDSI \propto \frac{R_{PEM}}{R_{chopper} \cdot J_1(\alpha_{PEM})} \quad (6.11)$$

Here  $\alpha_{PEM} = \pi/2$  is the retardation introduced by the PEM and  $J_1(x)$  the Bessel function of the first kind.  $R_{PEM}$  and  $R_{chopper}$  are the measured amplitudes of the LIAs. To minimize artifacts arising from unwanted back-reflections and scattering, care has been taken to block the transmitted laser beam and cover all reflecting surfaces close to the sample. Scattering signals between  $10^\circ$  and  $145^\circ$  can be detected with this setup.

### 6.2.3 Measurements

Different chiral colloids have been grown by the GLAD method described in Sec. 6.1. Colloids with opposite handedness as well as different geometrical shapes have been measured and compared using the CDSI setup (Fig. 6.14). The shape and geometrical parameters were determined by analyzing scanning electron microscopy (SEM) images. An overview of these parameters can be found in Tab. 6.1, which were also used for simulation purposes.

	$2a_b$	$2a_{h,i}$	$2a_{h,o}$	$l_h$	$l_t$	$T$	$P$
left-handed helix <i>LH1</i>	$0.43 \pm 0.03$	$0.23 \pm 0.02$	$0.35 \pm 0.04$	$1.386 \pm 0.008$	$1.832 \pm 0.003$	5	$0.277 \pm 0.002$
left-handed helix <i>LH2</i>	$0.33 \pm 0.02$	$0.19 \pm 0.06$	$0.55 \pm 0.03$	$2.17 \pm 0.02$	$2.478 \pm 0.005$	4	$0.55 \pm 0.004$
left-handed helix <i>LH3</i>	$0.35 \pm 0.03$	$0.17 \pm 0.04$	$0.90 \pm 0.04$	$2.800 \pm 0.014$	$3.08 \pm 0.01$	3	$1.161 \pm 0.006$
right-handed helix <i>RH1</i>	$0.31 \pm 0.02$	$0.212 \pm 0.011$	$0.34 \pm 0.02$	$1.323 \pm 0.011$	$1.630 \pm 0.006$	5	$0.265 \pm 0.002$
achiral rod	$0.33 \pm 0.02$	-----	-----	-----	$2.314 \pm 0.004$	---	-----

**Table 6.1:** Geometrical parameters of the measured colloids also used for calculations. Shown are diameter of bead ( $2a_b$ ), inner diameter of helix ( $2a_{h,i}$ ), outer diameter of helix ( $2a_{h,o}$ ), length of helix ( $l_h$ ), total length of colloid ( $l_t$ ), number of turns ( $T$ ), and pitch of helix ( $P$ ). All values are in  $\mu\text{m}$ .

### Chiral sensitivity of CDSI

First  $TiO_2$  screws of both helicities (*LH1* and *RH1*) were grown on 300nm  $SiO_2$  beads with a helical pitch of  $P \sim 250$  nm and 4 to 5 turns. As an achiral control both solutions of the seed  $SiO_2$  beads and  $TiO_2$  rods of the same height were also measured. The latter were grown with the same GLAD-method but fast azimuthal rotation. The results from the total scattered intensity (TSI) and the circular differential scattered intensity (CDSI) measurements of the helical colloids are shown in Fig. 6.15 together with SEM images.

The TSI values for all samples decrease monotonically with increasing scattering angles for angles greater than  $20^\circ$ . The differences in the absolute values are mainly due to slight differences in the concentrations of the measured solutions. As expected, the total scattering intensity (TSI) does not differentiate between opposite helicities.

In contrast the measured CDSI signals of the two enantiomers are approximately equal in shape and opposite in sign. Small variations are due to slight differences in the geometry of the screws, as can be seen from the SEM images. The CDSI signal for the achiral rods and the spherical  $SiO_2$  beads vanish for all scattering angles, as expected. Therefore the CDSI signals are only sensitive to the chiral features of the scatterer, as proposed by Bustamante et al [21]. It can therefore distinguish between left and right-handed helices. Furthermore even small chiral structural features of the helices give rise to relatively big CDSI signals (up to  $\sim 10^{-2}$ ).

The solid lines represent theoretical calculations of the differential scattering intensity  $\langle \Delta I \rangle_{mh}$  and are based on the algorithm described in Sec. 6.2.1 using the measured geome-

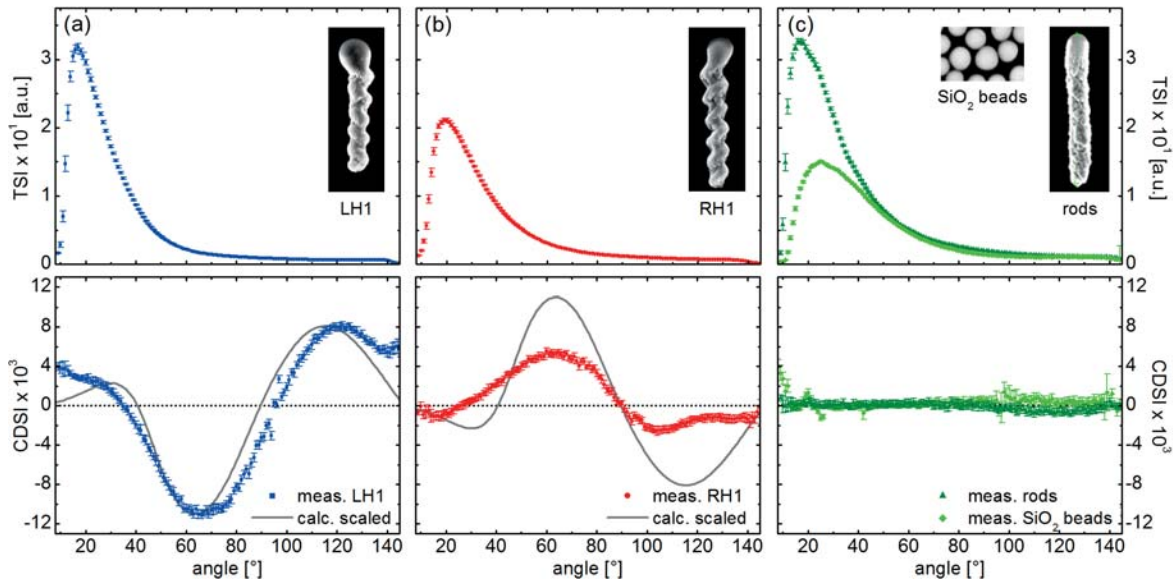


**Figure 6.15:** Total scattering intensity (first row) and the differential scattering signal of circular polarized light of (a) left- and (b) right handed helices, as well as (c) achiral rod-shaped colloids of the same size and spherical  $\text{SiO}_2$  beads. Also shown are the corresponding SEM images. The dots are experimental data, whereas the solid lines show calculation results. Each solution had a concentration of approximately 0.5  $\mu\text{M}$  [P6].

trical parameters of the colloids. The number of thin helices and polarizabilities was set to  $n_h = 5$  and  $n_p = 20$ , respectively. The calculation results are scaled for a better comparison. The calculations are in qualitative agreement with the experimental results for all samples. Discrepancies between theory and experiment for small angles can be traced back to the fact that due to experimental limitations at low angle scattering (LAS) the detector also sees some of the direct incident beam [108, 109]. But overall, the CDSI signals are sensitive to the geometry and thus serve as a diagnostic for the chirality of the solutions

We also measured a racemic mixture of the aqueous solutions of the left- and right handed helices, shown in Fig. 6.16. For this purpose 500  $\mu\text{l}$  of each solution were mixed together. As expected the CDSI signals almost vanish whereas the TSI signals do not change significantly. Moreover, the CDSI signal of the racemate is in good agreement with the mean value of the signals for both helices, which is also shown for comparison.

### Variation of geometrical parameters

Now the CDSI and TSI signals of chiral colloids with different geometrical parameters shall be compared. Therefore  $\text{TiO}_2$  screws have been grown with increasing pitch. Screws with twice ( $P \sim 500$  nm,  $LH2$ ) and fortimes ( $P \sim 1000$  nm,  $LH3$ ) the pitch of the colloids measured before were fabricated. As the SEM pictures and the measured parameters show

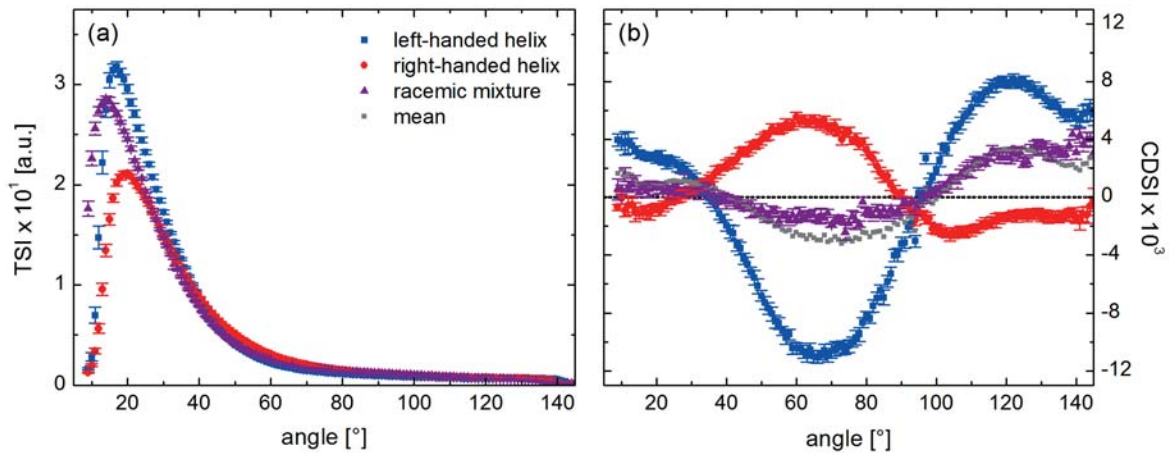


**Figure 6.16:** (a) Total scattered intensity (TSI) and (b) circular differential scattering signal (CDSI) for a racemic mixture of the left- and right handed helices. The CDSI values for the enantiolean solutions are also shown as well as the mean value of these signals (taken from [P6]).

(Fig. 6.18 and Tab. 6.1) was not only the pitch increased, but also the diameter of the screws. If the radius now exceeds the mean distance between neighboring seeds, then the helices may join during the growth process which causes aggregates in solution (Fig. 6.17). This changes the CDSI signals and complicates the interpretation. Nevertheless we successfully measured CDSI and TSI for helices with increasing pitch, as is shown in Fig. 6.18. The different colloids exhibit different CDSI signals making it possible to clearly distinguish between them.

As before the expected CDSI signals were calculated using Eq. 6.10 for the multi-helix stack with the measured parameters for pitch, number of turns, and inner and outer radius. The

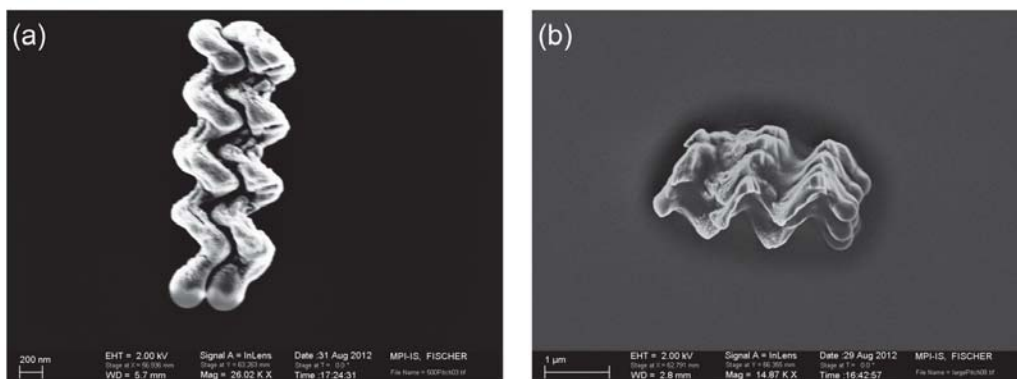


**Figure 6.17:** SEM images showing examples for conglomerates found in the solutions of (a) LH2 and (b) LH3. If the radius of the helices exceeds the mean distance between neighboring seeds, they may join during the growth process.

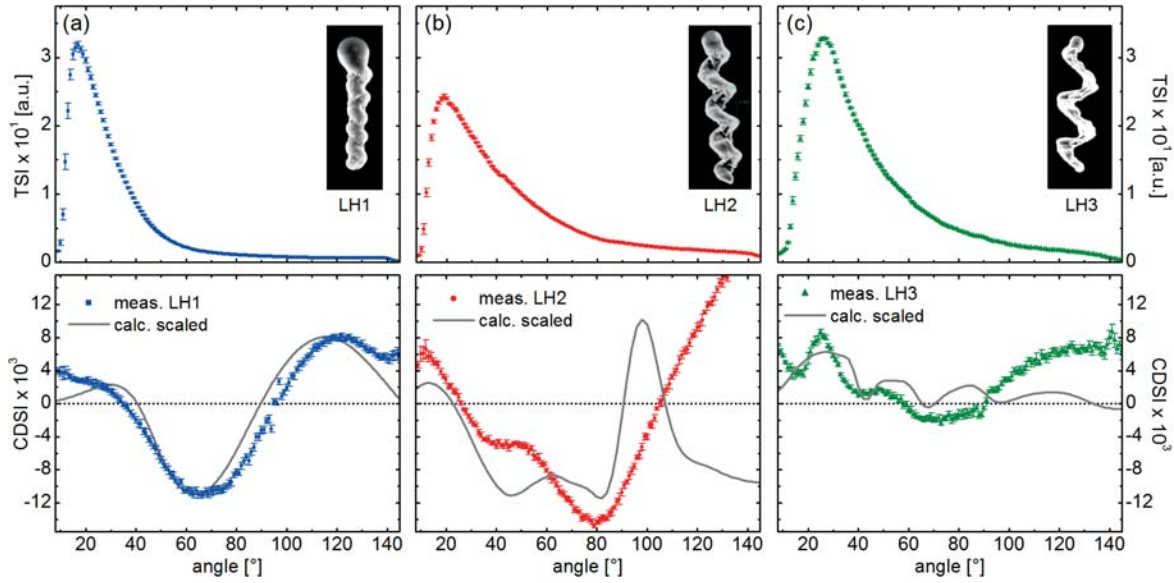


**Figure 6.18:** Total scattering intensity and the differential scattering signal of circular polarized light for left-handed helices with different geometrical parameters. The pitch  $P$  and also the radius  $a$  of the screws have been increased (from (a) to (c)). Also shown are the calculation results (solid lines).

number of thin helices and polarizabilities per turn were set to  $n_h = 5$  and  $n_p = 20$ , respectively. The results have been scaled and are also shown in Fig. 6.18. It is obvious that the agreement with the calculation is only guaranteed for sample LH1, the one with the smallest pitch. A possible explanation for the disagreement may be the influence of the aggregates on the CDSI signals, which have not been considered in the calculations. Exemplarily this influence has been estimated for LH2 through calculations of  $\langle \Delta I \rangle$  for aggregates of two, three and four multihelices as shown in Fig. 6.19a. Here the multihelices are joined together along the x-axis of the scatterer fixed coordinate system. For the calculations Eq. 6.9a is appended by the term

$$1.25 a_{out} \left[ \frac{i}{n_h n_p T} \right] \hat{\mathbf{e}}_x,$$

and the modified Eqs. 6.9 are used in Eq. 6.4. Here all symbols have the same meaning as before. Figure 6.19b shows the scaled results together with the measured CDSI signal of LH2. As can be seen, the more helices are joined together the stronger the negative band at  $\sim 80^\circ$  gets compared to the one at  $\sim 40^\circ$ , which is also observed in the measured signal. The monotonic increase in the measured CDSI signal for  $\theta > 80^\circ$ , however, is not reflected by the calculations. This is likely due to the influence of other aggregates than the ones considered here.

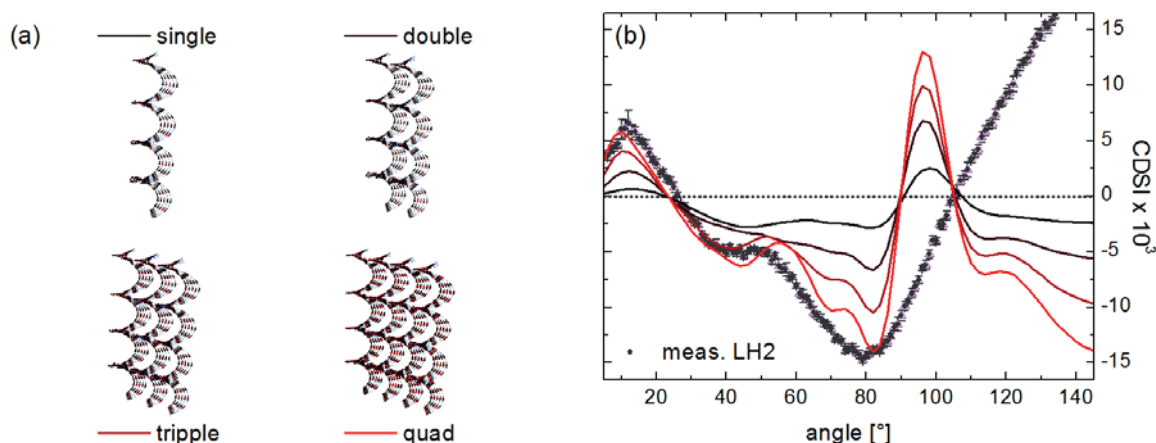


**Figure 6.19:** (a) Schemes of multihelix aggregates used for calculation. (b) Scaled results of  $\langle \Delta I \rangle$  for the aggregates shown in (a) together with the measured CDSI signal for LH2.

### 6.3 The propeller-effect and chiral separation

In 1978 Baranova and Zel'dovich predicted the "propeller effect" where a racemic mixture of chiral molecules is separated into its left and right-handed fractions when subjected to a radio-frequency electric field of rotating polarization [96]. The coupling between the applied electric field and the electric dipole moment of the molecules causes their rotation. Because the sense of the rotation is given by the circularity of the electric field, opposite enantiomers will "screw" in opposite directions. Therefore a separation along the rotation axis of the electric field takes place. Estimations by Baranova and Zel'dovich of the propeller effect for molecules with a permanent electric dipole moment of 4 Debye and a rotating electric field of 0.3 MV/m and 100 MHz deduced an enantiomeric excess of 7% per centimeter of sample vessel after  $\sim 27$  hours. Therefore the propeller effect has thus far not been demonstrated experimentally.

In the colloidal analogue the electric dipolar molecules are replaced by magnetic dipolar colloids driven by a rotating magnetic field. For this purpose a ferromagnetic 200 nm strip made of Ni was included into the helices. Before releasing the helices from the wafer they are magnetized orthogonally to their long axis by placing the wafer into a strong electromagnet ( $\sim 1.8$  T). In Fig. 6.20a it is schematically shown how a homogeneous, rotating magnetic field couples to the magnetic moment of the helices and causes their rotation. Due to shape-induced rotation-translation coupling the helices also translate. To minimize drag the helices will align since the drag on the side of the helix is larger. Finally they will be propelled along the rotation axis of the rotating magnetic field. For a helix the direction of translation is given by its chirality and is therefore opposite to its enantiomer. For a racemic mixture this results in a chiral separation, as has been successfully shown in [P6]. In summary it could be successfully demonstrated, that the differential scattering (CDSI) of

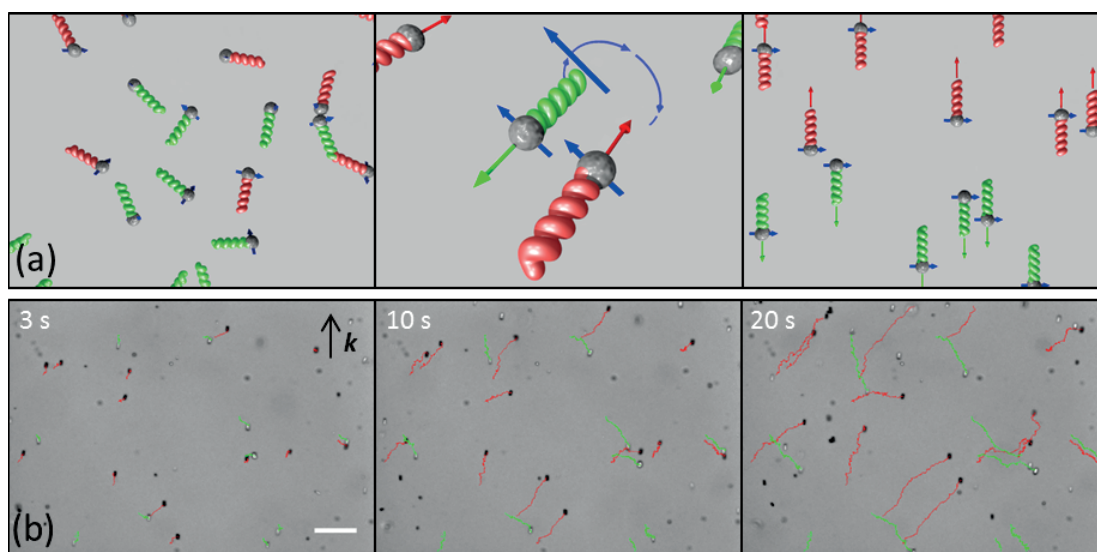


**Figure 6.20:** (a) Schematic of magnetic dipolar colloidal helices in the presence of a rotating magnetic field. The enantiomers (red and green) possess a magnetic dipole moment (blue arrow) which will align and rotate with the applied field. Therefore the helices propel in opposite directions. (b) Tracks of right- (red) and left-handed (green) colloids in a magnetic field of 20 Gauss rotating with 20 Hz (time interval 20 s, scale bar 20  $\mu\text{m}$ ) (taken from [P6]).

circularly polarized light is a useful diagnostic tool for the characterization of chiral colloids in solution. Beside a small correction of the theory proposed by Bustamante et al. [21] an extension to helices of finite thickness was developed. By measurements of different  $\mu\text{m}$ -sized  $\text{TiO}_2$  helices in solution, the CDSI signal was shown to be sensitive to the sense and shape of the chiral parts of the colloids (i.e. pitch and radius).



# 7

## Conclusion

Optical methods provide a direct mechanism of distinguishing between the enantiomers of chiral molecules. Although there exist a number of established techniques and commercial instruments optical activity remains difficult to detect in small sample volumes or strongly absorbing environments. Thus new chiroptical methods have been successfully developed, evaluated and presented in this thesis. These methods are based on the difference of the interaction of chiral molecules and colloids with left- and right-circularly polarized light in refraction, absorption or scattering. These phenomena are now discussed in turn.

### 7.1 Chiral refractometry

In the chiral refractometer optical activity is detected in refraction. The difference  $\delta n$  in the real part of the refractive index causes both circular polarizations to refract with slightly different angles at an interface between a chiral and an achiral medium. The difference in the refraction angles for the polarization components is usually on the order of several nanorads ( $10^{-9}$  rad). Furthermore knowing in which direction the right- or the left-circular components refract contains the information on the handedness of the optically active medium (e.g. the molecules' chirality). Therefore different detection schemes for the optical activity induced beam deflection or splitting have been tested. They can be separated into (I) position methods and (II) intensity methods.

The position method (I) incorporates the direct detection using a position sensitive diode (PSD) combined with an appropriate polarization modulation. Here a dual-polarization modulation scheme was implemented with two photoelastic modulators (PEM). The polarization of the incoming light beam is altered between circular states at the difference

frequency of the two PEMs. This reduced artifacts arising from interference and beam deflections induced by the PEM. Therefore changes in the circular birefringence  $\delta n$  of  $1 \times 10^{-8}$  could be resolved.

The intensity method (II) demonstrates a new form of optical activity measurement based on a modified weak value amplification scheme. Weak value amplification has been shown to be a promising tool to detect small, achiral and polarization-dependent beam deflections, where the spatial beam separation is several orders of magnitude than the beam diameter itself. To determine the sign of the polarization-dependent beam splitting two modifications were introduced: a heterodyne mixing scheme using a Zeeman-HeNe laser and a polarization modulation scheme. This allows for an amplification of up to  $\sim 10^6$  in the separation of the beam components compared with the actual separation (in the absence of weak value amplification). Both modulation schemes have been chosen so that they measure angular deflections and not optical rotation. It was further demonstrated that they can be used to determine the absolute sign of the optical activity. With the heterodyne detection setup a circular birefringence of  $\delta n = 1 \times 10^{-8}$  has been resolved. The most sensitive method developed is the polarization modulated weak value amplification scheme since it could detect circular birefringence of  $\Delta n \sim 1 \times 10^{-9}$  with a relative error of  $s_{rel} \leq 1\%$ .

This sensitivity corresponds to an optical rotation  $\alpha = \pi \delta n l / \lambda$  of about  $0.03^\circ$  in a polarimeter that uses a 10 cm sample cell. However, unlike the polarimeter, which requires volumes of at least  $800 \mu\text{l}$ , the refraction method requires a volume of less than  $8 \mu\text{l}$  (assuming a laser beam with a cross section of  $< 2 \text{ mm}$  and a wedge shaped sample cell with  $2 \times 4 \times 2 \text{ mm}^3$ ). Using a cell of the same length (2 mm) in a polarimeter the 50-fold shorter pathlength would result in a reduced optical rotation of  $0.0006^\circ$ , which is comparable to the sensitivity of typical commercial polarimeters ( $\sim 0.001^\circ$ ). The schemes shown in this thesis can be even more sensitive when using enhancement methods of the angular splitting as proposed by Ghosh et al. [29, 30]. An interesting prospect is also to extend the refraction scheme by combining it with interferometric weak-value detection (which we used for the photothermal spectroscopy of a silane monolayer [P5]). A resolution of  $\sim 1$  picorad in angular separation has been reported in [35]. Such sensitivity promises the analysis of solutions that rotate the polarization by  $0.00003^\circ$  in  $\sim \mu\text{l}$  volumes, and would surpass the sensitivity of any commercial laboratory polarimeter.

## 7.2 MIR laser-based vibrational optical activity

Work in this thesis reports the first vibrational optical activity (VOA) spectra recorded with a tunable quantum cascade laser (QCL). Both, circular dichroism (VCD) and circular birefringence (VCB) spectra, which are Kramers-Kronig transforms of each other, were measured in the mid-infrared region. Despite their limited spectral range, quantum cascade lasers offer a number of distinct advantages. They can be tuned with high resolution, which

permits close-lying bands to be resolved and facilitates comparison with calculations. They also provide a significantly higher output power compared to conventional thermal light sources (up to  $10^4$ ), which permits measurements in longer-path-length cells. This is promising for both chiroptical spectroscopies (VCB and VCD) since they scale linearly with path length. Moreover allows the spectral brightness of a QCL measurements in strongly absorbing solvents, i.e. aqueous solutions.

These advantages have been demonstrated with a QCL-based setup comprising a ZnSe-modulator (PEM) and a thermo-electrically (TE) cooled detector. VOA spectra of different samples have been recorded and compared to FT spectrometer measurements and calculations. They were found to be in good agreement with each other. Among the samples were solutions of the inorganic complex  $\text{Ni}(\text{sp})\text{Cl}_2$  and the aromatic terpenoid limonene. Furthermore spectra of an aqueous solution of the amino acid proline were presented. Measured in a  $100\ \mu\text{m}$  cell they had an optical density of up to 3.5 in the examined spectral region. Nevertheless satisfactory VCD data have been recorded for both enantiomers.

The limiting factor for the sensitivity of the QCL setup is the reproducibility of the solvent background. It is mainly dominated by instrumental birefringence and interference effects inside the PEM. Therefore a modified setup was implemented using a detector with  $\text{LN}_2$  cooling (providing an enhanced detectivity) and an anti-reflection coated PEM. Background artifacts due to interference effects could be reduced, and a decreased mean RMS deviation between subsequent measurements of  $2 \times 10^{-5}$  is demonstrated compared to  $3 \times 10^{-4}$  for the first setup. Finally, VCD spectra of an aqueous solution of L-proline were recorded using the modified setup, which showed an enhanced SNR (40 compared to 28). The reproducibility and therefore the sensitivity of the present setup may be further enhanced through the implementation of an optical reference channel. This could eliminate artifacts arising from wavelength tuning errors of the QCL, which are suspected to be the reason for the “spikes” observed in the RMS deviation data. A dual PEM method as proposed by Nafie et. al [51] could be a promising tool to further suppress artifacts due to linear birefringence. Nevertheless, the results of this thesis pave the way for laser-based vibrational optical activity measurements. They also demonstrate the viability of QCLs for VOA spectroscopy of biomolecules in spectral regions that are difficult to study due to significant absorption by water, such as the amide III region ( $1400 - 1100\ \text{cm}^{-1}$ ). Moreover, QCL-based VCD-setups are promising for time-resolved studies of optical activity in aqueous solutions, which is also supported by the moderate measurement time of  $\sim 20$  min compared to aqueous studies with FTIR-VCD instrumentations. Time-resolved VCD measurements can be used to optimize reaction conditions leading to a maximum ee (enantiomeric excess) which may not be the same yielding maximum product. First successful tests of the use of laser-based VCD spectroscopy for reaction monitoring were performed in collaboration with the group of Dr. S. Lüdeke (University Freiburg). The results are going to be published in [P7] and [P9].

### 7.3 Mid-infrared refractometry

Due to their compact and rugged design quantum cascade lasers are an attractive practical laser light source in the MIR spectral range. They are also technically less demanding than nonlinear optical frequency conversion schemes based on short pulse high power lasers. One drawback, however, are the intensity fluctuations QCLs are often plagued with. These limit the achievable sensitivity in transmission based absorption measurements especially when detecting weakly absorbing species. Therefore vibrational spectroscopy in the MIR was demonstrated with a quantum cascade laser without the need to directly measure absolute intensities. A MIR refractometer has been introduced which relies on detecting changes in the real part of the index of refraction (angles of reflection) to deduce the absorption via a beam profile analysis. First measurements with an achiral sample have been successful. Pure dichloromethane (DCM), which showed a single absorption line in the wavelength region of the laser, has been used as a test sample. Both the dispersion and absorption line shapes were deduced simultaneously from the analysis of beam profile changes at a total internal reflection interface. In the present setup it requires an expensive imaging setup limited through any distortion of the beam profile. The sensitivity and ease of implementation would therefore benefit from position sensitive detectors in the MIR, which are not yet commercially available. This would allow for the implementation of position detection schemes as presented for the chiral refractometer to measure vibrational circular birefringence (VCB) via measurements of the optical activity induced beam deflection and splitting. The corresponding VCD spectrum could then be revealed by a Kramers-Kronig transform permitting an alternative CD detection mode without the need for direct intensity measurements.

### 7.4 Chiral scattering and colloidal molecules

Generally, the physical effects due to the symmetry breaking of chiral molecules (optical activity) are often weak and difficult to experimentally detect. Therefore a number of physical chiral separation schemes have been proposed but have thus far not been demonstrated experimentally at the molecular scale. Complex nonspherical colloidal particles could act as “colloidal molecules” in mesoscopic model systems and thereby permit the visualization of molecular phenomena that are otherwise difficult to observe.

Using glancing angle physical vapor deposition (GLAD) a large number of helical colloids were produced in good yields. This technique allows the composition of chiral colloids with programmable shape and chirality. In this thesis the circular differential scattering (CDS) has been shown to be useful for the characterization of these chiral colloidal suspensions. CDS spectra for suspensions of left- and right-handed helical colloids have been obtained.

Cylindrical shaped colloids and  $\text{SiO}_2$  beads were used as an achiral probe, showing no CDS signals, as expected. The scattering data of the colloids agreed well with theoretical predictions. The calculations are based on a model presented by Bustamante et al. [21], which has been adapted to the case of an helical scatterer with a finite thickness. Further calculations are presented to show the sensitivity of the scattering signals to the chiral parameters of the helices, like pitch and radius for example. The model has been tested with measurements on colloids with increasing pitch and it could be clearly distinguished between the signals of the different samples. However, here the formation of aggregates in solution complicates the analysis and no satisfactory agreement with theoretical predictions could be found. Finally, the observation of the propeller effect was reported using the chiral colloidal molecules. In summary it could be successfully demonstrated that chiral scattering is a sensitive probe of the configuration and structure of chiral colloids.





## References

- [1] W. T. LORD KELVIN , “The molecular tactics of a crystal”. Clarendon Press, Oxford (1894)
- [2] T. ITO, H. ANDO, T. SUZUKI, T. OGURA, K. HOTTA, Y. IMAMURA, Y. YAMAGUCHI, AND H. HANDA, “Identification of a primary target of thalidomide teratogenicity.”, *Science* **327**, pp. 1345 – 1350 (2010)
- [3] L. D. BARRON , “Molecular Light Scattering and Optical Activity”. Cambridge University Press, 2nd edition (2004)
- [4] G. FASMAN , “Circular Dichroism and the Conformational Analysis of Biomolecules”. Springer, 1rst edition (1996)
- [5] N. BEROVA, K. NAKANISHI, AND R. W. WOODY , “Circular Dichroism: Principles and Applications”. Wiley, 2nd edition (2000)
- [6] L. D. BARRON, F. ZHU, L. HECHT, G. E. TRANTER, AND N. W. ISAACS, “Raman optical activity: An incisive probe of molecular chirality and biomolecular structure”, *J. Mol. Struct.* **834**, pp. 7 – 16 (2007)
- [7] P. FISCHER AND F. HACHE, “Nonlinear optical spectroscopy of chiral molecules.”, *Chirality* **17**, pp. 421 – 437 (2005)
- [8] P. FISCHER , “Nonlinear Optical Spectroscopy of Chiral Molecules”. In N. Berova, P. L. Polavarapu, K. Nakanishi, and R. W. Woody, editors, *Comprehensive Chiroptical Spectroscopy: Instrumentation, Methodologies, and Theoretical Simulations (Volume 1)*, chapter 13, pages 347 – 371. John Wiley & Sons, 1st edition (2012)
- [9] A. D. BUCKINGHAM AND P. FISCHER, “Direct chiral discrimination in NMR spectroscopy”, *Chem. Phys.* **324**, pp. 111 – 116 (2006)
- [10] J. LABUTA, S. ISHIHARA, T. ŠIKORSKÝ, Z. FUTERA, A. SHUNDO, L. HANYKOVÁ, J. V. BURDA, K. ARIGA, AND J. P. HILL, “NMR spectroscopic detection of chirality and enantiopurity in referenced systems without formation of diastereomers.”, *Nat. Commun.* **4**, pp. 2188–1 – 2188–8 (2013)
- [11] J. M. BIJVOET, A. F. PEERDEMAN, AND A. J. VAN BOMMEL, “Determination of the absolute configuration of optically active compounds by means of X-rays”, *Nature* **168**, pp. 271 – 272 (1951)

- [12] L. A. NAFIE , “Vibrational Optical Activity: Principles and Applications”. John Wiley & Sons, 1st edition (2011)
- [13] K. GOTTFRIED AND T.-M. YAN , “Quantum Mechanics: Fundamentals”. Springer, 2nd edition (2003)
- [14] B. E. A. SALEH AND M. C. TEICH , “Fundamentals of Photonics”. John Wiley & Sons, 2nd edition (2007)
- [15] M. BASS , “Handbook of Optics, Volume I: Geometrical and Physical Optics, Polarized Light, Components and Instruments”. McGraw-Hill Professional, 2nd edition (1996)
- [16] G. H. WAGNIÈRE , “On the interaction of light with molecules: pathways to the theoretical interpretation of chiroptical phenomena”. In N. Berova, P. L. Polavarapu, K. Nakanishi, and R. W. Woody, editors, *Comprehensive Chiroptical Spectroscopy: Instrumentation, Methodologies, and Theoretical Simulations (Volume 1)*, chapter 1, pages 3 –34. John Wiley & Sons, 1st edition (2012)
- [17] H. RHEE AND M. CHO , “Femtosecond infrared circular dichroism and optical rotatory dispersion”. In N. Berova, P. L. Polavarapu, K. Nakanishi, and R. W. Woody, editors, *Comprehensive Chiroptical Spectroscopy: Instrumentation, Methodologies, and Theoretical Simulations (Volume 1)*, chapter 8, pages 203 – 219. John Wiley & Sons, 1st edition (2012)
- [18] L. D. BARRON AND A. D. BUCKINGHAM, “Rayleigh and Raman optical activity”, *Annu. Rev. Phys. Chem.* **26**, pp. 381 – 396 (1975)
- [19] A. D. BUCKINGHAM AND M. B. DUNN, “Optical activity of oriented molecules”, *J. Chem. Soc. A*, pp. 1988 – 1991 (1971)
- [20] L. D. BARRON AND A. D. BUCKINGHAM, “Rayleigh and Raman scattering from optically active molecules”, *Mol. Phys.* **20**, pp. 1111 – 1119 (1971)
- [21] C. BUSTAMANTE, “Circular intensity differential scattering of light. IV. Randomly oriented species”, *J. Chem. Phys.* **76**, pp. 3440 – 3446 (1982)
- [22] A. J. FRESNEL , “Œuvres complètes d’Augustin Fresnel: Théorie de la lumière” (1866)
- [23] A. GHOSH AND P. FISCHER, “Chiral Molecules Split Light: Reflection and Refraction in a Chiral Liquid”, *Phys. Rev. Lett.* **97**, pp. 173002–1 – 4 (2006)
- [24] M. P. SILVERMAN, “Reflection and refraction at the surface of a chiral medium: comparison of gyrotropic constitutive relations invariant or noninvariant under a duality transformation”, *J. Opt. Soc. Am. A* **3**, pp. 830 – 837 (1986)

- [25] M. P. SILVERMAN AND J. BADOZ, “Interferometric enhancement of chiral asymmetries: ellipsometry with an optically active Fabry-Perot interferometer”, *J. Opt. Soc. Am. A* **11**, pp. 1894 – 1916 (1994)
- [26] I. J. LALOV AND E. M. GEORGIEVA, “Multibeam interference, total internal reflection and optical activity”, *J. Mod. Optic.* **44**, pp. 265 – 278 (1997)
- [27] A. GHOSH, F. M. FAZAL, AND P. FISCHER, “Circular differential double diffraction in chiral media.”, *Opt. Lett.* **32**, pp. 1836 – 1838 (2007)
- [28] A. GHOSH, W. HILL, AND P. FISCHER, “Observation of the Faraday effect via beam deflection in a longitudinal magnetic field”, *Phys. Rev. A* **76**, pp. 055402–1 – 4 (2007)
- [29] R. P. RAJAN AND A. GHOSH, “Enhancement of circular differential deflection of light in an optically active medium.”, *Opt. Lett.* **37**, pp. 1232 – 1234 (2012)
- [30] R. PAPUKUTTY RAJAN AND A. GHOSH, “Angular amplification by a diffraction grating for chiro-optical measurements.”, *Appl. Opt.* **51**, pp. 6480 – 6483 (2012)
- [31] Y. AHARONOV, D. Z. ALBERT, AND L. VAIDMAN, “How the result of a measurement of a component of the spin of a spin-1/2 particle can turn out to be 100”, *Phys. Rev. Lett.* **60**, pp. 1351 – 1354 (1988)
- [32] I. M. DUCK, P. M. STEVENSON, AND E. C. G. SUDARSHAN, “The sense in which a “weak measurement” of a spin-1/2 particle’s spin component yields a value 100”, *Phys. Rev. D* **40**, pp. 2112 – 2117 (1989)
- [33] N. W. M. RITCHIE, J. G. STORY, AND R. G. HULET, “Realization of a measurement of a “weak value””, *Phys. Rev. Lett.* **66**, pp. 1107 – 1110 (1991)
- [34] O. HOSTEN AND P. KWIAT, “Observation of the spin hall effect of light via weak measurements.”, *Science* **319**, pp. 787 – 790 (2008)
- [35] P. DIXON, D. STARLING, A. JORDAN, AND J. HOWELL, “Ultrasensitive Beam Deflection Measurement via Interferometric Weak Value Amplification”, *Phys. Rev. Lett.* **102**, pp. 173601–1 – 4 (2009)
- [36] J. C. HOWELL, D. J. STARLING, P. B. DIXON, P. K. VUDYASETU, AND A. N. JORDAN, “Interferometric weak value deflections: Quantum and classical treatments”, *Phys. Rev. A* **81**, pp. 033813–1 – 3 (2010)
- [37] A. J. LEGGETT, “Comment on “How the result of a measurement of a component of the spin of a spin-(1/2 particle can turn out to be 100””, *Phys. Rev. Lett.* **62**, pp. 2325 (1989)
- [38] M. SARGENT, W. E. LAMB, AND R. FORK, “Theory of a Zeeman Laser. I”, *Phys. Rev.* **164**, pp. 436 – 449 (1967)

- [39] T. B. FREEDMAN, X. CAO, R. K. DUKOR, AND L. A. NAFIE, “Absolute configuration determination of chiral molecules in the solution state using vibrational circular dichroism”, *Chirality* **15**, pp. 743 – 758 (2003)
- [40] L. A. NAFIE, “Vibrational circular dichroism: a new tool for the solution-state determination of the structure and absolute configuration of chiral natural product molecules.”, *Nat. Prod. Commun.* **3**, pp. 451 – 466. (2008)
- [41] P. J. STEPHENS, F. J. DEVLIN, AND J.-J. PAN, “The Determination of the Absolute Configurations of Chiral Molecules Using Vibrational Circular Dichroism (VCD) Spectroscopy”, *Chirality* **20**, pp. 643 – 663 (2008)
- [42] H. IZUMI, A. OGATA, L. A. NAFIE, AND R. K. DUKOR, “A revised conformational code for the exhaustive analysis of conformers with one-to-one correspondence between conformation and code: application to the VCD analysis of (S)-ibuprofen.”, *J. Org. Chem.* **74**, pp. 1231 – 1236 (2009)
- [43] F. WANG, C. ZHAO, AND P. L. POLAVARAPU, “A Study of the Conformations of Valinomycin in Solution Phase.”, *Biopolymers* **75**, pp. 85 – 93 (2004)
- [44] T. A. KEIDERLING, J. KUBELKA, AND J. HILARIO , “Vibrational Circular Dichroism of Biopolymers: Summary of Methods and Applications”. In M. Brainman and V. Gregoriou, editors, *Vibrational Spectroscopy of Biological And Polymeric Materials*, chapter 5, pages 253 – 324. CRC Press, Boca Raton (2006)
- [45] J. FAIST, F. CAPASSO, D. L. SIVCO, C. SIRTORI, A. L. HUTCHINSON, AND A. Y. CHO, “Quantum Cascade Laser”, *Science* **264**:pp. 553 – 556 (1994)
- [46] R. F. CURL, F. CAPASSO, C. GMACHL, A. A. KOSTEREV, B. MCMANUS, R. LEWICKI, M. PUSHARSKY, G. WYSOCKI, AND F. K. TITTEL, “Quantum cascade lasers in chemical physics”, *Chem. Phys. Lett.* **487**, pp. 1 – 18 (2010)
- [47] M. BRANDSTETTER AND B. LENDL, “Tunable mid-infrared lasers in physical chemosensors towards the detection of physiologically relevant parameters in biofluids”, *Sensor. Actuat. B* **170**, pp. 185 – 195 (2012)
- [48] H. RHEE, Y.-G. JUNE, J.-S. LEE, K.-K. LEE, J.-H. HA, Z. H. KIM, S.-J. JEON, AND M. CHO, “Femtosecond characterization of vibrational optical activity of chiral molecules.”, *Nature* **458**, pp. 310 – 313 (2009)
- [49] J. HELBING AND M. BONMARIN, “Vibrational circular dichroism signal enhancement using self-heterodyning with elliptically polarized laser pulses.”, *J. Chem. Phys.* **131**, pp. 174507–1 – 9 (2009)
- [50] R. A. LOMBARDI AND L. A. NAFIE, “Observation and calculation of vibrational circular birefringence: a new form of vibrational optical activity”, *Chirality* **21**, pp. E277 – E286 (2009)

- [51] L. A. NAFIE, “Dual Polarization Modulation: A Real-Time, Spectral-Multiplex Separation of Circular Dichroism from Linear Birefringence Spectral Intensities”, *Appl. Spectrosc.* **54**, pp. 1634 – 1645 (2000)
- [52] S. F. MASON AND R. D. PEACOCK, “Complexes of some first-row transition elements with (-)-spartein”, *J. Chem. Soc., Dalton Trans.* **2**:pp. 226 – 228 (1973)
- [53] Y. HE, X. CAO, L. NAFIE, AND T. FREEDMAN, “Ab initio VCD calculation of a transition-metal containing molecule and a new intensity enhancement mechanism for VCD.”, *J. Am. Chem. Soc.* **123**, pp. 11320 – 11321 (2001)
- [54] L. A. NAFIE AND T. B. FREEDMAN, “Vibronic coupling theory of infrared vibrational transitions”, *J. Chem. Phys.* **78**, pp. 7108 – 7116 (1983)
- [55] F. J. DEVLIN, P. J. STEPHENS, J. R. CHEESEMAN, AND M. J. FRISCH, “Ab Initio Prediction of Vibrational Absorption and Circular Dichroism Spectra of Chiral Natural Products Using Density Functional Theory:  $\alpha$ -Pinene”, *J. Phys. Chem. A* **101**, pp. 9912 – 9924 (1997)
- [56] D. M. MCCANN AND P. J. STEPHENS, “Determination of absolute configuration using density functional theory calculations of optical rotation and electronic circular dichroism: chiral alkenes.”, *J. Org. Chem.* **71**, pp. 6074 – 6098 (2006)
- [57] P. L. POLAVARAPU, “Renaissance in chiroptical spectroscopic methods for molecular structure determination.”, *Chem. Rec.* **7**, pp. 125 – 136 (2007)
- [58] V. BAUMRUK AND T. A. KEIDERLING, “Vibrational circular dichroism of proteins in water solution”, *J. Am. Chem. Soc.* **115**, pp. 6939 – 6942 (1993)
- [59] V. P. GUPTA AND T. A. KEIDERLING, “Vibrational CD of the amide II band in some model polypeptides and proteins”, *Biopolymers* **32**, pp. 239 – 248 (1992)
- [60] B. I. BAELO, P. PANCOSKA, AND T. A. KEIDERLING, “Vibrational circular dichroism spectra of proteins in the amide III region: measurement and correlation of bandshape to secondary structure.”, *Anal. Biochem.* **250**:pp. 212 – 221 (1997)
- [61] VENYAMINOV S. YU. AND F. G. PRENDERGAST, “Water (H<sub>2</sub>O and D<sub>2</sub>O) molar absorptivity in the 1000-4000 cm<sup>-1</sup> range and quantitative infrared spectroscopy of aqueous solutions.”, *Anal. Biochem.* **248**, pp. 234 – 245 (1997)
- [62] G. SCALMANI AND M. J. FRISCH, “Continuous surface charge polarizable continuum models of solvation. I. General formalism.”, *J. Chem. Phys.* **132**, pp. 114110 (2010)
- [63] J. KAPITÁN, V. BAUMRUK, V. KOPECKÝ, R. POHL, AND P. BOUR, “Proline zwitterion dynamics in solution, glass, and crystalline state.”, *J. Am. Chem. Soc.* **128**, pp. 13451 – 13462 (2006)

- [64] A. LAKHANI, P. MALON, AND T. A. KEIDERLING, "Comparison of vibrational circular dichroism instruments: development of a new dispersive VCD.", *Appl. Spectrosc.* **63**, pp. 775 – 785 (2009)
- [65] J. M. BRUNEL, "BINOL: A versatile chiral reagent.", *Chem. Rev.* **105**, pp. 857 – 897 (2005)
- [66] Y. CHEN, S. YEKTA, AND A. K. YUDIN, "Modified BINOL ligands in asymmetric catalysis.", *Chem. Rev.* **103**, pp. 3155 – 3212 (2003)
- [67] G. LANDEK, M. VINKOVIĆ, D. KONTREC, AND V. VINKOVIĆ, "Influence of Mobile Phase and Temperature on Separation of 1,1'-Binaphthyl-2,2'-Diol Enantiomers with Brush Type Chiral Stationary Phases Derived from l-Leucine", *Chromatographia* **64**, pp. 469 – 473 (2006)
- [68] Q.-S. HU, D. VITHARANA, AND L. PU, "An efficient and practical direct resolution of racemic 1,1'-bi-2-naphthol to both of its pure enantiomers", *Tetrahedron: Asymmetry* **6**, pp. 2123 – 2126 (1995)
- [69] C. GUO, R. D. SHAH, R. K. DUKOR, X. CAO, T. B. FREEDMAN, AND L. A. NAFIE, "Determination of enantiomeric excess in samples of chiral molecules using fourier transform vibrational circular dichroism spectroscopy: simulation of real-time reaction monitoring.", *Anal. Chem.* **76**, pp. 6956 – 6966 (2004)
- [70] C. CHEN, Y. FUJIMOTO, G. GIRDAUKAS, AND C. J. SIH, "Quantitative analyses of biochemical kinetic resolutions of enantiomers", *J. Am. Chem. Soc.* **104**, pp. 7294 – 7299 (1982)
- [71] J. E. BERTIE, R. N. JONES, AND C. D. KEEFE, "Infrared Intensities of Liquids XII : Accurate Optical Constants and Molar Absorption Coefficients Between 6225 and 500 cm<sup>-1</sup> of Benzene at 25Å° C , from Spectra Recorded in Several Laboratories", *Appl. Spectrosc.* **47**, pp. 891 – 911 (1993)
- [72] S. SINGH, "Refractive index measurement and its applications", *Phys. Scr.* **65**, pp. 167 – 180 (2002)
- [73] J. H. JAFFE, "The Measurement of Refractive Indexes of Liquids in the Infrared", *J. Opt. Soc. Am.* **41**, pp. 166 – 169 (1951)
- [74] J. H. JAFFE AND U. OPPENHEIM, "Infrared dispersion of liquids by critical angle refractometry.", *J. Opt. Soc. Am.* **47**, pp. 782 – 784 (1957)
- [75] R. J. KORNISKI AND W. L. WOLFE, "Infrared refractometer measurements of adhesives.", *Appl. Opt.* **17**, pp. 3138 – 3142 (1978)
- [76] R. E. KAGARISE AND J. MAYFIELD, "Simple Interferometer for Dispersion Measurements of Liquids in the 2-22 μ Region", *J. Opt. Soc. Am.* **48**, pp. 430 – 431 (1958)

- [77] P. N. SCHATZ, “Infrared Dispersion Measurements and Integrated Absorption Coefficients for Pure Liquid Benzene”, *J. Chem. Phys.* **32**, pp. 894 – 899 (1960)
- [78] J. HAWRANEK AND R. JONES, “The determination of the optical constants of benzene and chloroform in the IR by thin film transmission”, *Spectrochim. Acta A* **32**, pp. 111 – 123 (1976)
- [79] A. H. PFUND, “The Dispersion of CS<sub>2</sub> and CCL<sub>4</sub> in the Infrared”, *J. Opt. Soc. Am.* **25**, pp. 351 – 354 (1935)
- [80] J. FAHRENFORT AND W. M. VISSER, “On the determination of optical constants in the infrared by attenuated total reflection”, *Spectrochim. Acta A* **18**, pp. 1103 – 1108 (1962)
- [81] H. KOGELNIK AND T. LI, “Laser beams and resonators”, *Appl. Opt.* **5**, pp. 1550 – 1567 (1966)
- [82] A. VAN BLAADEREN, R. RUEL, AND P. WILTZIUS, “Template-directed colloidal crystallization”, *Nature* **385**, pp. 321 – 324 (1997)
- [83] P. SCHALL, I. COHEN, D. A. WEITZ, AND F. SPAEPEN, “Visualization of dislocation dynamics in colloidal crystals.”, *Science* **305**:pp. 1944 – 1948 (2004)
- [84] P. SCHALL, I. COHEN, D. A. WEITZ, AND F. SPAEPEN, “Visualizing dislocation nucleation by indenting colloidal crystals.”, *Nature* **440**, pp. 319 – 323 (2006)
- [85] M. E. LEUNISSEN, C. G. CHRISTOVA, A.-P. HYNINEN, C. P. ROYALL, A. I. CAMPBELL, A. IMHOF, M. DIJKSTRA, R. VAN ROIJ, AND A. VAN BLAADEREN, “Ionic colloidal crystals of oppositely charged particles.”, *Nature* **437**, pp. 235 – 240 (2005)
- [86] F. LI, D. P. JOSEPHSON, AND A. STEIN, “Colloidal Assembly: The Road from Particles to Colloidal Molecules and Crystals.”, *Angew. Chem.* **50**, pp. 360 – 388 (2011)
- [87] W. POON, “Colloids as Big Atoms.”, *Science* **304**, pp. 830 – 831 (2004)
- [88] A. VAN BLAADEREN, “Colloidal molecules and beyond.”, *Science* **301**, pp. 470 – 471 (2003)
- [89] E. DUGUET, A. DÉSSERT, A. PERRO, AND S. RAVAINÉ, “Design and elaboration of colloidal molecules: an overview.”, *Chem. Soc. Rev.* **40**, pp. 941 – 960 (2011)
- [90] S. SACANNA AND D. J. PINE, “Shape-anisotropic colloids: Building blocks for complex assemblies”, *Curr. Opin. Colloid Interface Sci.* **16**, pp. 96 – 105 (2011)
- [91] S. C. GLOTZER AND M. J. SOLOMON, “Anisotropy of building blocks and their assembly into complex structures.”, *Nat. Mater.* **6**, pp. 557 – 562 (2007)

- [92] S. SACANNA, L. ROSSI, AND D. J. PINE, “Magnetic click colloidal assembly”, *J. Am. Chem. Soc.* **134**, pp. 6112 – 6115 (2012)
- [93] R. M. ERB, H. S. SON, B. SAMANTA, V. M. ROTELLO, AND B. B. YELLEN, “Magnetic assembly of colloidal superstructures with multipole symmetry.”, *Nature* **457**, pp. 999 – 1002 (2009)
- [94] D. ZERROUKI, J. BAUDRY, D. PINE, P. CHAIKIN, AND J. BIBETTE, “Chiral colloidal clusters.”, *Nature* **455**, pp. 380 – 382 (2008)
- [95] M. ARISTOV, R. EICHHORN, AND C. BECHINGER, “Separation of chiral colloidal particles in a helical flow field”, *Soft Matter* **9**, pp. 2525 – 2530 (2013)
- [96] N. B. BARANOVA AND B. Y. ZEL’DOVICH, “Separation of mirror isomeric molecules by radio-frequency electric field of rotating polarization”, *Chem. Phys. Lett.* **57**, pp. 435 – 437 (1978)
- [97] K. ROBBIE, M. J. BRETT, AND A. LAKHTAKIA, “Chiral sculptured thin-films”, *Nature* **384**, pp. 616 (1996)
- [98] M. M. HAWKEYE AND M. J. BRETT, “Glancing angle deposition: Fabrication, properties, and applications of micro- and nanostructured thin films”, *J. Vac. Sci. Technol. A* **25**, pp. 1317 – 1335 (2007)
- [99] W. STÖBER, A. FINK, AND E. BOHN, “Controlled growth of monodisperse silica spheres in the micron size range”, *J. Colloid Interface Sci.* **26**, pp. 62 – 69 (1968)
- [100] S. RECLUSIA AND S. RAVAINÉ, “Synthesis of Colloidal Crystals of Controllable Thickness through the Langmuir-Blodgett Technique”, *Chem. Mater.* **15**, pp. 598 – 605 (2003)
- [101] M. MAESTRE, C. BUSTAMANTE, T. HAYES, J. SUBIRANA, AND I. TINOCO, “Differential scattering of circularly polarized light by helical sperm head from octopus *Eledone cirrhosa*”, *Nature* **298**, pp. 773 – 774 (1982)
- [102] C. BUSTAMANTE, I. TINOCO, AND M. F. MAESTRE, “Circular differential scattering can be an important part of the circular dichroism of macromolecules”, *P. Natl. Acad. Sci. USA* **80**, pp. 3568 – 3572 (1983)
- [103] C. BUSTAMANTE, M. F. MAESTRE, AND D. KELLER, “Expressions for the interpretation of circular intensity differential scattering of chiral aggregates.”, *Biopolymers* **24**, pp. 1595 – 1612 (1985)
- [104] A. S. BELMONT, S. ZIETZ, AND C. NICOLINI, “Differential scattering of circularly polarized light by chromatin modeled as a helical array of dielectric ellipsoids within the born approximation.”, *Biopolymers* **24**, pp. 1301 – 1321 (1985)

- [105] C. PHILLIPS, W. MICKOLS, M. MAESTRE, AND I. TINOCO, “Circular differential scattering and circular differential absorption of DNA-protein condensates and of dyes bound to DNA-protein condensates”, *Biochemistry* **25**, pp. 7803 – 7811 (1986)
- [106] S. ZIETZ, A. BELMONT, AND C. NICOLINI, “Differential scattering of circularly polarized light as a unique probe of polynucleosome superstructures. A simulation by multiple scattering of dipoles.”, *Cell Biophys.* **5**, pp. 163 – 187 (1983)
- [107] I. TINOCO AND A. L. WILLIAMS, “Differential absorption and differential scattering of circularly polarized light: Applications to biological macromolecules”, *Annu. Rev. Phys. Chem.* **35**, pp. 329 – 355 (1984)
- [108] J. A. HARPST, A. I. KRASNA, AND B. H. ZIMM, “Low-angle light-scattering instrument for DNA solutions.”, *Biopolymers* **6**, pp. 585 – 594 (1968)
- [109] F. SCHEFFOLD AND R. CERBINO, “New trends in light scattering”, *Curr. Opin. Colloid Interface Sci.* **12**, pp. 50 – 57 (2007)





## Own Publications

- [P1] M. PFEIFER AND P. FISCHER, “Weak value amplified optical activity measurements.”, *Opt. Express* **19**, pp. 16508 – 16517 (2011)
- [P2] M. PFEIFER AND P. FISCHER, “Heterodyne “weak measurements” of nanorad beam deflections”. In *Proceedings OPTO 2011*, pages 95 – 99 (2011)
- [P3] S. LÜDEKE, M. PFEIFER, AND P. FISCHER, “Quantum-Cascade Laser-Based Vibrational Circular Dichroism”, *J. Am. Chem. Soc.* **133**, pp. 5704 – 5707 (2011)
- [P4] M. PFEIFER, S. LÜDEKE, AND P. FISCHER, “Mid-IR laser-based vibrational optical activity”. In *Proceedings of SPIE*, volume 8219, page 821906 (2012)
- [P5] M. PFEIFER, A. RUF, AND P. FISCHER, “Indirect absorption spectroscopy using quantum cascade lasers: mid-infrared refractometry and photothermal spectroscopy”, *Opt. Express* **21**, pp. 25643 – 25654 (2013)
- [P6] D. SCHAMEL, M. PFEIFER, J. G. GIBBS, B. MIKSCH, A. G. MARK, AND P. FISCHER, “Chiral colloidal molecules and observation of the propeller effect.”, *J. Am. Chem. Soc.* **135**, pp. 12353 – 12359 (2013)
- [P7] A. RÜTHER, M. PFEIFER, V. A. LÓRENZ-FONFRÁ, AND S. LÜDEKE, “ph-Titration of proline monitored by quantum cascade laser-based vibrational circular dichroism”, *J. Phys. Chem. B*, *submitted* (2013)
- [P8] A. LAMBRECHT, M. PFEIFER, W. KONZ, J. HERBST, AND F. AXTMANN, “Broadband spectroscopy with external cavity quantum cascade lasers beyond conventional absorption measurements”, *Analyst, Advance Article* (2014)
- [P9] A. RÜTHER, M. PFEIFER, V. A. LÓRENZ-FONFRÁ, AND S. LÜDEKE, “Reaction monitoring using mid-infrared laser-based vibrational circular dichroism”, *Chirality*, *to be published* (2014)





# Danksagung

Eine wissenschaftliche Arbeit ist nie das Werk einer einzelnen Person. Nur durch die Hilfe und Unterstützung der zahlreichen Menschen, die mich während der letzten Jahre begleitet und bei der Erstellung dieser Arbeit unterstützt haben, konnte sie zu dem werden, was sie ist. Deshalb ist es jetzt an der Zeit, mich bei euch allen von Herzen zu bedanken.

Allen voran möchte ich meinem Doktorvater PROF. PEER FISCHER danken für die Vergabe der Arbeit und seine stets exzellente Betreuung trotz der räumlichen Distanz. Das mir entgegengebrachte Vertrauen und die Wertschätzung als auch die vielen konstruktiven Gespräche und Ideen haben für eine von Kreativität und Freude an der Wissenschaft geprägte Arbeitsatmosphäre gesorgt. Dies hat nicht zuletzt einen wesentlichen Teil zum erfolgreichen Gelingen dieser Arbeit beigetragen.

PROF. JORIS VON SLAGEREN danke ich für seine Bereitschaft, die vorliegende Arbeit zu begutachten, als auch PROF. SABINE LUDWIGS für die Übernahme des Prüfungsvorsitzes und damit der Vervollständigung der Prüfungskommission.

ARMIN LAMBRECHT, FRANK KÜHNEMANN und RAIMUND BRUNNER danke ich für die freundliche Aufnahme in ihre Abteilung bzw. Arbeitsgruppe am IPM und die Möglichkeit, dort zu promovieren.

STEFFEN LÜDEKE und ANJA RÜTHER danke ich für die herausragende Zusammenarbeit und fachliche Unterstützung gerade im Bereich der VCD-Spektroskopie. Dank gilt ebenso meinen WISSENSCHAFTLICHEN KOLLEGEN am Max-Planck Institut für Intelligente System, die mich offen und hilfsbereit für meine Arbeiten in Stuttgart aufgenommen haben, besonders DEBORA SCHAMEL, JOHN GIBBS, ANDREW MARK und natürlich JUTTA HESS.

Meinem ehemaligen Doktorandenkollegen und Mitstreiter CHRISTIAN PETERMANN für die zahlreichen anregenden und inspirierenden Diskussionen, gerade in Momenten voller experimenteller Frustration. Danke auch für die Versorgung mit exzellenten Heißgetränken.

Meinen Kollegen NIKLAS, STEPHAN und JENS für ihre konstruktiven Anregungen und Ideen, sowie die entspannten Zwischengespräche. Danke, dass ihr auch einem Ex-TOM-ler Mittagessenasyl gewährt



Den KOLLEGINNEN und KOLLEGEN am IPM gilt mein Dank für eine sehr angenehme Arbeitsatmosphäre, ihre stete Hilfsbereitschaft und die zerstreuen Pausengespräche. Besonders erwähnen möchte ich hier JOCHEN, PHILIPP, CONSTANZE, CHRISTIAN und CARLO, ebenso BIRGIT HUNDRIESER.

Besonders bedanken möchte ich mich bei MEINER FAMILIE. Durch euren Rückhalt und die liebevolle Fürsorge habt ihr in jeglicher Hinsicht die Grundsteine für meinen Weg gelegt und mir somit das Physikstudium ermöglicht.

Eine herausragende Stellung in jeglicher Hinsicht nimmt meine FREUNDIN SUSANNE ein, die mir in allen Phasen dieser Arbeit zur Seite stand. Du hast mir stets Mut zugesprochen und mich auch in der stressigen und nervenaufreibenden Endphase ertragen. Du gibst mir Halt, bringst mich zum lachen. Mit dir verbringe ich meine schönsten Momente. Danke für deine immerwährende und bedingungslose Unterstützung. Schön, dass du bei mir bist.



